

NAVAL POSTGRADUATE SCHOOL MONTEREY, CALIFORNIA



DISSERTATION

ANALYSIS OF MODAL TRAVEL TIME
VARIABILITY DUE TO MESOSCALE OCEAN
STRUCTURE

by

Amy R. Smith

June, 1997

Dissertation Supervisors:

Kevin B. Smith
Ching-Sang Chiu

Approved for public release; distribution is unlimited.

DTIC Quality ~~unclassified~~

19980102 095

REPORT DOCUMENTATION PAGE

Form Approved OMB No. 0704-0188

Public reporting burden for this collection of information is estimated to average 1 hour per response, including the time for reviewing instruction, searching existing data sources, gathering and maintaining the data needed, and completing and reviewing the collection of information. Send comments regarding this burden estimate or any other aspect of this collection of information, including suggestions for reducing this burden, to Washington Headquarters Services, Directorate for Information Operations and Reports, 1215 Jefferson Davis Highway, Suite 1204, Arlington, VA 22202-4302, and to the Office of Management and Budget, Paperwork Reduction Project (0704-0188) Washington DC 20503.

1. AGENCY USE ONLY <i>(Leave blank)</i>	2. REPORT DATE	3. REPORT TYPE AND DATES COVERED
	June, 1997	Doctoral Dissertation
4. TITLE AND SUBTITLE Analysis of Modal Travel Time Variability Due to Mesoscale Ocean Structure		5. FUNDING NUMBERS
6. AUTHOR(S) Amy R. Smith		
7. PERFORMING ORGANIZATION NAME(S) AND ADDRESS(ES) Naval Postgraduate School Monterey CA 93943-5000		8. PERFORMING ORGANIZATION REPORT NUMBER
9. SPONSORING/MONITORING AGENCY NAME(S) AND ADDRESS(ES)		10. SPONSORING/MONITORING AGENCY REPORT NUMBER
11. SUPPLEMENTARY NOTES The views expressed in this thesis are those of the author and do not reflect the official policy or position of the Department of Defense or the U.S. Government.		
12a. DISTRIBUTION/AVAILABILITY STATEMENT Approved for public release; distribution is unlimited.		12b. DISTRIBUTION CODE
13. ABSTRACT <i>(maximum 200 words)</i>		

This dissertation examines the effects of ocean mesoscale variability on acoustic arrival time patterns for two separate ocean environments. First, for an open ocean environment away from strong boundary currents, the effects of randomly phased linear baroclinic Rossby waves on acoustic travel time are shown to produce a variable overall spreading in the arrival pattern, primarily producing a delay in the later, axial arrivals. Second, using the state-of-the-art Semtner-Chervin eddy resolving global ocean circulation model coupled with the University of Miami Parabolic Equation (UMPE) acoustic propagation model, the effects of a fluctuating frontal region created by the California Current on the temporal, spatial and seasonal variability in the individual modal arrivals of the first thirty modes over a one-model-year time span is assessed. The mesoscale bias variability is also examined by comparing the various peak arrival times for the range-averaged environment to that of the range-dependent environment. To support this work, approximate "wide angle PE mode functions" were newly developed which form a different basis set for modal expansion from that obtained using standard normal mode theory. These new mode functions provide the proper basis set for modal expansion of the field computed by wide angle PE models.

14. SUBJECT TERMS Underwater Acoustic Propagation, Modal Decomposition, Acoustic Tomography		15. NUMBER OF PAGES 119	
		16. PRICE CODE	
17. SECURITY CLASSIFICATION OF REPORT Unclassified	18. SECURITY CLASSIFICATION OF THIS PAGE Unclassified	19. SECURITY CLASSIFICATION OF ABSTRACT Unclassified	20. LIMITATION OF ABSTRACT UL

Approved for public release; distribution is unlimited.

ANALYSIS OF MODAL TRAVEL TIME VARIABILITY DUE TO MESOSCALE OCEAN STRUCTURE

Amy R. Smith
Lieutenant Commander, United States Navy
B.A., St. Olaf College, 1980
M. S., University of Southern California, 1986
M. S., Massachusetts Institute of Technology, 1990
O. E., Massachusetts Institute of Technology, 1990

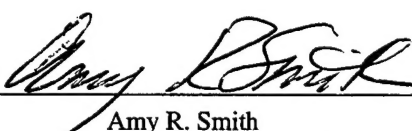
Submitted in partial fulfillment of the
requirements for the degrees of

DOCTOR OF PHILOSOPHY IN ENGINEERING ACOUSTICS

from the

NAVAL POSTGRADUATE SCHOOL
June, 1997

Author:



Amy R. Smith

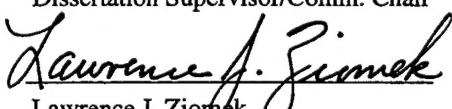
Approved by:



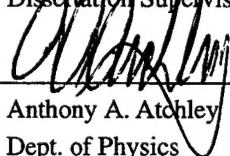
Kevin B. Smith
Asst. Prof. of Physics
Dissertation Supervisor/Comm. Chair



Ching-Sang Chiu
Assoc. Prof. of Oceanography
Dissertation Supervisor



Lawrence J. Ziemek
Prof. of Elect. and Comp. Engineering



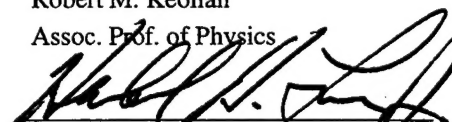
Anthony A. Atchley
Dept. of Physics



Robert M. Keolian

Assoc. Prof. of Physics

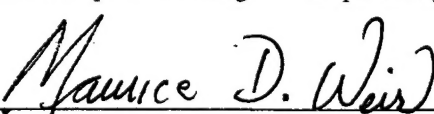
Approved by:



Herschel H. Loomis, Jr., Chairman
Dept. of Elect. and Comp. Engineering



Anthony A. Atchley, Chairman
Dept. of Physics



Maurice D. Weir, Associate Provost for Instruction

ABSTRACT

This dissertation examines the effects of ocean mesoscale variability on acoustic arrival time patterns for two separate ocean environments. First, for an open ocean environment away from strong boundary currents, the effects of randomly phased linear baroclinic Rossby waves on acoustic travel time are shown to produce a variable overall spreading in the arrival pattern, primarily producing a delay in the later, axial arrivals. Second, using the state-of-the-art Semtner-Chervin eddy resolving global ocean circulation model coupled with the University of Miami Parabolic Equation (UMPE) acoustic propagation model, the effects of a fluctuating frontal region created by the California Current on the temporal, spatial and seasonal variability in the individual modal arrivals of the first thirty modes over a one-model-year time span is assessed. The mesoscale bias variability is also examined by comparing the various peak arrival times for the range-averaged environment to that of the range-dependent environment. To support this work, approximate "wide angle PE mode functions" were newly developed which form a different basis set for modal expansion from that obtained using standard normal mode theory. These new mode functions provide the proper basis set for modal expansion of the field computed by wide angle PE models.

TABLE OF CONTENTS

I. INTRODUCTION	1
A. HISTORICAL BACKGROUND	3
B. ACOUSTIC MONITORING SYSTEMS	7
C. OCEAN-ACOUSTIC MODELING	8
D. DISSERTATION SUMMARY	9
II. THEORETICAL BACKGROUND	11
A. PARABOLIC EQUATION APPROXIMATION	11
1. Background	11
2. Theory	12
3. Implementation of the PE approximation	16
B. PE BROADBAND TRAVEL TIME COMPUTATION	18
C. MODAL ARRIVAL TIME COMPUTATION	19
III. MODE FUNCTIONS FOR THE WIDE ANGLE APPROXIMATION TO THE PARABOLIC EQUATION	25
A. THEORETICAL DEVELOPMENT	26
B. NUMERICAL IMPLEMENTATION	31
C. NUMERICAL RESULTS	34
D. SUMMARY	39
IV. TRAVEL TIME BIAS DUE TO OPEN OCEAN ROSSBY WAVES	43
A. THE MODELED OCEAN ENVIRONMENT	43
B. ACOUSTIC PROPAGATION MODELING	46

C. DATA ANALYSIS AND DISCUSSION.....	53
V. TRAVEL TIME VARIABILITY DUE TO THE CALIFORNIA CURRENT FRONT.....	67
A. OCEAN MODEL	69
B. ACOUSTIC PATH DESCRIPTION AND INPUT DATA PREPARATION.....	70
C. ACOUSTIC MODELING.....	76
D. MODAL ANALYSIS.....	81
E. SUMMARY	92
VI. CONCLUSIONS	93
REFERENCES	97
INITIAL DISTRIBUTION LIST	103

LIST OF FIGURES

1. Modal coefficient amplitudes as a function of range for modes 1, 8, 15, 20 and 25 of a range-independent Munk canonical sound speed profile.	36
2. Same as Fig. 1 except for modes 30, 35, 40, 45, and 50.....	37
3. Same as Fig. 1 except for modes 55, 60, 70, 72, and 74.	38
4. Comparison of mode 70 as computed using standard normal mode theory and the second order approximation to the wide angle mode function.	40
5. Comparison of arrival times computed using standard normal modes (KRAKEN) and second order approximate WAPE modes.	41
6. Sound speed perturbation field realization for $V_0=0.125$ m/s.	48
7. Sound speed perturbation field realization for $V_0=0.25$ m/s.	49
8. Transmission loss arrival time structure at range 1000 km for $V_0=0.125$ m/s.....	52
9. Representative modal decomposition of computed single frequency (100 Hz) pressure fields.	54
10. Transmission loss arrival time structures at range 500 km and depth 1000 m.....	55
11. Transmission loss arrival time structures at range 1000 km and depth 1000 m....	56
12. Arrival envelope lengths at 500 km range.	58
13. Arrival envelope lengths at 1000 km range.	59
14. Arrival envelope spread at 500 km range.....	60
15. Arrival envelope spread at 1000 km range.	61
16. Travel time bias in first and last arrival peaks at 500 km range.....	62
17. Travel time bias in first and last arrival peaks at 1000 km range.....	63
18. West coast sound sources.	70

19. Annual range-averaged sound speed profiles as interpolated from POCM output for modeled environment.	73
20. Sound speed perturbation field for POCM model date 05 Jan 95.	74
21. Sound speed perturbation field for POCM model date 01 Jul 95.	75
22. Typical range-dependent arrival structures at 200, 400, and 474 km ranges.	78
23. Plot of typical arrival structure at receiver depth (model date 31Jul95).	79
24. Full pressure field arrival structure at receiver over one model year period.	79
25. Centroid and energy distribution of arrival structure at receiver over one year.	79
26. Modal coefficient amplitudes for a single frequency run.	80
27. Annual spatial variability of selected mode functions at 200 km range.	82
28. Annual spatial variability of selected mode functions at 400 km range.	83
29. Annual spatial variability of selected mode functions at receiver range.	84
30. Annual variability in centroid of select modal arrivals at the 400 km range.	86
31. Temporal variability in first 30 modes at the 400 km range.	87
32. Frequency spectra of modal arrival times at the 400 km range.	89
33. Bias in full-field peak arrival.	91

LIST OF TABLES

Table 1. Acoustic propagation model (UMPE) input run parameters used to compute WAPE solution for the modeled range-independent deep ocean environment.....	35
Table 2. Assigned baroclinic mode phase values with resulting local sound speed axis depths and axis sound speeds at the initial range step.....	47
Table 3. Acoustic propagation model (UMPE) input run parameters for deep ocean environment with mesoscale structure.....	50
Table 4. Arrival statistics for deep ocean with random mesoscale structure.....	65
Table 5. Naval Postgraduate School SS3 source characteristics.....	71
Table 6. Pt. Sur receiver characteristics.....	71
Table 7. Acoustic propagation model (UMPE) input run parameters for west coast environment.....	77
Table 8. Ensemble statistics for modal arrivals at the 400 km range.....	88

ACKNOWLEDGEMENTS

First, I would like to acknowledge the financial support provided through the FY96 Student Research Fellowship Program sponsored by the Research, Development, Test and Evaluation Division of the Naval Command, Control and Ocean Surveillance Center (NRaD), San Diego CA and the Research Initiation Program at the Naval Post-graduate School, Monterey CA.

Next, I owe a very large debt of gratitude to my two advisors, Dr. Kevin Smith and Dr. Ching-Sang Chiu, and the other members of my dissertation committee, Dr. Anthony Atchley, Dr. Robert "Bonzo" Keolian, and Dr. Larry Ziomek. They helped me survive all the "growing pains" which come along with the Ph.D. experience. They provided me with much encouragement and an occasional "kick in the pants" when they knew I could do better. They also certainly shared (and supplied) many laughs along the way.

A special thank you also goes out to Mr. Paul Baxley, Dr. Newell Booth, Dr. Bill Hodgkiss, and Dr. John Roese for your personal encouragement and involvement through the NRaD Fellowship, and for providing me with the opportunity to participate in SWELLEX-96 on board the Research Platform FLIP.

I am also particularly grateful to Professor Semtner and Robin Tokmakian for supplying the Semtner-Chervin oceanographic model data used for a major portion of this work. And I would certainly be remiss if I didn't say thanks to the guys in the Coastal Acoustics lab, including Chris Miller, Stefan Hudson, and Rob Bourke, for all of their computer technical support.

There are many special friends who helped me maintain my sense of humor and perspective throughout my time here at NPS. While space prohibits mentioning them all, my heartfelt thanks goes out in particular to Daphne Kapolka, Joe Osborne, Bill Stewart, Bob Klocek, and the choir members of St. Thomas Aquinas parish.

Finally, but far from least, I give my love and thanks to my husband Patrick, to my four energetic children Jessica, Walter, Sean, and Shannon, and to my extended family for the tremendous support and encouragement you all provided. This "deployment" is finally over!

I. INTRODUCTION

Knowledge of ocean acoustics and associated environmental parameters is essential to developing and strengthening the Navy's ocean environmental/acoustic nowcasting and forecasting capabilities. As naval systems, platforms and sensors become increasingly more sophisticated, knowledge of environmental factors and their impact on acoustic propagation will play an even more critical role in undersea warfare (USW) system performance. To understand, predict, and assess the performance of various USW acoustic systems, it becomes essential to understand the temporal and spatial variability of the sound speed structure, the impact of oceanographic features such as fronts and mesoscale eddies on acoustic propagation, and acoustic pulse arrival time variations due to mesoscale features, internal waves, bottom properties and ambient noise. This dissertation focuses specifically on the effects of ocean mesoscale variability on acoustic arrival time patterns.

Oceanic mesoscale phenomena are the analogues of weather systems. Mesoscale features extend on the order of 100-250 km and persist on the order of 50-150 days. More than ninety percent of the kinetic energy of the entire ocean may be characterized by mesoscale variability rather than by large scale currents (Spindel and Worcester, 1990). These mesoscale features can significantly influence acoustic propagation and thus impact tactical operations. The impact of mesoscale features on the acoustic field at the receiver can be significant, affecting the temporal sequence, amplitude and angular distribution of the acoustic energy.

The presence of mesoscale phenomena was clearly established by oceanographic studies such as the MODE expedition in 1973 (Mode Group, 1978). A method for monitoring this mesoscale variability in the ocean interior, ocean acoustic tomography, was introduced by Munk and Wunsch (1979). In this method, the sound-speed fluctuation field within a volume is measured by the travel times of variously oriented acoustic transmissions through the volume. The acoustic travel time is inversely proportional to average sound speed along the transmission path. Shallow mesoscale perturbations will

alter only the average sound speed for steep ray arrivals, whereas mesoscale perturbations which extend to sound speed axis depths will alter the average sound speed for both steep and axial rays. Thus, by measuring travel-time perturbations of acoustic signals along various paths, the underlying sound speed structure may be inferred by inversion. The first at-sea experiment of this technique was performed in 1981 (Ocean Tomography Group, 1982). Subsequent efforts to refine tomographic techniques led to a number of investigations into travel time perturbations. A review of these studies is provided as background in Section A to help put into context the contributions presented by this dissertation.

Understanding inherent ocean variability is also important when installing "permanent" acoustic transmission systems, such as those considered in support of the Acoustic Thermometry of the Ocean Climate (ATOC) (Munk and Forbes, 1989) or the North Pacific Acoustic Laboratory (NPAL) (Worcester and Spindel, 1997). ATOC seeks to measure global warming related trends based on average large spatial-scale changes in the ocean's temperature distribution. NPAL is a recently proposed semi-permanent acoustic laboratory consisting of several vertical and/or horizontal line arrays to be used for continuous ocean monitoring and a variety of other experiments. Further introductory discussion of issues related to ocean variability and these transmission systems in relation to this dissertation are presented in Section B.

Valid numerical predictions of acoustic travel time variability due to mesoscale processes rely critically on realistic environmental inputs. While ideally these inputs might come from in-situ measurements, in general the ability to obtain a sufficient number of measured synoptic environmental samples to support long range acoustic propagation predictions is extremely limited. An alternate approach relies on state-of-the-art ocean models to provide the environment input data, and is the approach taken in this dissertation. This is discussed further in Section C. Finally, a summary of the dissertation contents is presented in Section D.

A. HISTORICAL BACKGROUND

In developing the concept of ocean acoustic tomography within the framework of ray theory, Munk and Wunsch (1979) relied on several simplifying assumptions. Two of their fundamental assumptions were

- 1) travel time changes between widely separated sources and receivers are related linearly to the magnitude of the intervening mesoscale perturbations, and
- 2) ray trajectories will remain stationary upon passage through a mesoscale perturbation; only the travel times will vary.

Mercer and Booker (1983) examined these assumptions and suggested that linearization is invalid for dealing with the problem under realistic conditions, particularly when the acoustic range exceeds a few hundred kilometers. Their results, based on ray tracing through a simulated warm midocean eddy and a cold core Gulf Stream ring (both circular with 200 km diameters), suggested that the changes in travel time are nonlinear as a function of sound speed. This non-linearity was found to especially affect the late-arriving (axial) rays. They further concluded that the assumption of stationary ray paths was incorrect, resulting in a significant error compared with the 10-ms precision that was expected for tomographic arrays. Overall, their results suggested that the range-dependent effects so badly bias the inversions for range-averaged oceans that tomographic results might be meaningless.

Other investigators (Spiesberger and Worcester, 1983) developed comparisons of exact and approximate perturbations in travel time and ray geometry due to mesoscale perturbations. The three approximations to the exact travel time they considered were

- 1) range-dependent perturbation and the unperturbed path,
- 2) range-average of the sound-speed perturbation and the unperturbed path, and
- 3) range average of the sound-speed perturbation and its associated (perturbed) ray path.

From their study, they concluded that travel-time errors incurred by using either linearized or range-averaged travel-time perturbation calculations are small, but not negligible (at

most 30% of the exact total travel time). They further concluded that range-dependent raytrace calculations would be necessary to achieve accurate inversions.

By the mid-1980's, investigations began to focus on examining the nonlinear bias observed in travel time perturbations with a goal of developing systematic methods in tomographic techniques to correct for this effect. The nonlinear bias results from the differences in ray path geometry (which is a function of the sound speed field) between the actual and modeled sound speed fields. Spiesberger (1985a, 1985b) approached the problem using numerical prediction within the framework of ray theory, whereas Munk and Wunsch (1985, 1987) took an analytical approach, again based on ray theory. General results from Spiesberger's work suggested that for the non-linear term in a range-dependent environment

- 1) the non-linear contribution is approximately proportional to the horizontal range traveled by the ray,
- 2) it is roughly proportional to the square of the magnitude of the eddy anomaly,
- 3) its value is insensitive to the position of the (isolated) eddies,

and more generally that

- 4) flat, axial rays are less linear than steep rays,
- 5) the magnitude and sign of the bias depends on the climatological profile used to model the sound speed field,
- 6) linear iteration tomographic methods may not be sufficient in all cases to correct for the bias, and
- 7) the nonlinear bias is small compared with seasonal fluctuations of the travel time.

Munk and Wunsch also found that linear inversions of the range-averaged sound speed profile are subject to a significant error arising from a quadratic bias. However, in their approach, they found that this quadratic bias is such that the travel time through a structured ocean is generally (not always) less than through a smooth ocean with the same mean properties. This is referred to as a negative (warm) bias. They also concluded that

the bias is generally constant. Thus, what matters for a problem such as detecting global warming is not that a warm bias exists, but rather any secular changes in the warm bias.

Ocean acoustic tomography, when first demonstrated, was performed using sources centered at frequencies about 224 Hz and with source-receiver ranges about 300 km. These conditions were suitable for using a ray theory approach. However, over time, there was a growing interest towards refining tomographic techniques for use at longer ranges and lower frequencies. Accordingly, to meet the challenges of lower frequency and longer ranges, further deep-water tomographic techniques were formed based on a combination of ray and mode theory (Munk and Wunsch, 1983), adiabatic mode theory (Shang, 1989), a wave-theoretic approach (Athanassoulis and Skarsoulis, 1995), and non-adiabatic parabolic equation modeling (Shang and Wang, 1993; Shang, 1997). In general, findings with regard to the travel time perturbations are similar to those reported by investigators implementing ray theory, with the exception that Shang (1997) reported a predominant “cold” bias based on full-wave parabolic equation (PE) modeling vice the “warm” bias found using analytic ray theory (Munk and Wunsch, 1987). This cold bias is also noted in both ray-tracing and PE numerical predictions by Tappert and Tang (unpublished 1995), in PE numerical predictions by Smith (1992) and Shang and Wang (1996), and PE numerical predictions done in support of this dissertation previously presented by Smith *et. al.* (1996).

Long-range propagation has also been suggested to allow measurements of range-averaged sound-speed (and corresponding temperature) profiles, effectively filtering out the mesoscale variability in order to observe trends in the mean ocean temperature (Munk and Forbes, 1989). In contrast to acoustic tomography, where the mesoscale variability is the “signal” providing information about the range-dependent sound speed mapping, the mesoscale variability is noise in the global measurement problem. If constant, the mesoscale bias is not a significant issue as investigators are interested in long-term temporal changes in mean ocean temperature. However, if the mesoscale bias variability is sufficiently great, then it becomes difficult to separate out the effects of global climatic changes from the mesoscale bias.

In related research outside the context of tomography, Smith *et. al.* (1992a, 1992b) considered the effects of ocean mesoscale perturbations on long-range acoustic ray propagation. It was shown that acoustic rays, particularly those traveling near the axis (corresponding to the lowest order modes), exhibited chaotic behavior, i.e., extreme sensitivity to small-scale perturbations in the environment and/or initial conditions. This again suggested that the arrival pattern of the lowest order modes becomes highly complicated at long ranges. Thus, chaotic ray motion limits the ability to make deterministic predictions of long-range arrival time patterns using ray theory. A deep water tomography experiment known as SLICE89 (Howe *et al.*, 1991) measured the arrival structure of a pulse at a range of 1000 km. The analysis of the resulting data was consistent with the aforementioned complexity of the lowest order modes. Further analysis (Colosi *et. al.*, 1994) strongly indicated that internal waves were responsible for this complexity rather than mesoscale fluctuations. However, other preliminary work (Smith, 1992) with Rossby waves suggested that such mesoscale features could significantly perturb the near-axial arrivals in spite of the adiabatic nature of the mode propagation.

As this review of travel time perturbation studies suggests, there is general agreement that a non-linear bias does indeed exist between travel times observed in a structured range-dependent ocean as compared to a smooth range-independent ocean with similar mean properties. However, there appears to be divergent conclusions with regard to the general sign of the bias. In this dissertation, the emphasis is on not only predicting a statistical mean for the bias, but on investigating its variability based on parameters such as range, local mode number, and mesoscale perturbation strength. In the deep ocean environment, perturbations will be shown to produce a variable overall spreading in the arrival structure, primarily producing a delay (cold bias) in the axial arrivals. In the more complicated region of the California current, the analysis of the bias remains more ambiguous.

B. ACOUSTIC MONITORING SYSTEMS

Understanding inherent ocean variability is also important when installing "permanent" acoustic monitoring systems. As discussed by Chiu *et. al.* (1994), there are three fundamental acoustic issues which must be carefully addressed when considering the locations of permanent sound sources and receivers. These issues include acoustic reliability, acoustic stability, and geophysical noise. Acoustic reliability involves determining the regions/sites which can be ensonified on a year-round basis based on a specified source location. Acoustic stability is concerned with understanding which portion of the acoustic arrival pattern is relatively invariant over time; estimation of useful travel time series requires stable arrivals. Finally, geophysical noise, or the size of the travel time change due to mesoscale features, ocean fronts, or seasonal cycles will directly influence the amount of measurement time required before a statistically significant trend can be observed. Hence, information regarding the variability of travel time perturbations becomes critical to large-scale monitoring projects such as ATOC and NPAL.

In recent discussions regarding possible site locations for establishing NPAL, the SOSUS array site at Pt. Sur, California was suggested as a potential site. Currently, the Naval Postgraduate School (NPS) has several sound sources within a 600 km radius of the Pt. Sur array site which were specifically deployed to study the California Current system. Transmissions from these sources are monitored through a bottom hydrophone at the Pt. Sur site. Through the use of coupled ocean-acoustic computer modeling, this dissertation specifically investigates issues of acoustic stability and geophysical noise related to the acoustic path (474.6 km in length) between one of these sound sources and the Pt. Sur receiver. Insights from this variability study might then be potentially useful in array configuration design for NPAL, refining tomographic techniques for this region, or for assessing travel time variability of ATOC transmissions through this region.

C. OCEAN-ACOUSTIC MODELING

In studying the effects of mesoscale variability on underwater sound propagation characteristics, it would be desirable to obtain in-situ measurements at sea for the sound propagation and oceanographic variables. A complete description of environmental conditions for acoustic purposes would require simultaneously sampling oceanographic variables of temperature, salinity, and pressure, but this is costly, time-consuming, and provides just a snapshot on a single day. Alternatively, coupled ocean-acoustic computer modeling provides a cost effective means of studying acoustic propagation through oceanographic features such as fronts and eddies on a range of spatial and temporal scales. Ocean models can also be coupled with atmospheric models to predict future states of the ocean in the upper layers. This permits spatial and temporal variability to be examined. As with any type of computer model, the model physics must still be validated with physical measurements.

As a result of ever-improving numerical methods, faster computers, and growing global data sets, ocean numerical models are becoming increasingly reliable and realistic (Semtner, 1995). Thus, state-of-the-art global ocean circulation models can be used to investigate geophysical time-scale acoustic variability. A demonstration of this was provided by Chiu *et. al.* (1994) when they presented their results of a ray variability simulation of sound transmission from Heard Island to the west coast of the United States. A similar ray variability simulation was also provided by Staten *et. al.* (1996) for an acoustic path between Hawaii and Monterey, California. Other coupled ocean-acoustic propagation models have been demonstrated by Robinson *et. al.* (1994) and Newhall *et. al.* (1990), among others. In this dissertation, a global ocean circulation model is coupled with a full-wave parabolic equation (PE) acoustic propagation model to study the travel time variability in a region approximately 500 km off the California coast. The code written to specifically interface these specific ocean and acoustic models is a unique contribution of this dissertation.

As discussed by Chiu *et. al.* (1994), travel time fluctuations yield information about the mesoscale processes along the acoustic path. These fluctuations are then useful

“signals” for the calibration of eddy-resolving global ocean circulation models. The statistics of predicted travel time variability as determined from the coupled ocean-acoustic model output and provided in this dissertation may then be checked against measured travel time variability for consistency.

D. DISSERTATION SUMMARY

The objective of this work is to examine (via computer simulation) the variability of modal acoustic travel times due to mesoscale ocean structure and to analyze these effects in terms of range, local modes, perturbation strength and travel time variability. These results have potential applicability to tomographic and long range acoustic thermometry techniques.

Chapter II, **Theoretical Background**, reviews the theory relevant to the material presented in the subsequent chapters. Overviews are provided of the parabolic equation approximation used for acoustic propagation modeling, the PE broadband travel time computation method, and the modal travel time computation method Modal Spectrum of the PE Field (MOSPEF) (Shang and Wang, 1993).

Chapter III, **Mode Functions for the Wide Angle Approximation to the Parabolic Equation**, examines the effect of various parabolic equation approximations on the normal mode decomposition of the computed pressure field. Local normal mode decompositions were required to analyze modal travel time variability as presented in this dissertation. However, in the course of doing this analysis, computations for the modal amplitudes of a reference range-independent PE field using standard normal modes yielded fluctuating vice constant modal amplitudes for modes higher than about mode 30. This led to the development and investigation of approximate “wide angle PE mode functions”. These mode functions form a different basis set for modal expansion from that obtained using standard normal mode theory. Chapter III presents numerical implementation schemes for approximating these wide angle mode functions, and results comparing range-independent wide angle PE field modal decompositions performed using wide angle

vs. standard mode functions. While this work was originally pursued as a “side issue” to this dissertation, it is perhaps one of the more significant aspects of this research.

Chapter IV, Deep Ocean Environment, investigates the effects of randomly phased Rossby wave baroclinic modes on acoustic travel time and arrival structure in a deep ocean environment. Numerical predictions of the acoustic field are obtained from a broadband, range-dependent parabolic equation (PE) model using a modeled deep ocean environment composed of a superposition of randomly phased Rossby waves to provide realistic mesoscale sound speed perturbations. The variability in arrival structure and the bias resulting from approximating the range-dependent environment with a range-averaged environment is examined for ranges of 500 and 1000 kilometers.

Chapter V, Coupled Ocean-Acoustic Modeling through a region of the California Current, investigates the effects of a fluctuating frontal region created by the California Current on modal acoustic travel time variability. For this phase of research, the state-of-the-art global Parallel Ocean Circulation Model (POCM) (Semtner and Chervin, 1992), also known as the Semtner and Chervin model, was used to obtain realistic input environmental data spanning a one-year time period for a 474 km acoustic path. The temporal, spatial and seasonal variability in the individual modal arrivals of the first thirty modes is assessed. The mesoscale bias variability is also examined by comparing the full-field peak arrival times for the range-averaged environment to that of the range-dependent environment.

Chapter VI, Conclusions, presents a summation of conclusions and identifies areas requiring further research.

II. THEORETICAL BACKGROUND

In this chapter, basic background theory relevant to subsequent chapters of the dissertation is presented. Specifically, overviews are provided of the parabolic equation approximation used for acoustic propagation modeling, the PE broadband travel time computation method, and a modal travel time computation method Modal Spectrum of the PE Field (MOSPEF) (Shang and Wang, 1993).

A. PARABOLIC EQUATION APPROXIMATION

1. Background

In a 1974 lecture, Tappert (1977, paper based on lecture) introduced the parabolic approximation to the wave equation to the underwater acoustics community. This approximation is valid to much lower frequencies (>2 Hz) than the geometrical acoustic (small wavelength) approximation as it retains all the diffraction effects associated with the ocean sound channel (Tappert, 1977). In contrast to separation of variables methods, which are based on the approximation that the ocean is exactly horizontally stratified, the parabolic approximation retains full coupling between local waveguide modes, thereby making it valid for more realistic, non-stratified oceans. These are just a few of the reasons why use of the parabolic approximation for acoustic propagation predictions has become commonplace.

In Tappert's original paper, several approximations to the so-called "square root operator" of the parabolic approximation were introduced. One of these defines what is known as the standard parabolic equation (SPE). Over the last twenty years, there have been additional higher order approximations made to the square root operator of the parabolic equation. One such approximation leads to the wide-angle parabolic equation (WAPE) introduced by Thomson and Chapman (1983). This WAPE approximation is based on an operator splitting by Feit and Fleck (1978), and extends the SPE

approximation to accommodate wider angles of propagation. It is also generally less sensitive to the choice of a reference wavenumber, k_0 . Furthermore, error analysis indicated that the effects of phase errors are greatly reduced with this operator. Subsequently, the WAPE approximation is favored over the SPE for predicting acoustic propagation, and (unless otherwise specified) is the approximation used for all acoustic propagation computations made in this dissertation.

2. Theory

To develop the parabolic equation approximation, first consider a time-harmonic acoustic field in a cylindrical coordinate system which can be represented by

$$P(r, z, \varphi, t) = p(r, z, \varphi) e^{-i\omega t}. \quad (2.1)$$

Substituting this into the wave equation in cylindrical coordinates leads to the Helmholtz equation

$$\frac{1}{r} \frac{\partial}{\partial r} \left(r \frac{\partial p}{\partial r} \right) + \frac{1}{r^2} \frac{\partial^2 p}{\partial \varphi^2} + \frac{\partial^2 p}{\partial z^2} + k_0^2 n^2(r, z, \varphi) p = -4\pi P_0 \delta(\mathbf{r} - \mathbf{r}_s), \quad (2.2)$$

where $k_0 = \frac{\omega}{c_0}$ is the reference wavenumber, $n(r, z, \varphi) = \frac{c_0}{c(r, z, \varphi)}$ is the acoustic index of refraction, c_0 is the reference sound speed, and $c(r, z, \varphi)$ is the acoustic sound speed. Here, all of the features of the environment are represented within $c(r, z, \varphi)$. We shall neglect density variations in this derivation, but this could be incorporated without any loss of generality. For a point source at coordinates $(r = 0, z = z_s)$,

$$\delta(\mathbf{r} - \mathbf{r}_s) = \frac{1}{2\pi r} \delta(z - z_s) \delta(r). \quad (2.3)$$

The reference pressure level P_0 is defined as the pressure amplitude at a reference distance of $R_0 = 1 \text{ m}$.

Treating the ocean as a waveguide with a cylindrical coordinate system, acoustic energy primarily propagates outward from an acoustic source in the horizontal direction. Therefore, the pressure field can be represented by an outgoing Hankel function slowly modulated by an envelope function, that is,

$$p(r, z, \phi) = \psi(r, z, \phi) H_0^{(1)}(k_0 r). \quad (2.4)$$

In the far-field the Hankel function can be approximated by the first term of its asymptotic expansion (Gradshteyn and Ryzhik, 1994)

$$H_0^{(1)}(k_0 r) \approx \left(\frac{2}{i\pi k_0 r} \right)^{1/2} e^{ik_0 r}, \quad k_0 r \gg 1. \quad (2.5)$$

Using this expression, the relationship between the acoustic pressure $p(r, z, \phi)$ and the envelope function $\psi(r, z, \phi)$ can be expressed as

$$p(r, z, \phi) = P_0 \sqrt{\frac{R_0}{r}} \psi(r, z, \phi) e^{ik_0 r}. \quad (2.6)$$

This is the definition of the so-called “PE field function” ψ , scaled such that at $r = R_0$, $|\psi| = 1$ and $|p| = P_0$. Substituting this into the Helmholtz equation, assuming azimuthal symmetry and dropping the source term, it can be shown that the far-field outgoing wave in layered media satisfies (Tappert, 1977; Smith and Tappert, 1993)

$$\frac{\partial \psi}{\partial r} = ik_0 (Q_{op} - 1) \psi \quad (2.7)$$

where the operators

$$Q_{op} = (1 + \mu + \varepsilon)^{1/2}, \quad (2.8)$$

$$\mu = \frac{1}{k_0^2} \frac{\partial^2}{\partial z^2}, \quad (2.9)$$

$$\varepsilon = n^2 - 1. \quad (2.10)$$

For range-independent environments, it should be noted that Eq. (2.7) is exact and defines the solution of the field propagating outward from the source.

The second order differential equation is now reduced to a first order one, thereby allowing solutions to be approximated via a one-way (no backscatter) non-iterative marching algorithm

$$\psi(r + \Delta r, z) = \exp \{ ik_0 \Delta r (Q_{op} - 1) \} \psi(r, z). \quad (2.11)$$

However, use of the full-band, exact square-root operator is not numerically efficient. Subsequently, approximations to Q_{op} have been introduced to reduce the computational burden. Note also that as approximations to Q_{op} are used, the pressure field computed from an approximate ψ substituted into the exact relation Eq. (2.6) also becomes approximate. The resulting approximate pressure field is therefore not exactly equivalent to the acoustic pressure field satisfying the acoustic wave equation. The significance of this will become apparent as the SPE and WAPE mode functions are compared in Chapt. III.

The SPE operator due to Tappert (1977) is obtained using the binomial approximation

$$Q_{op} = (1 + \mu + \epsilon)^{1/2} \approx 1 + \frac{1}{2}\mu + \frac{1}{2}\epsilon \quad \text{for } |\mu| \ll 1, |\epsilon| \ll 1. \quad (2.12)$$

This approximation assumes that variation in the refractive index is small to some degree ($|\epsilon| \ll 1$), and is limited to small propagation angles ($|\mu| \ll 1$). The literature suggests accurate solutions are limited to a half-beamwidth of $10^\circ - 20^\circ$ (see e.g., Jensen *et. al.*, 1994, p.346, or Chin-Bing *et. al.*, 1993, p.62) for the propagation angle. Substituting Eq. (2.12) into Eq. (2.7) yields the well-known standard parabolic equation for underwater acoustics

$$\frac{\partial \psi}{\partial r} = \frac{i}{2k_0} \frac{\partial^2 \psi}{\partial z^2} + \frac{ik_0}{2} \left(n^2 - 1 \right) \psi. \quad (2.13)$$

This equation is valid in the far-field, and neglects azimuthal coupling and backscatter.

Adopting the notation

$$Q_{SPE} = \left(1 + \frac{1}{2}\mu + \frac{1}{2}\epsilon \right), \quad (2.14)$$

Eq. (2.13) becomes

$$\frac{\partial \psi}{\partial r} = ik_0 (Q_{SPE} - 1) \psi. \quad (2.15)$$

A higher order approximation to Q_{op} introduced by Thomson and Chapman (1983) is based on an operator splitting by Feit and Fleck (1978). Commonly referred to as the “wide-angle” approximation, it has the form

$$Q_{WAPE} = (1 + \mu)^{1/2} + \left[(1 + \epsilon)^{1/2} - 1 \right]. \quad (2.16)$$

This operator extended the SPE operator to accommodate wider angles of propagation and was also found to be less sensitive to the choice of k_0 . The literature suggests accurate solutions are limited to a half-beamwidth of $\sim 40^\circ$ (see e.g., Jensen *et. al.*, 1994, p.350) for the WAPE propagation angle. However, benchmark testing using the WAPE approximation demonstrated the capability to accurately propagate fields for select environments with half-beamwidths of greater than 70° (Chin-Bing *et. al.*, 1993). Error analysis indicated that for typical deep ocean conditions, the effects of phase errors were greatly reduced relative to the SPE operator. For these reasons, use of the WAPE is commonplace for predicting sound propagation, and is the approximation used in the Navy standard PE model (Holmes and Gainey, 1991).

These are but two widely-used approximations to the exact square-root operator Q_{op} defined by Eq. (2.8). Other approximations exist, and use of any of these approximations to the exact square-root operator will give rise to some phase error beyond some range. In the next section, we shall examine how the wide angle approximation to the square-root operator is implemented for numerical predictions in the University of Miami

Parabolic Equation Model (UMPE) (Smith and Tappert, 1993), the model used for this dissertation work.

3. Implementation of the PE approximation

There are three common methods of computing PE solutions: (1) the split-step Fourier (PE/SSF) method (Hardin and Tappert, 1973), (2) the implicit finite difference (IFD-PE) method (e.g., Lee and Botseas, 1982), and (3) the finite element (FEPE) method (e.g., Collins, 1988). UMPE uses the PE/SSF method and the general algorithm behind this method is described below. For a more formal development, the reader is referred to Smith and Tappert (1993).

To initiate the computation, a regular spatial grid ($\Delta r, \Delta z$) is established onto which the environmental parameters (n, ρ) are mapped. Next, the marching algorithm, Eq. (2.11), requires that the initial conditions for the PE field function $\psi(r_0, z)$ as well as boundary conditions at the sea surface ($z=0$) and at the maximum computational depth ($z=z_{\max}$) be specified. The free surface is typically treated as a pressure release boundary, thus requiring $\psi(r, z=0) = 0$. The bottom boundary condition at $z = z_{\max}$ must approximate the radiation condition $\psi_b(z) \rightarrow 0$ as $z \rightarrow \infty$. However, since the computational depth is finite, the field amplitude is forced to zero in an artificial absorption layer which extends well below the bottom depth of interest. Because the PE/SSF algorithm numerically solves the one-way wave equation, Eq. (2.7), over all depths, there is no need to incorporate a numerical scheme to satisfy the appropriate boundary conditions at the water/sediment interface. These boundary conditions are automatically satisfied within the PE/SSF algorithm by simply including the changes in the environment at the water/sediment interface within the definition of the acoustic index of refraction, $n(r, z)$.

Before considering implementation of the marching algorithm further, note that the square root operator Q_{op} , Eq. (2.8), is written in terms of two other operators. One operator, ε , Eq. (2.10), is simply a multiplication operator in z -space and therefore forms a

diagonal matrix on the computational depth grid. The other operator, μ , Eq. (2.9), is a function of the second derivative in z -space, and thus forms a tridiagonal banded matrix on the computational depth grid. Correspondingly, when implementing the marching algorithm, the eigenfunction value in the z -domain at a given depth grid point is coupled to values at other depth points. However, since there is a unique eigenfunction for each eigenvalue, the corresponding operator in vertical wavenumber space is diagonal. This makes it desirable to separate the application of each operator to the domain in which it forms a diagonal matrix. The PE/SSF algorithm specifically assumes that these component operators, which are in some representation diagonal, may be applied independently. Using the simple relation

$$Q_{op} = 1 - (T_{op} + U_{op}), \quad (2.17)$$

the marching algorithm, Eq. (2.11), may be rewritten as

$$\psi(r + \Delta r, z) = \exp\{-ik_0 \Delta r T_{op}\} \exp\{-ik_0 \Delta r U_{op}\} \psi(r, z) \quad (2.18)$$

where T_{op} and U_{op} come from separating terms derived from μ and ε , respectively, in the desired square root operator approximation. This then leads to the following “split-step” implementation.

Once the boundary conditions and initial conditions for $\psi(r_0, z)$ are specified, a transformation is made to the k_z -domain followed by a multiplication of the k_z -space operator $e^{-ik_0 \Delta r \hat{T}_{op}(k_z)}$. The result is then transformed back to the z -domain and is followed by a multiplication of the z -space operator $e^{-ik_0 \Delta r U_{op}(z, r)}$. The final result is the field function at $r + \Delta r$. Therefore, the approximate solution for Ψ is marched out in range according to the relation

$$\Psi(z, r + \Delta r) = e^{-ik_0 \Delta r U_{op}(z, r)} \times IDFT\{e^{-ik_0 \Delta r \hat{T}_{op}(k_z)} \times [DFT(\Psi(z, r))]\} \quad (2.19)$$

where for the wide angle PE approximation

$$\hat{T}_{op}(k_z) = 1 - \left[1 - \left(\frac{k_z}{k_0} \right)^2 \right]^{1/2}, \quad (2.20)$$

and

$$U_{op}(z, r) = -[n(z, r) - 1]. \quad (2.21)$$

UMPE utilizes a FFT algorithm to implement the DFT in Eq. (2.19).

B. PE BROADBAND TRAVEL TIME COMPUTATION

The calculation of the time domain arrival structure is straightforward using the PE code. For a broadband acoustic field, the time-harmonic acoustic field initially assumed in Eq. (2.1) represents a single (CW) component of the general field. Separate PE calculations are then made to compute acoustic fields for each desired frequency over the bandwidth of interest. Using discrete time, $t = n\Delta t$, and discrete frequencies, $f = l\Delta f$, a total of N frequencies in the bandwidth of interest where $\Delta f\Delta t = \frac{1}{N}$, assuming azimuthal symmetry and adopting the notation

$$P(r, z, n\Delta t) = p_l(r, z) e^{-i\left(\frac{2\pi}{N}\right)nl}, \quad (2.22)$$

the representation of the field in the time domain can then be represented as

$$\tilde{P}(r, z, n\Delta t) = IDFT[X(l\Delta f)p_l(r, z)] = \frac{1}{N} \sum_{l=0}^{N-1} X(l\Delta f)p_l(r, z) e^{-i\left(\frac{2\pi}{N}\right)nl} \quad (2.23)$$

where $X(l\Delta f)$ represents the complex source spectrum. For all work presented here, a Hanning window is used to represent the source amplitudes providing a simple representation of a time-domain pulse.

In UMPE, arrival time structures are computed at user-designated fixed ranges, i.e. at $r = R$, using the value of the frequency-dependent range-scaled PE field function

$\frac{1}{\sqrt{R}} \Psi_{l,R}$. This neglects the overall phase factor $\exp(ik_0 R) = \exp(i2\pi l \Delta f R / c_0)$.

Consequently, the time domain is heterodyned around the value $t_0 = R/c_0$. Accordingly, arrival times are given in terms of “reduced time” or $t - t_0$. To reduce the computational burden, the UMPE model also heterodynes the signal by shifting the center frequency f_c to d.c. Adopting the notation $f_l = l \Delta f$, $f_c = l_c \Delta f$, $f_u = l_u \Delta f$ and $t_0 = n_0 \Delta t$, where f_l , f_c , and f_u represent the lower, center and upper frequency for the bandwidth of interest, respectively, the inverse Fourier transform actually computed by UMPE is

$$\tilde{P}'_R(z, (n - n_0) \Delta t) = \frac{1}{N} \sum_{l=l_l}^{l_u} \frac{X(l \Delta f)}{\sqrt{R}} \Psi_{l,R}(z) e^{-i\left(\frac{2\pi}{N}\right)(n - n_0)(l - l_c)} \quad (2.24)$$

yielding $\tilde{P}'_R(z, (n - n_0) \Delta t)$, the set of complex pressure values in depth-(reduced) time space for the designated range.

C. MODAL ARRIVAL TIME COMPUTATION

To compute individual modal arrival time structures, the PE solution must first be decomposed into normal modes. Normal mode decompositions based on the technique of *separation of variables* assume that the ocean is nearly exactly stratified horizontally. In general, range and depth dependent spatially continuous modes exist which are unique harmonics of the ocean waveguide. However, for cases where the ocean acoustic waveguide properties vary with range, these modes are not simply functions of depth where separation of variables can be used. Subsequently, normal mode theory has been generalized for that of an “almost stratified” medium. In ocean acoustics, this theory was first set forth by Pierce (1965) and Milder (1969). It has become common practice for the modes of an exactly stratified ocean to be used as an orthonormal basis set for any general ocean environment. In ocean acoustics, this orthonormal basis set is referred to as

the set of “local normal modes”, and computed as a function of range using the local environmental properties. The result of this approach when applied to the wave equation for a range-dependent environment is a set of coupled differential equations which govern the range variations of the modal amplitudes.

Consequently, it is seen that in a range-dependent environment, the local normal modes do not propagate independently of each other but rather interact continuously with neighboring modes. If, however, the range-dependent changes in sound-speed profile are small and gradual, an adiabatic approximation can be assumed. That is, coupling between modes may be neglected and each normal mode is assumed to propagate independently while it progressively adapts to changes in the environment. Under adiabatic conditions, the largest proportion of wave energy will remain in the same-numbered mode as it propagates through the changing environment. However, it has been shown by Desaubies *et. al.* (1986) that the degree to which the adiabatic approximation can be used is very sensitive to the shape of the sound-speed profile, frequency of propagation, and mode number. Their work points out that when coupling cannot be neglected, there is no simple expression for the modal travel times.

In an attempt to address this difficulty, Shang and Wang (1993) proposed a method of computing modal travel time for range-dependent, strong mode coupling environments which is known as the modal spectrum of the PE field (MOSPEF). It is this method which is used to compute the modal travel times presented in Chapt. V of this dissertation. In MOSPEF, coupled modal amplitude equations are avoided by first computing the total acoustic pressure field solution using the PE method, such as that described in previous sections. Next, using local normal mode functions $\Psi_m(z; r, \omega)$ computed from a normal mode code such as KRAKEN (Porter, 1991), range-dependent modal amplitudes and phase are then calculated.

Using the PE solution for the two-dimensional range-dependent acoustic field, this field is expressed as a summation of local normal modes

$$p_{PE}(r, z; \omega) = \sum_{m=1}^{\infty} \Phi_m(r; \omega) \Psi_m(z; r, \omega) \quad (2.25)$$

where $\Psi_m(z)$ is the local mode solution of the range-dependent Sturm-Liouville eigenvalue equation

$$\frac{d^2}{dz^2}\Psi_m(z) + [k_0^2 n^2(z, r) - K_m^2]\Psi_m(z) = 0 \quad (2.26)$$

evaluated at the local range r and subject to appropriate boundary conditions. In this equation, K_m^2 represents the separation "constant" (which locally assumes a range-independent environment) and $\Psi_m(z)$ denotes the specific mode function associated with this separation constant.

Taking advantage of the orthogonality of the mode functions leads to

$$\Phi_m(r; \omega) = \int P_{PE}(r, z; \omega) \Psi_m^*(z; r, \omega) dz, \quad (2.27)$$

or, by substituting Eq. (2.6) to put Eq. (2.27) in terms of the PE field function

$$\begin{aligned} \Phi_m(r; \omega) &= \left[\int P_0 \sqrt{\frac{R_0}{r}} \Psi_{PE}(r, z; \omega) \Psi_m^*(z; r, \omega) dz \right] e^{ik_0 r} \\ &= r^{-1/2} A_m(r; \omega) e^{ik_0 r} = r^{-1/2} |A_m(r; \omega)| e^{i\phi_m(r; \omega)}. \end{aligned} \quad (2.28)$$

The complex modal amplitude is given by

$$A_m(r; \omega) = \int P_0 \sqrt{R_0} \Psi_{PE}(r, z; \omega) \Psi_m^*(z; r, \omega) dz \quad (2.29)$$

and the modal phase is given by

$$\phi_m(r; \omega) = k_0 r + \text{Arg}[A_m(r; \omega)]. \quad (2.30)$$

Shang and Wang refer to the quantity $|A_m(r; \omega)|$ as the modal repopulation character.

The modal arrival times can be computed similarly to the broadband computation. Using discrete frequencies with the source spectrum denoted by $X(l\Delta f)$, the acoustic pressure field is found from the PE pressure field solution by substituting Eqs. (2.25) and (2.28) into (2.23), thus yielding

$$\tilde{P}(r, z, n\Delta t) = \frac{1}{N} \sum_{l=0}^{N-1} \left(\sum_{m=1}^{\infty} X(l\Delta f) r^{-1/2} |A_m(r; l\Delta f)| \Psi_m(z; r, l\Delta f) e^{i\Phi_m(r; l\Delta f)} e^{-i\left(\frac{2\pi}{N}\right)nl} \right) \quad (2.31)$$

or in terms of the modal pulse

$$\tilde{P}_m(r, z, n\Delta t) = \frac{1}{N} \sum_{l=0}^{N-1} X(l\Delta f) r^{-1/2} |A_m(r; l\Delta f)| \Psi_m(z; r, l\Delta f) e^{i\left(\Phi_m(r; l\Delta f) - \left(\frac{2\pi}{N}\right)nl\right)}. \quad (2.32)$$

If the mode functions are approximately invariant over the frequency bandwidth of consideration, such that

$$\Psi_m(z; r, \omega_l) \approx \Psi_m(z; r, \omega_c) \approx \Psi_m(z; r, \omega_u) \quad (2.33)$$

where ω_l , ω_c , and ω_u are the lower, center, and upper frequencies of the bandwidth under consideration, then Eq. (2.32) can be simplified to

$$\tilde{P}_m(r, z, n\Delta t) = \frac{1}{N} \Psi_m(z; r, l_c \Delta f) \sum_{l=0}^{N-1} X(l\Delta f) r^{-1/2} |A_m(r; l\Delta f)| e^{i\left(\Phi_m(r; l\Delta f) - \left(\frac{2\pi}{N}\right)nl\right)}. \quad (2.34)$$

This simplification reduces the computational burden of computing an FFT for each depth grid point.

In the dissertation work presented here, modal arrival time structures are computed only at designated fixed ranges. The complex modal amplitude $A_m(R; \omega)$ was computed from Eq. (2.29) using the individual frequency-dependent mode functions (rather than the approximate mode function $\Psi_m(z; R, \omega_c)$ when Eq. (2.33) is valid) as computed by the KRAKEN normal mode code. When computing the modal pulse, Eq. (2.32) or Eq. (2.34), the approximate center frequency mode function was used only if Eq. (2.33) was valid. The signal is heterodyned about the center frequency and the overall phase factor is neglected, giving results in terms of “reduced time”. The source spectrum used by UMPE is a Hanning amplitude window. Thus, the Fourier transform actually computed was

$$\tilde{P}'_{R, m}(z, (n - n_0)\Delta t) = \frac{\Psi_m(z; R, l_c \Delta f)}{N} \sum_{l=l_i}^{l_u} \frac{X(l\Delta f)}{\sqrt{R}} A_m(R; l\Delta f) e^{-i\left(\frac{2\pi}{N}\right)(n - n_0)(l - l_c)} \quad (2.35)$$

when Eq. (2.33) was valid or

$$\tilde{P}'_{R, m}(z, (n - n_0)\Delta t) = \frac{1}{N} \sum_{l=l_i}^{l_u} \frac{X(l\Delta f)}{\sqrt{R}} (\Psi_m(z; R, l\Delta f)) A_m(R; l\Delta f) e^{-i\left(\frac{2\pi}{N}\right)(n - n_0)(l - l_c)} \quad (2.36)$$

otherwise. The final result yields $\tilde{P}'_{R, m}(z, (n - n_0)\Delta t)$, the set of modal complex pressure values in depth-(reduced) time space for the designated range.

III. MODE FUNCTIONS FOR THE WIDE ANGLE APPROXIMATION TO THE PARABOLIC EQUATION

With a goal of further developing modal ocean acoustic tomography, Shang and Wang (1993) proposed using the modal spectrum of the PE field for computing modal travel times under strong mode coupling environments. Instead of dealing with the coupled equations governing the complex modal amplitudes, they obtained the coupled modal amplitudes and phases from the spectral expansion of the full wave field given by the PE solution with local normal modes as the basis set. Their results, obtained using a 2-D wide angle implicit finite-difference (IFD) PE code (Lee and Botseas, 1982) and normal mode code KRAKEN (Porter, 1991), presented modal travel time perturbations for the first ten modes due to a single mesoscale eddy.

In a similar type approach, modal decompositions of wide angle PE fields were computed in support of the investigations presented in later chapters. However, computations for the modal amplitudes of a reference range-independent wide angle PE field using standard normal modes erroneously yielded fluctuating rather than constant modal amplitudes for modes higher than about mode 30. This led to the new development and investigation of “wide angle PE mode functions” presented here. The results of Shang and Wang do not contradict these results. Rather, their analysis was limited to only a small number of low-order modes which do not suffer significantly from this mismatch. It should be noted, however, that their analysis did not employ the correct modal basis set, as will be shown in this chapter.

In that PE-based methods are full wave methods providing the total acoustic field on a computational grid, they do not readily supply information regarding the propagation of individual modes. This modal information might assist in interpreting acoustic propagation behavior in a complex environment, or be useful for determining the relative adiabatic nature of a particular environment. Thomson (1993) addressed this issue for the standard parabolic approximation. In his work, he described a PE-based spectral method suitable for modal analysis. Specifically, he demonstrated that the field p in a waveguide

satisfying the acoustic wave equation is exactly related to the field ψ satisfying the SPE approximation. For this case, the modal amplitudes and wavenumbers of ψ can be determined exactly, and the corresponding amplitudes and wavenumbers of the normal modes of the acoustic field p are then obtained by simple mapping rules.

For other higher order parabolic approximations, such as the WAPE and Pade' expansions, the modal eigenfunctions and associated eigenvalues of ψ are distinct from those of the acoustic wave equation. In that the WAPE is a common implementation for PE models using the split-step Fourier technique and is expected to yield more accurate results than the SPE, a better understanding of its "normal modes" is desired.

In this chapter, the parabolic approximation to the wave equation is examined within the context of normal mode theory. Building on the PE theory presented in Chapt. II, approximate mode functions for the split-step Fourier (SSF) WAPE algorithm are developed. These mode functions are then used to decompose range-independent sound-pressure fields computed using the WAPE approximation. The resulting modal coefficients and eigenfunctions obtained using the WAPE mode functions are compared with those obtained using standard normal mode theory. It is important to note in what follows that use of the SSF algorithm does not introduce any additional approximations in terms of the corresponding modal description.

A. THEORETICAL DEVELOPMENT

Normal mode decomposition theory uses the technique of *separation of variables* and is based on the approximation that the ocean is exactly horizontally stratified. Considering only modes within the water column, and assuming constant water density, azimuthal symmetry, and range independence (sound speed varies only with depth), the time-harmonic acoustic field $p(r, z) e^{-i\omega t}$ at $r > 0$ due to a point source at $z = z_s$ and $r = 0$ satisfies the two-dimensional Helmholtz equation

$$\frac{1}{r} \frac{\partial}{\partial r} \left(r \frac{\partial p}{\partial r} \right) + \frac{\partial^2 p}{\partial z^2} + k_0^2 n^2(z) p = 0. \quad (3.1)$$

Seeking solutions in the form $p(r, z) = \Phi(r) \Psi(z)$ yields the well-known depth-dependent modal equation

$$\frac{d^2}{dz^2} \Psi_m(z) + [k_0^2 n^2(z) - K_m^2] \Psi_m(z) = 0 \quad (3.2)$$

which is subject to appropriate boundary conditions. In this equation, K_m^2 represents the separation constant and $\Psi_m(z)$ denotes the specific mode function associated with this separation constant. The complete sum of normalized modes is necessary to represent an arbitrary pressure field. Accordingly, the pressure is expressed as

$$p(r, z) = \sum_{m=1}^{\infty} \Phi_m(r) \Psi_m(z). \quad (3.3)$$

Returning to the relationship between the acoustic field and the envelope function, Eq. (2.6), an alternate approach employing the separation of variables technique to solve the standard parabolic equation, Eq. (2.15), yields an expansion into PE modes. Hereafter, these particular modes will be referred to as SPE modes. In this case, the range-independent expansion is shown by Desanto (1977) to be

$$\psi(r, z) = \sum_{j=1}^{\infty} a_j u_j(z) \exp(is_j r) \quad (3.4)$$

where a_j are the SPE mode amplitudes, $u_j(z)$ are the SPE mode functions, and s_j are the SPE modal wavenumbers.

Thomson (1993) has shown that the depth-dependent SPE mode functions $u_j(z)$ satisfy an eigenvalue equation comparable to that for the normal mode functions of the acoustic wave equation, Eq. (3.2)

$$\frac{d^2}{dz^2}u_j(z) + [k_0^2 n^2(z) - K_j^2]u_j(z) = 0, \quad (3.5)$$

where the SPE modal wavenumbers s_j are given by

$$s_j = \frac{K_j^2 - k_0^2}{2k_0}, \quad (3.6)$$

and the horizontal wavenumbers K_j are the corresponding normal mode eigenvalues of Eq. (3.2). The important issue here is that the mode functions for the SPE approximation exactly match those which solve the acoustic wave equation. Accordingly, these mode functions may be found using a normal mode code such as KRAKEN (Porter, 1991). As we shall see shortly, this is not the case when using the WAPE approximation.

We now seek approximate solutions to Eq. (2.7) replacing \mathcal{Q}_{op} by the approximate propagator function \mathcal{Q}_{WAPE} and assuming

$$\psi(r, z) = \sum_{n=1}^{\infty} \Gamma_n(r) v_n(z). \quad (3.7)$$

Here, $\Gamma_n(r)$ represents the WAPE range dependent modal amplitude and $v_n(z)$ is the WAPE mode function. This expansion for $\psi(r, z)$ leads to the modal equation

$$\frac{ik_0}{v_n(z)} \left[\left(1 + \frac{1}{k_0^2} \frac{d^2}{dz^2} \right)^{1/2} + (n(z) - 1) - 1 \right] v_n(z) - \frac{1}{\Gamma_n(r)} \frac{d}{dr} \Gamma_n(r) = 0. \quad (3.8)$$

Setting the separation constant equal to $i\beta_n$, it can be shown that $\Gamma_n(r)$ has the simple range dependence

$$\Gamma_n(r) = b_n \exp(i\beta_n r) \quad (3.9)$$

where b_n is the modal amplitude and β_n is the associated WAPE modal wavenumber.

Using this separation constant, the WAPE depth-dependent modal equation becomes

$$\left[\left(1 + \frac{1}{k_0^2} \frac{d^2}{dz^2} \right)^{1/2} + (n(z) - 1) - \left(1 + \frac{\beta_n}{k_0} \right) \right] v_n(z) = 0. \quad (3.10)$$

To develop approximations for the WAPE modes, the square root operator is approximated using first order and second order Taylor series expansions. This leads to the first order approximate depth-dependent WAPE modal equation

$$\frac{d^2}{dz^2} v_n(z) + 2k_0^2 \left[n(z) - \frac{\beta_n'}{k_0} \right] v_n(z) \approx 0, \quad (3.11)$$

and to second order

$$\left[\frac{1}{8k_0^4} \frac{d^4}{dz^4} - \frac{1}{2k_0^2} \frac{d^2}{dz^2} - n(z) - \frac{\beta_n'}{k_0} \right] v_n(z) \approx 0. \quad (3.12)$$

where $\beta_n' = \beta_n + k_0$. Note that the terms "first order" and "second order" refer to the relative order of the Taylor series employed. It does not relate to the order of accuracy used during numerical implementation. The first order approximation is essentially a return to the small angle approximation, and is not expected to provide highly satisfactory results in numerical implementation. However, it is included in the analysis to gain insight into the nature of the WAPE mode function and its relationship to the standard normal mode function.

The eigenfunctions satisfying Eqs. (3.10) - (3.12) no longer match those normal mode eigenfunctions associated with the acoustic wave equation. The orthogonality (i.e. uniqueness) of the WAPE modes can be examined as follows. Here we shall only consider the first order approximation, although the orthogonality of the WAPE modes can be shown to be more general. Multiply the first order approximate depth-dependent WAPE modal equation, Eq. (3.11), for $v_n(z)$ by $v_m(z)$ and for $v_m(z)$ by $v_n(z)$.

Subtracting these two equations yields

$$v_m(z) \frac{d^2}{dz^2} v_n(z) - v_n(z) \frac{d^2}{dz^2} v_m(z) = 2k_0 (\beta_n - \beta_m) v_n(z) v_m(z) \quad (3.13)$$

or

$$\frac{d}{dz} \left(v_m(z) \frac{d}{dz} v_n(z) - v_n(z) \frac{d}{dz} v_m(z) \right) = 2k_0(\beta_n - \beta_m) v_n(z) v_m(z). \quad (3.14)$$

Integrating over z and applying the boundary conditions for an ideal waveguide (pressure release surface and pressure release bottom), Eq. (3.14) reduces to

$$(\beta_n - \beta_m) \int_0^D v_n(z) v_m(z) dz = 0. \quad (3.15)$$

The assumption of a pressure release bottom boundary condition in this case is considered appropriate as a penetrable seafloor at low grazing angles reflects similarly to a free surface (Jensen *et. al.*, 1994, p. 108). Note also that the assumption of a pressure release bottom does not greatly alter the resulting modeshapes when considering only deep, trapped modes corresponding to refracted-refracted (RR) paths with no bottom interactions, as will be the case for the remainder of this development and subsequent numerical implementation. Since each modal wavenumber is unique, i.e.

$$\beta_m \neq \beta_n \quad \text{if } m \neq n,$$

$$\int_0^D v_n(z) v_m(z) dz = 0 \text{ for } m \neq n. \quad (3.16)$$

Therefore, the first order approximate WAPE modes form an orthogonal basis set.

To determine the approximate WAPE modal amplitudes, Eqs. (2.4), (2.5), (3.7) and (3.9) are used to establish the far-field WAPE modal solution for the computed WAPE field p in a layered waveguide

$$p(r, z) \approx \left(\frac{2}{i\pi k_0 r} \right)^{1/2} \sum_n b_n v_n(z) \exp(i\beta_n' r) \quad (3.17)$$

where $\beta_n' = \beta_n + k_0$.

B. NUMERICAL IMPLEMENTATION

Finite-difference techniques are used to numerically approximate the wide-angle PE mode functions developed in the previous section. Numerical schemes are developed for the first and second order Taylor series approximations given by Eqs. (3.11) and (3.12).

For the first order approximation Eq. (3.11), a numerical scheme closely following that developed by Jensen *et al.* (1994) for normal modes to the acoustic wave equation is developed. Defining a grid of N equally-spaced points over the depth interval $0 \leq z \leq D$, gives the depth points $z_j = jh$, $j = 0, 1, \dots, N$, where h is the mesh width given by D/N . This then allows us to define the following $O(h^2)$ difference approximations for the first and second derivatives based on forward, centered, and backward difference approximations, respectively,

$$v_j' \approx \frac{v_{j+1} - v_j}{h} + \left[-2k_0 \left(\frac{\omega}{c(z)} - \beta_n' \right) v_j \right] \frac{h}{2}, \quad (3.18)$$

$$v_j'' \approx \frac{v_{j-1} - 2v_j + v_{j+1}}{h^2} + O(h^2), \quad (3.19)$$

$$v_j' \approx \frac{v_j - v_{j-1}}{h} - \left[-2k_0 \left(\frac{\omega}{c(z)} - \beta_n' \right) v_j \right] \frac{h}{2}. \quad (3.20)$$

In the water column, the approximate mode functions must satisfy Eq. (3.11), which in terms of the difference approximations becomes

$$v_{j-1} + \left(-2 + h^2 2k_0 \left[\frac{\omega}{c(z_j)} - \beta_n' \right] \right) v_j + v_{j+1} = 0, \quad j = 1, 2, \dots, N-1. \quad (3.21)$$

As discussed previously, the top and bottom boundary conditions are assumed to be pressure release, giving $v_0 = 0$ and $v_N = 0$. Collecting these equations together, we obtain the eigenvalue problem,

$$\mathbf{A}(\beta_n') \mathbf{v} = 0 \quad (3.22)$$

where \mathbf{A} is a symmetric tridiagonal matrix of order $N-1$ with the diagonal elements defined by

$$d_j = \left(-2 + h^2 2k_0 \left[\frac{\omega}{c(z_j)} - \beta_n' \right] \right), j = 1, 2, \dots, N-1, \quad (3.23)$$

and the off-diagonal elements defined by

$$e_j = 1, j = 1, 2, \dots, N-1. \quad (3.24)$$

To develop a numerical scheme to solve the second order approximation Eq. (3.12), the following $O(h^4)$ centered difference approximations (Godunov and Ryabenkii, 1987) are employed

$$v_j^{iv} = \frac{1}{h^4} \left[-\frac{1}{6} v_{j-3} + 2v_{j-2} - \frac{13}{2} v_{j-1} + \frac{28}{3} v_j - \frac{13}{2} v_{j+1} + 2v_{j+2} - \frac{1}{6} v_{j+3} \right], \quad (3.25)$$

$$v_j'' = \frac{1}{h^2} \left[-\frac{1}{12} v_{j-2} + \frac{4}{3} v_{j-1} - \frac{5}{2} v_j + \frac{4}{3} v_{j+1} - \frac{1}{12} v_{j+2} \right]. \quad (3.26)$$

Substituting into the governing equation

$$v^{iv} - 4k_0^2 v'' - 8k_0^3 \left(\frac{\omega}{c(z)} - \beta_n' \right) v = 0 \quad (3.27)$$

and using a mesh similar to that defined for Eqs. (3.18)-(3.24) gives the resulting equation which must be satisfied in the water column,

$$\begin{aligned} & v_{j-3} + \left(-12 - 2h^2 k_0^2 \right) v_{j-2} + \left(39 + 32h^2 k_0^2 \right) v_{j-1} \\ & + \left(-56 - 60h^2 k_0^2 + 48h^4 k_0^3 \left(\frac{\omega}{c(z)} - \beta_n' \right) \right) v_j + \left(39 + 32h^2 k_0^2 \right) v_{j+1} \\ & + \left(-12 - 2h^2 k_0^2 \right) v_{j+2} + v_{j+3} = 0, \quad j = 3, 4, \dots, N-3. \end{aligned} \quad (3.28)$$

This leads to a seven diagonal banded matrix. Again, pressure release boundaries are assumed, giving $v_0 = 0$ and $v_N = 0$. For $j = 1, 2, N-2, N-1$, the pressure release assumption leads to the following equations,

$$\begin{aligned} & \left(-44 - 58h^2 k_0^2 + 48h^4 k_0^3 \left(\frac{\omega}{c(z)} - \beta_n' \right) \right) v_1 + \left(38 + 32h^2 k_0^2 \right) v_2 \\ & + \left(-12 - 2h^2 k_0^2 \right) v_3 + v_4 = 0, \quad j = 1, \end{aligned} \quad (3.29)$$

$$\begin{aligned} & \left(38 + 32h^2 k_0^2 \right) v_1 + \left(-56 - 60h^2 k_0^2 + 48h^4 k_0^3 \left(\frac{\omega}{c(z)} - \beta_n' \right) \right) v_2 \\ & + \left(39 + 32h^2 k_0^2 \right) v_3 + \left(-12 - 2h^2 k_0^2 \right) v_4 + v_5 = 0, \quad j = 2, \end{aligned} \quad (3.30)$$

$$\begin{aligned} & v_{N-5} + \left(-12 - 2h^2 k_0^2 \right) v_{N-4} + \left(39 + 32h^2 k_0^2 \right) v_{N-3} \\ & + \left(-56 - 60h^2 k_0^2 + 48h^4 k_0^3 \left(\frac{\omega}{c(z)} - \beta_n' \right) \right) v_{N-2} \\ & + \left(38 + 32h^2 k_0^2 \right) v_{N-1} = 0, \quad j = N-2, \end{aligned} \quad (3.31)$$

$$\begin{aligned} & v_{N-4} + \left(-12 - 2h^2 k_0^2 \right) v_{N-3} + \left(38 + 32h^2 k_0^2 \right) v_{N-2} \\ & + \left(-44 - 58h^2 k_0^2 + 48h^4 k_0^3 \left(\frac{\omega}{c(z)} - \beta_n' \right) \right) v_{N-1} = 0, \quad j = N-1 \end{aligned} \quad (3.32)$$

In the following section, results from these numerical approximations will be shown.

The eigenvectors of the matrices defined by Eqs. (3.23)-(3.24) and (3.28)-(3.32) represent the first order and second order Taylor series approximations, respectively, to the WAPE mode functions $v_n(z)$ in Eq. (3.16). The matrix eigenvalues represent the associated wide-angle PE modal wavenumbers β_n .

To determine the modal amplitudes, it is useful to write Eq. (3.17) as

$$\sqrt{rp}(r, z) \approx \left(\frac{2}{i\pi k_0} \right)^{1/2} \sum_n b_n v_n(z) \exp(i\beta_n' r) = \sum_n A_n(r) v_n(z) \quad (3.33)$$

where A_n is the desired modal amplitude. This expression is general and does not depend on which approximation to the WAPE is used. Note that we have accounted for cylindrical spreading losses by scaling $p(r, z)$ by \sqrt{r} . Then assuming normalized modes and invoking orthogonality, it can be shown that at a given range the modal amplitude is given by

$$A_m(r) = \sqrt{r} \int_0^D \frac{p(z, r) v_m(z)}{\rho(z)} dz. \quad (3.34)$$

In the following section, modal amplitudes for a range-independent, open ocean environment are computed.

C. NUMERICAL RESULTS

The numerical schemes developed for the first and second order approximations to the WAPE mode function were tested assuming a range-independent, deep ocean environment characterized by the Munk canonical sound speed profile (Munk, 1974)

$$[c(z) - c_o] / c_o = \epsilon (e^\eta - \eta - 1) \quad (3.35)$$

where $\epsilon=0.0057$, the scaled depth variable $\eta = 2(z-z_{axis})/B$, and the reference sound speed c_o was chosen as 1490 m/s. Axis depth, z_{axis} , was assumed to be -1.0 km. The bottom depth was assumed to be -4.5 km.

The acoustic pressure field was computed out to a range of 100 km using the University of Miami PE (UMPE) model (Smith and Tappert, 1993) employing the wide angle approximation. Input run parameters are summarized by Table 1. As was discussed in Chapt. II.A.3, the computational depth includes the water column of interest (bottom depth listed) and a “finite-depth fluid bottom halfspace”. This halfspace extends to the computational depth and is terminated with an artificial absorption layer to meet the radiation condition. The resulting pressure field was then decomposed into standard normal modes using KRAKEN (Porter, 1991), and first and second order approximation WA modes by finding the eigenvectors of the matrices defined by Eqs. (3.23)-(3.24) and (3.28)-(3.32) respectively.

These mode functions were then used to compute the respective modal amplitude coefficients at 1 km intervals out to 100 km using Eq. (3.34). For a range-independent environment, these coefficients should remain constant with range. Plots of selected modal coefficient amplitudes for the three different mode functions are provided by Figs.

Parameter	Value
Reference sound speed, c_{ref}	1490 m/s
Frequency, f	100 Hz
Source Level	183 dB re 1 μ Pa
Source Spectrum	Hanning amplitude window
Source Depth	1000 m
Bottom Depth	4500 m
Computational Depth	8000 m
Transform size	8192
Depth grid step	0.9765 m
Range grid step	10.0 m

Table 1. Acoustic propagation model (UMPE) input run parameters used to compute WAPE solution for the modeled range-independent deep ocean environment.

1-3. Modes were selected so as to minimize overlapping line segments on the plots. Only non-bottom interacting modes were considered, as the numerical scheme for the second order WAPE mode functions currently only treats the bottom as a pressure release surface.

For the lower modes depicted by Fig. 1, all three methods provide satisfactory demonstration of range-independence. However, the first order WAPE mode function approximation starts to show some small fluctuations for mode numbers greater than 15. In Fig. 2, the first order approximation clearly breaks down as the mode number increases.

Additionally, the standard normal mode decomposition of the WAPE computed field begins to show noticeable fluctuations for modes above mode 35. Only the second order approximation demonstrates satisfactory range-independence. As the mode number is increased further, the fluctuations in both the SPE and first order approximations continue to increase. This is illustrated in Fig. 3. Again, the second order approximation continues to demonstrate the range-independent nature of the input sound-speed

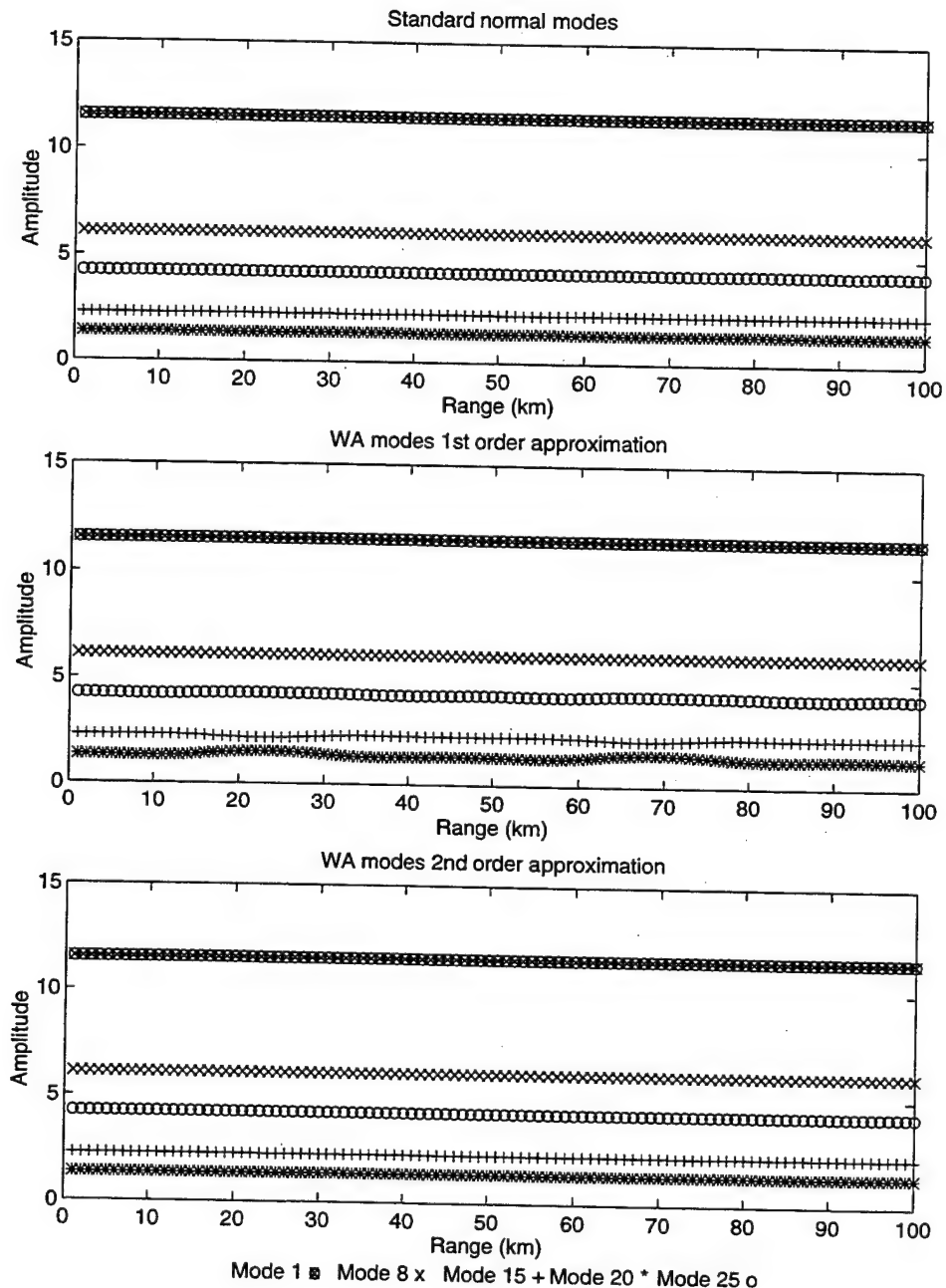


Figure 1. Modal coefficient amplitudes as a function of range for modes 1, 8, 15, 20 and 25 of a range-independent Munk canonical sound speed profile. Mode shapes were determined using standard normal mode theory and first and second order approximations to the wide angle mode function.

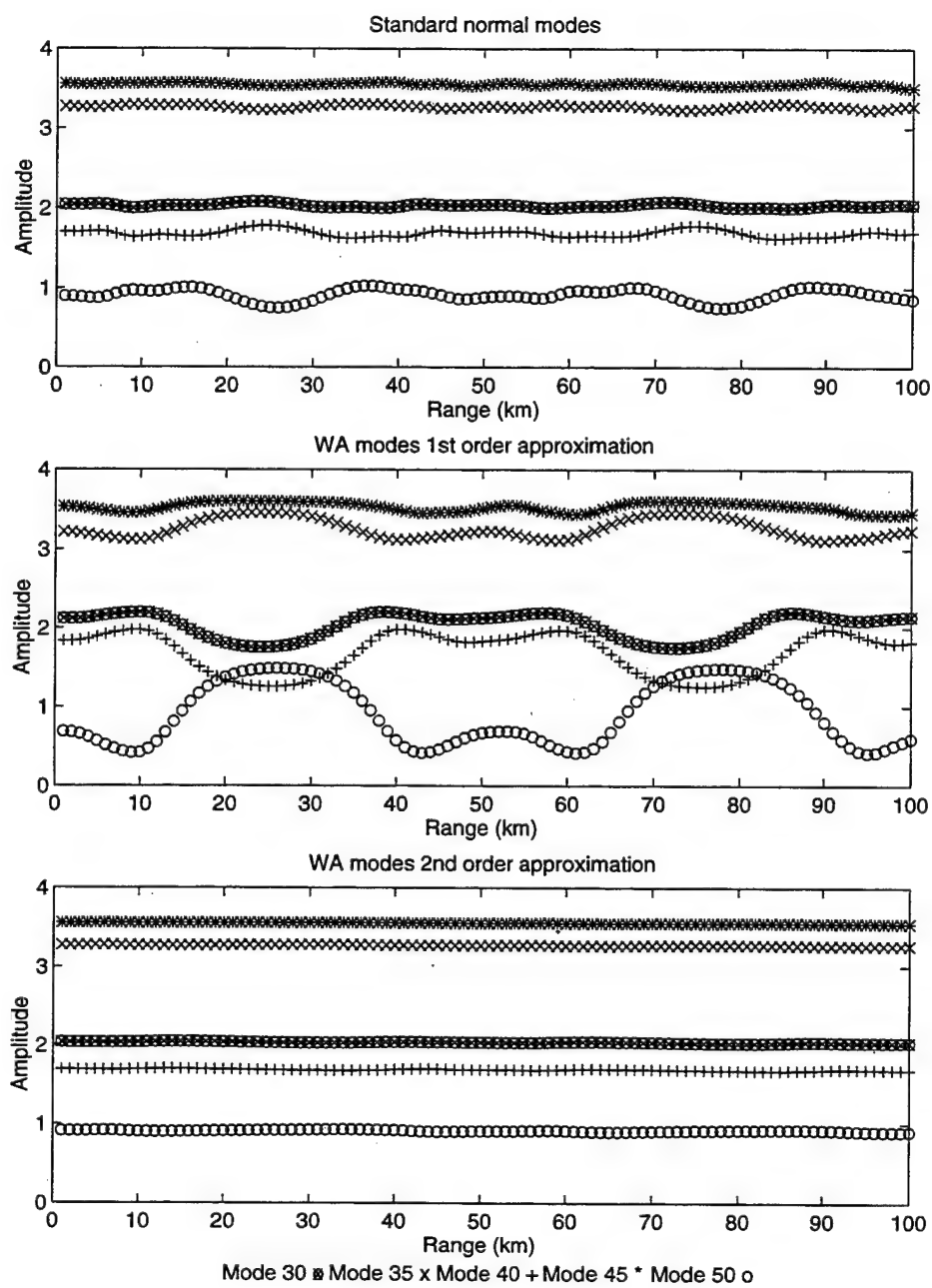


Figure 2. Same as Fig. 1 except for modes 30, 35, 40, 45, and 50.

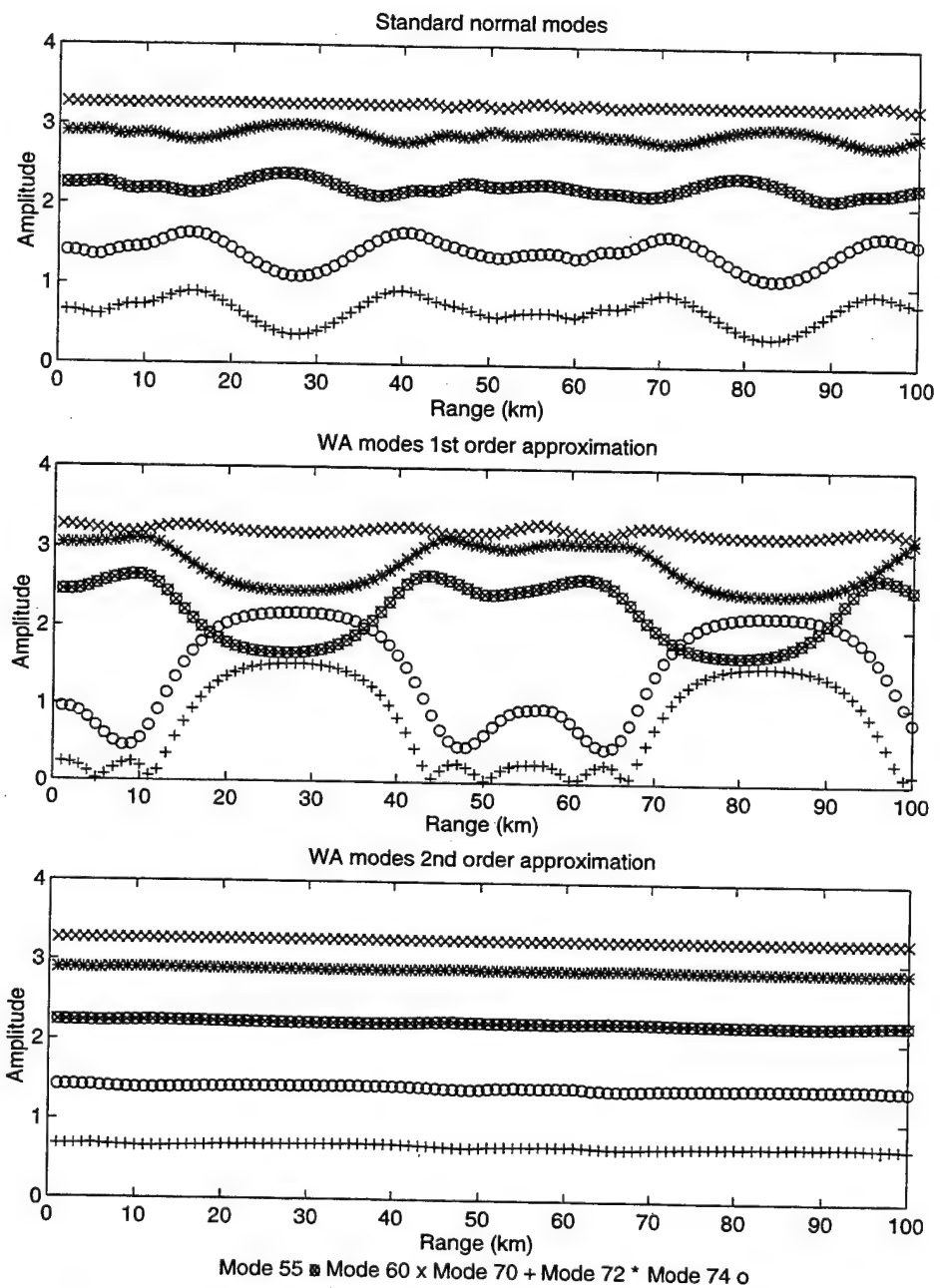


Figure 3. Same as Fig. 1 except for modes 55, 60, 70, 72, and 74.

environment. This pattern was observed up through mode 100, the highest mode computed in this work.

The differences are relatively small between the mode shapes computed using standard normal mode theory and the second order approximation to the WAPE mode function derived in this chapter. Figure 4 illustrates the difference between these two mode functions for mode 70. For this particular sound speed profile, the mode shapes derived using the two methods tended to converge at low mode numbers, and slowly diverge as the mode number increased. That such small differences in mode shapes would generate significant errors in the mode amplitude decomposition is both an interesting and important finding of this dissertation.

Finally, in that a portion of the work in this dissertation uses mode functions to compute modal travel times, a comparison of modal travel times computed using standard normal mode functions and the second order approximate WAPE mode functions is depicted by Fig. 5. For the results presented in Chapt. V, standard normal mode functions were used to compute modal travel times. This choice was made for two primary reasons. The first reason is that we were interested in statistical trends in the data rather than absolute times. The relatively small difference in travel time results between the two methods as represented by Fig. 5 was deemed acceptable for these trends. The second reason is that the numerical implementation for second order approximate wide angle mode functions developed in this chapter does not yet allow transmission across an interface or the incorporation of a density contrast, such as was required for the water column / bottom layer interface in Chapt. V.

D. SUMMARY

This chapter has examined how the wide angle approximation to the PE square root operator alters the associated mode functions in a normal mode decomposition. Specifically, first order and second order Taylor series approximations to the WAPE mode functions were developed and compared to SPE mode functions. While the field ψ

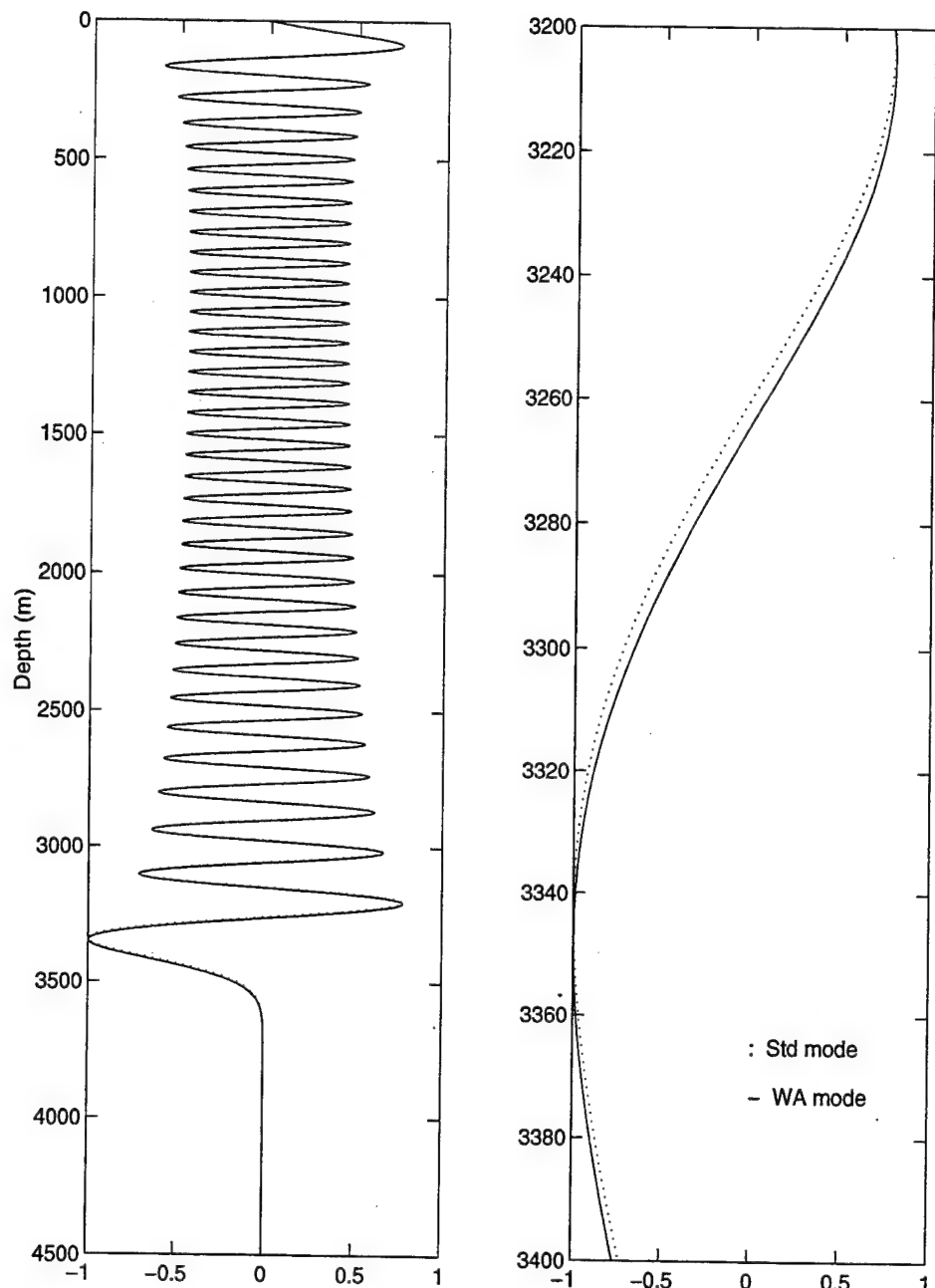


Figure 4. Comparison of mode 70 as computed using standard normal mode theory and the second order approximation to the wide angle mode function. The left hand side depicts the modeshape over the entire water column. The right hand side provides an enlargement of the 3200-3400 m depth to more clearly depict the difference in mode shape.

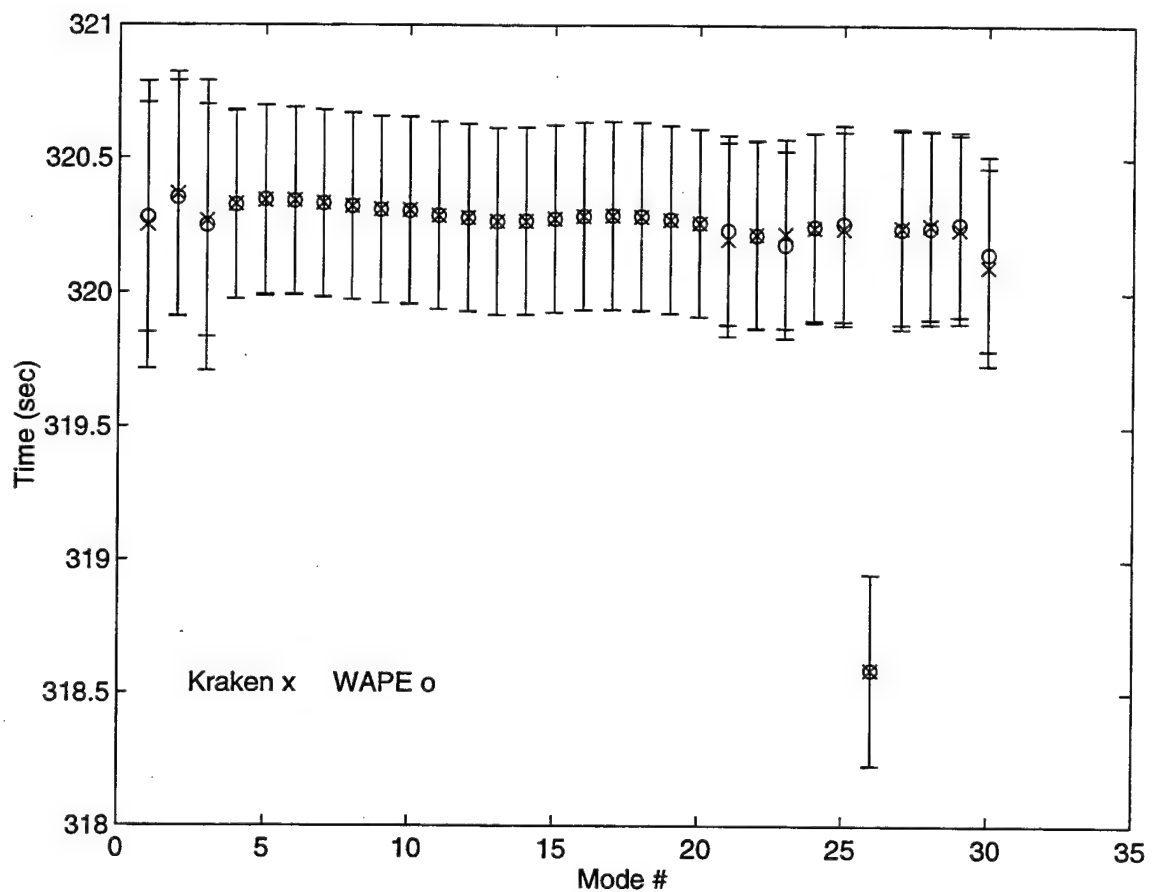


Figure 5. Comparison of arrival times computed using standard normal modes (KRAKEN) and second order approximate WAPE modes. Data illustrates the arrival times computed for data set 36 (95Jul07) as described in Chapt. V. The x,o plots the centroid of the arriving acoustic energy, and the errorbar plots the first standard deviation of energy distribution about the centroid. The mean difference in arrival times over the 30 modes was 2 (± 15.9) msec., with the positive mean indicating that the WAPE mode functions tended to predict a slightly earlier arrival (for this environment) relative to the decomposition estimates using standard normal modes.

satisfying the SPE approximation is exactly related to the field p which solves the acoustic wave equation, this is not the case for the WAPE approximation.

Numerical schemes were developed to compute the approximate WAPE mode functions and wavenumbers. The computed mode functions were then used to decompose a typical deep ocean range-independent sound-pressure field obtained using the WAPE approximation. The resulting modal amplitudes obtained using the WAPE mode functions were compared with those obtained using a standard normal mode decomposition of the WAPE field. The second order approximation to the WAPE mode function showed noticeably less fluctuation in the computed modal amplitudes for the modeled range-independent environment in comparison to the standard mode shapes above mode 35. The first order approximation to the WAPE mode function, although simpler to implement numerically, did not provide an adequate representation of the range-independent nature of the modeled environment.

The purpose of this chapter was to highlight the need for a different set of mode functions in normal mode expansions for parabolic approximations to the acoustic wave equation other than the SPE approximation. While the second order Taylor series approximation to the WAPE mode function derived in this chapter showed promising results for the simplified deep ocean environment, much remains to be done to develop proper numerical treatment of interfaces, bottom boundaries, and density gradients. For the modal arrival analysis accomplished in support of Chapt. V, the KRAKEN normal mode theory was used to compute modal arrival times.

IV. TRAVEL TIME BIAS DUE TO OPEN OCEAN ROSSBY WAVES

In this chapter, the effects of randomly phased baroclinic Rossby waves on acoustic travel time and arrival patterns are investigated. Rossby waves are characterized by a small sea-surface signature (10 cm or less), slow propagation speeds (of order 10 cm s^{-1} or less), and long wavelengths (hundreds to thousands of km). It has been speculated that these waves are responsible for the westward intensification of circulation gyres (Chelton and Schlax, 1996). It will be shown that the perturbations resulting from this random mesoscale structure produces an overall spreading in the arrival structure, primarily producing a delay (cold bias) in the axial arrivals.

While other investigators using various methods of analysis have reported a non-linear mesoscale bias which particularly affects the late arrivals (e.g., Mercer and Booker, 1983, Smith, Brown and Tappert, 1992a, 1992b, Athanassoulis and Skarsoulis, 1995), an extensive literature search found no full-wave field studies which specifically address the variability in the observed bias for a field composed of randomly phased Rossby waves. A further understanding of this bias effect and its variability could provide improved predictions of acoustic pulse propagation and provide insights into methods which correct for this bias in ocean monitoring efforts such as ATOC.

A. THE MODELED OCEAN ENVIRONMENT

Earlier investigations (Smith, Brown, and Tappert, 1992b) with Rossby waves suggested that such mesoscale features could significantly perturb the near-axial propagation. As a follow-on to this previous work in studying the variability in the observed perturbations, a similar modeled ocean environment was used in this analysis. Major features of the model along with analytic expressions for both the background and perturbation sound-speed fields are provided below. Expressions for the sound-speed fields

assume the Brunt-Väisala (buoyancy) frequency has the exponential form

$$N(z) = N_0 e^{z/B}, \quad (4.1)$$

where $B = 1$ km, $N_0 = 3$ cycles/h, and the depth z increases upward. The ocean surface and bottom are assumed to be flat, perfectly reflecting interfaces at depths $z=0$ and -4.5 km, respectively. The range-independent background sound-speed field consistent with this exponential form of the buoyancy frequency can be defined by the Munk canonical profile (Munk, 1974)

$$[c(z) - c_o] / c_o = \epsilon (e^\eta - \eta - 1), \quad (4.2)$$

where $\epsilon=0.0057$, the scaled depth variable $\eta = 2(z-z_{axis})/B$, and the reference sound speed c_o is chosen as 1490 m/s. Axis depth, z_{axis} , is assumed to be -1.0 km.

To simulate realistic mesoscale ocean features, the modeled environment contains a superposition of several modes of randomly phased baroclinic Rossby waves. Chiu and Desaubies (1987) have shown that this superposition is appropriate for modeling an open ocean environment away from strong boundary currents. The wave structure produces vertical water displacements of the water column, $\zeta(x,y,z,t)$. The coordinate system is aligned so that x , y , and z increase to the east, north, and upwards respectively. The sound-speed perturbation $\delta c(z,x)$ due to this mesoscale structure can be computed from a knowledge of $N(z)$ and the vertical water displacement $\zeta(x,y,z,t)$ (Munk and Zachariasen, 1976). Smith *et. al.* (1992b) have further shown that this sound-speed perturbation can be computed from

$$\frac{\delta c(z,x)}{c_o} = f_o \frac{\mu}{g} V_o \sum_j \frac{A_j}{k_j} \frac{d}{dz} \phi_j(z) \cos(k_j x + \alpha_j), \quad (4.3)$$

with

$$\frac{d}{dz} \phi_j(z) = -C_j e^{2z/B} \left(Y_0[\xi_j(z)] - \frac{Y_0[\xi_j(0)]}{J_0[\xi_j(0)]} (J_0[\xi_j(z)]) \right), \quad (4.4)$$

where $\xi_j(z) = C_j B e^{z/B}$. In Eq. (4.3), f_o is the Coriolis parameter, which we have assumed to be 1 cycle/day corresponding to a latitude of 30° , $\mu = 24.5$, $g = 9.8 \text{ m/s}^2$ is the gravitational acceleration, and V_o is the perturbation strength parameter in m/s. Each mode is assigned a weight A_j , wavenumber k_j , and random [uniform on $(0, 2\pi)$] phase α_j . In Eq. (4.4), the mode parameters C_j are selected to satisfy the bottom boundary condition

$$Y_0(C_j B e^{-H/B}) - [Y_0(C_j B) / J_0(C_j B)] J_0(C_j B e^{-H/B}) = 0. \quad (4.5)$$

In the work reported here, the first four baroclinic modes are included in the modal expansion. General experience has shown the lowest few modes contain most of the energy (Munk, Worcester, and Wunsch, 1995). Accordingly, mode parameter values were assigned so that the normalized modal energies dropped exponentially with increasing mode number. Assigned mode parameter values are $\lambda_j = 2\pi/k_j = 400, 350, 300, 250 \text{ km}$ and $A_j = 1.0000, 0.5157, 0.3276, 0.2236$ for $j = 1, 2, 3, 4$ respectively. These parameters then provide normalized modal energies which scale as $(A_j/k_j)^2$ of 1.00: 0.20: 0.06: 0.02.

The work of Smith, Brown and Tappert (1992b) reported that the threshold perturbation strength for the onset of easily detectable chaotic ray behavior appeared to lie between $V_o = 0.125 \text{ m/s}$ and $V_o = 0.25 \text{ m/s}$, perturbation strengths typical of the mid- to low-latitude regions of the world's ocean. To explore this same perturbation strength range, a set of twenty numerical prediction realizations were performed with V_o set first to 0.125 m/s and then twenty more realizations with V_o set to 0.25 m/s. These strength parameters produced maximum sound speed perturbations of approximately 6 m/s and 12 m/s respectively.

For each of the twenty range-dependent realizations with V_o set to 0.125 m/s, the phase α_j was randomly assigned. However to allow direct comparison between data sets, the same set of random phases was used for the twenty range-dependent realizations with V_o set to 0.25 m/s. Table 2 lists the assigned phase values used for each of the four baroclinic modes in each realization. Additionally, the location of the local sound speed

axis at the initial range step was directly influenced by the phase of the random mesoscale structure and the perturbation strength. Table 2 also provides the resulting depth of the local sound speed axis and the corresponding minimum sound speed at this local axis for each perturbation strength. In all realizations, the assigned mesoscale sound speed structure is assumed "frozen" in time over the pulse propagation period. Small-scale fluctuations such as those caused by internal waves are not considered.

A typical realization of the sound-speed structure for $V_o=0.125$ m/s is shown in Fig. 6. The perturbations in this particular realization range from approximately -5.3 to 6.1 m/s relative to the background sound speed profile. Figure 6 also provides the sound-speed perturbation envelope referenced to the range-independent canonical profile. Figure 7 provides a similar illustration of the sound-speed structure for the case $V_o=0.25$ m/s. In this case, the perturbations range from -10.7 to 12.2 m/s. For both perturbation strengths, the perturbation is essentially confined to the upper half of the water column. Note that the range-dependence of these perturbations is sinusoidal. Although the sound speed perturbation will average to zero over long range, the travel time perturbation is non-linear and will not average to zero.

B. ACOUSTIC PROPAGATION MODELING

Numerical predictions of the acoustic propagation were obtained from a modified version of the UMPE model (Smith and Tappert, 1993). UMPE is a broadband, range-dependent parabolic equation model which implements the split-step Fourier (SSF) method described previously in Chapt. II. It was modified to include a subroutine for generating the random mesoscale perturbation and superimposing these perturbations onto the background sound speed profile. Input run parameters used for acoustic propagation modeling are summarized by Table 3.

A continuous wave pulse, wide-angle acoustic source function was used to generate the starting field for multiple frequencies. The solutions are then inverse Fourier transformed to yield travel times. The modeled source has a 100 Hz center frequency,

	Randomly assigned phase value for baroclinic mode number				$V_0=0.125$		$V_0=0.25$	
Run	1	2	3	4	Axis Depth (m)	Sound Speed (m/s)	Axis Depth (m)	Sound Speed (m/s)
1	0.4437	2.0744	0.0500	3.5025	1039	1491	1100	1492
2	2.9363	6.1271	0.9400	1.2410	836	1489	695	1486
3	2.4603	2.2026	6.1550	1.2024	898	1488	845	1486
4	1.4359	3.2068	3.1620	1.8819	1074	1490	1118	1490
5	5.6134	1.9929	5.1243	3.3137	1065	1491	1136	1492
6	5.6213	6.0501	5.7924	3.3372	1012	1492	1083	1494
7	1.0054	0.1503	5.9521	1.7476	962	1491	872	1492
8	2.6148	2.1163	2.1666	1.5559	971	1488	951	1487
9	2.6314	1.6137	0.2810	3.0539	1050	1491	704	1486
10	1.0813	5.4430	4.9802	6.2065	1033	1490	986	1491
11	2.5339	2.9236	1.3976	0.6285	945	1488	916	1486
12	0.8081	3.6260	3.2656	0.7081	945	1488	1136	1490
13	1.5948	2.9414	1.8233	3.9961	1024	1489	1065	1489
14	0.6205	6.0390	0.7910	5.8630	1042	1492	986	1493
15	0.4336	0.7553	1.8742	4.2228	1042	1491	1197	1493
16	5.3948	5.1485	5.0633	4.8832	1138	1491	1047	1492
17	1.4660	0.9852	6.0588	6.1911	1006	1490	880	1490
18	0.2466	1.7549	2.9578	2.5819	989	1488	1241	1492
19	3.2380	3.7665	0.2168	0.3478	998	1490	854	1484
20	1.0107	3.6465	2.8894	6.2395	1050	1492	1109	1490

Table 2. Assigned baroclinic mode phase values with resulting local sound speed axis depths and axis sound speeds at the initial range step.

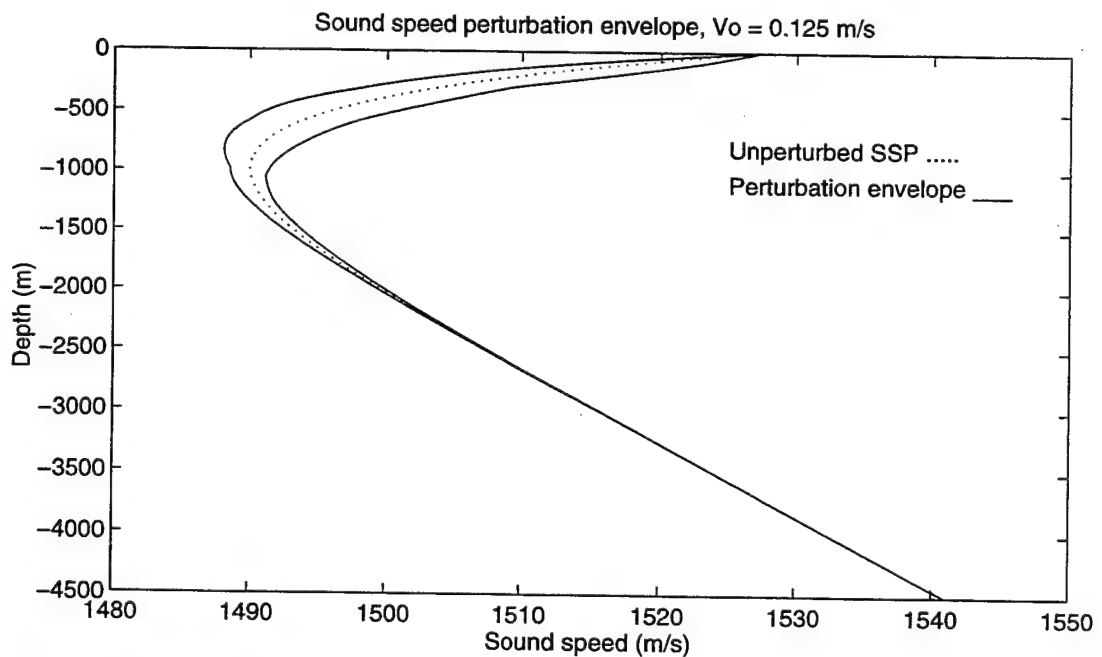
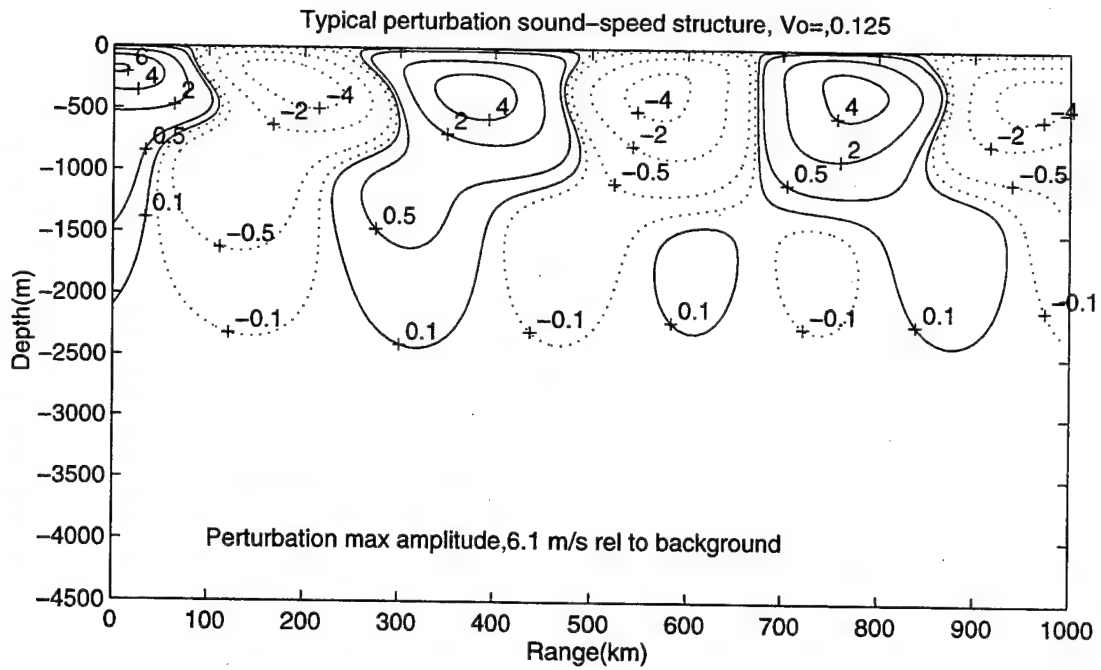


Figure 6. Sound speed perturbation field realization for $V_0=0.125$ m/s. The upper panel displays the sound speed perturbation field relative to the unperturbed background sound speed field. The lower panel compares the background sound speed profile with the envelope of the perturbed profiles.

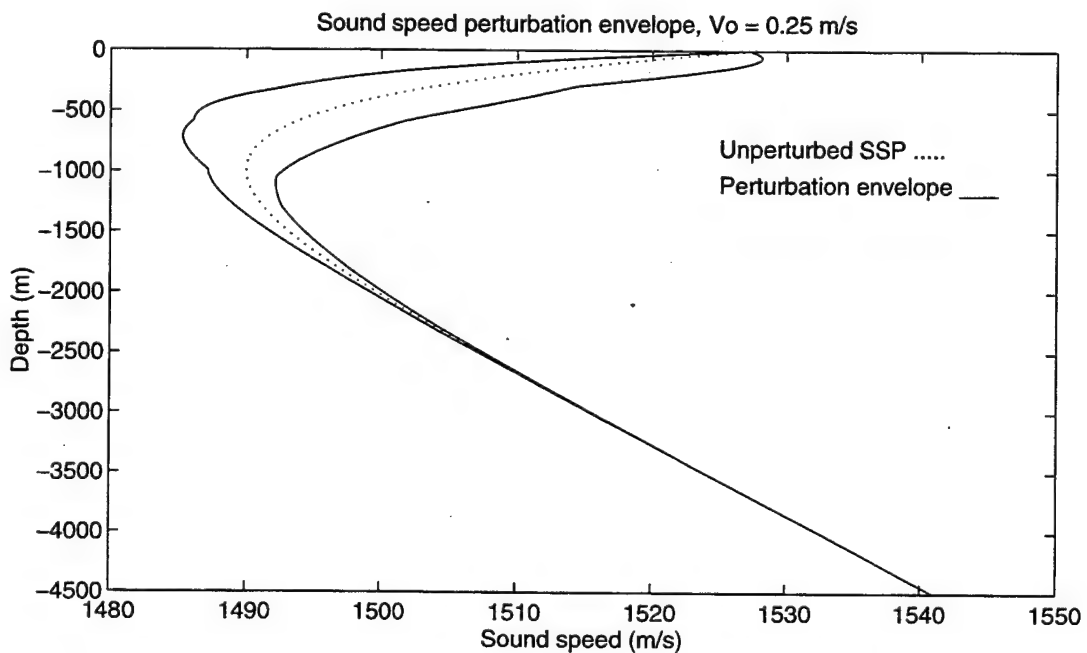
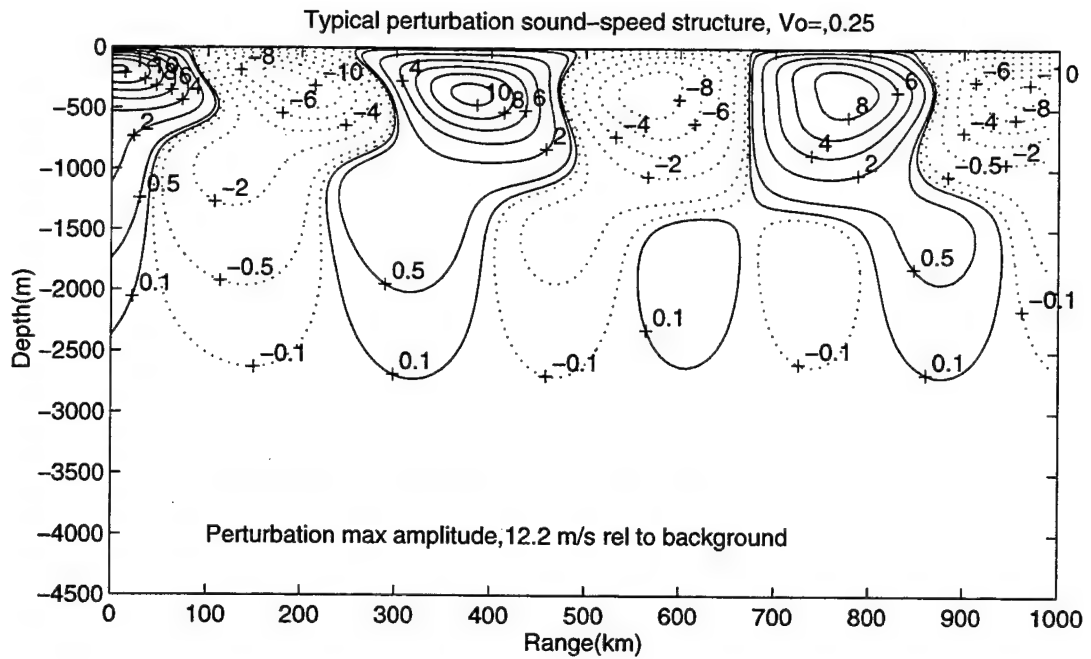


Figure 7. Sound speed perturbation field realization for $V_0=0.25$ m/s. The upper panel displays the sound speed perturbation field relative to the unperturbed background sound speed field. The lower panel compares the background sound speed profile with the envelope of the perturbed profiles.

Parameter	Value
Type of PE approximation	Wide-angle
Reference sound speed, c_0	1490.0 m/s
Number of points in depth	2048
Computational depth	9000.0 m
Depth mesh size	8.8 m
Range step size	50.0 m
Maximum range	1000.0 km
Center frequency	100.0 Hz
Number of frequencies	512
Frequency bandwidth	100.0 Hz
Frequency bin spacing	0.195 Hz
Source depth	Varied, placed at local sound speed axis, which varied up to ± 200 m from background sound speed axis at 1000 m.
Source level	200 dB re 1 μ Pa
Source spectrum	Hanning amplitude window
Angle of the beam center	0.00 deg
RMS half-width angle	35.00 deg
Taper	15.00 deg

Table 3. Acoustic propagation model (UMPE) input run parameters for deep ocean environment with mesoscale structure.

100 Hz bandwidth sampled at 512 discrete frequencies, and 200 dB re $1\mu\text{Pa}$ source level. The UMPE code generates the frequency bin spacing and assumes a Hanning amplitude window for the source spectrum. The pulse length is not an input parameter. A wide-angle source starting function (Thomson and Chapman, 1983) was used with a D/E angle of 0° and a half-width of 35° . A smooth filter was applied to the outer 15° to reduce the influence of sidelobes. To ensure the lowest modes were excited in each realization, the source was placed at the local sound speed axis, the depth of which varied by as much as 200 meters from the assumed background axis depending on the specific perturbation field.

To numerically predict the propagation field, a computational depth of 9000 m was used with a total transform size of 2048, thus providing for a depth mesh of 8.8 m. The projected field was computed out to a range of 1000 km using a range step of 50 m. Twenty range-dependent realizations for each perturbation strength V_0 were computed using the randomly-phased baroclinic modes as per Table 2. Next, a range-averaged sound speed profile was computed for each realization using the range-dependent sound speed profiles at 1 km steps up to the range of interest. To investigate the bias in travel time resulting from the mesoscale structure, forty additional realizations for each perturbation strength were then computed. Twenty each realizations were computed out to 500 km and 1000 km ranges using the respective range-averaged sound speed profile. Note, that while this use of the range-averaged sound speed profile will result in a range-independent environment, the range-averaged sound speed profile may differ slightly from the background Munk canonical profile (no perturbation). From the computed fields, the solutions are inverse Fourier transformed to yield travel times.

A typical plot of the computed broadband transmission loss field for the range-dependent case with $V_0=0.125$ m/s is provided in Fig. 8. In computing the FFTs, the time domain is heterodyned around the value $t_0 = R/c_0$. The time scale axis then uses “reduced time” or $(t-t_0)$ for the arrival time. Some wrap-around of the signal is observed due to the finite transform size. Note that the arrival structure even for the latest arrival is well-defined, suggesting an adiabatic nature of the propagation.

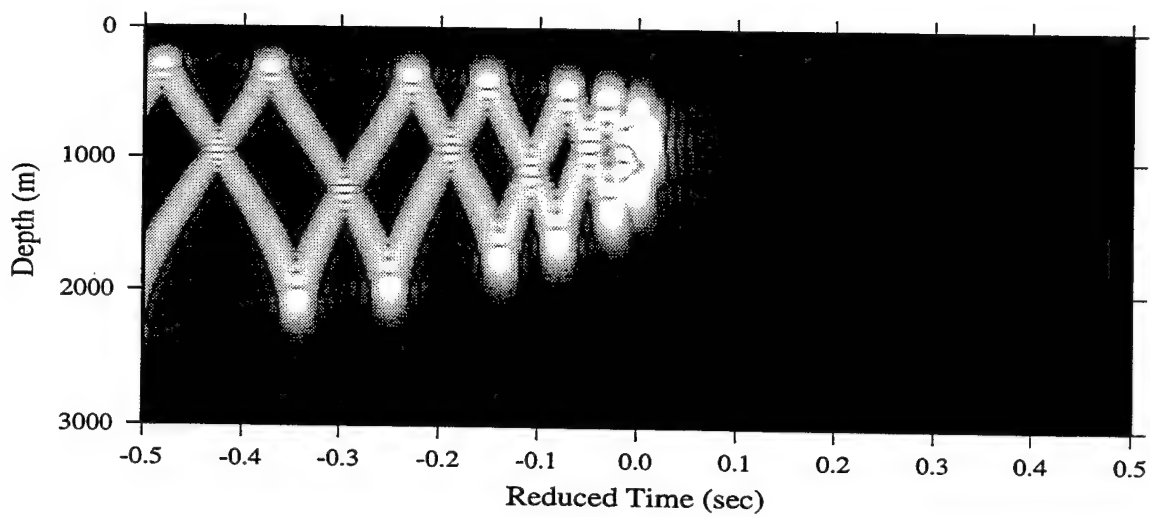
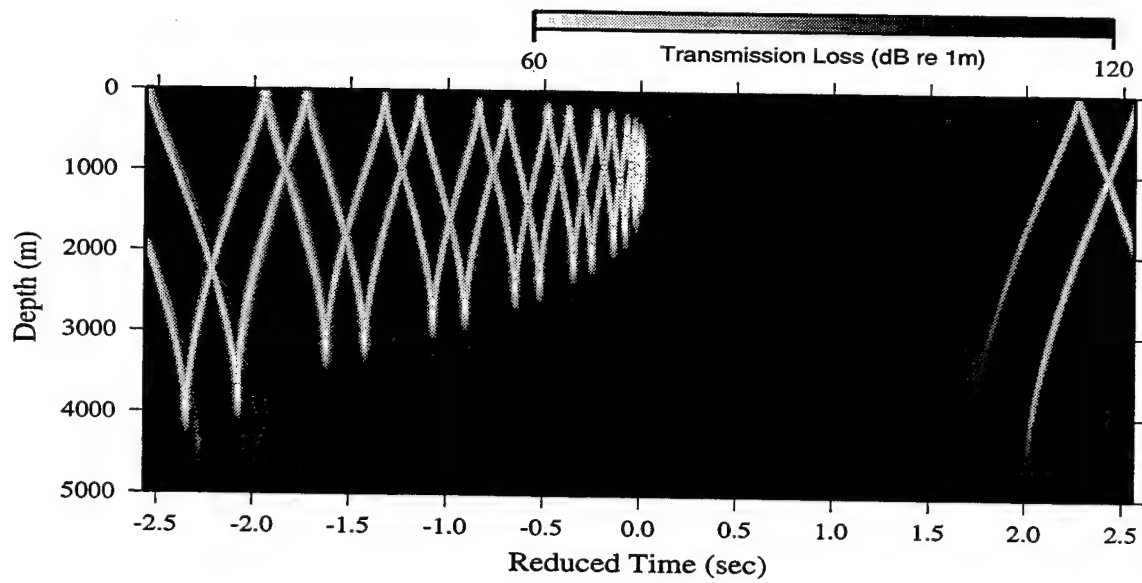


Figure 8. Transmission loss arrival time structure at range 1000 km for $V_0=0.125$ m/s. Upper panel shows total structure of the range-dependent realization. Lower panel shows expanded view of axial arrivals.

To further assess the relative adiabatic nature of the modeled environment, a modal decomposition was performed on a single frequency (100 Hz) range-dependent realization (#7) using the second order approximate wide angle mode functions described in Chapt. III. Results are provided by Fig. 9. At perturbation strength $V_0=0.125$ m/s, there is only a limited amount of mode coupling. However, as the perturbation strength is increased to $V_0=0.25$ m/s, mode coupling starts to increase.

Representative arrivals at the 1000 m depth and 500 km range are depicted in Fig. 10. In the upper panel, the arrival structure of a range-dependent realization for $V_0=0.25$ m/s is compared with its range-averaged realization. The lower panel shows an expanded version of the first and last arrivals. Figure 11 provides similar illustrations for the 1000 km range. In all but one of the range-dependent realizations computed for both $V_0=0.125$ m/s and $V_0=0.25$ m/s, the latest peak arrival at the 1000 km range was delayed from that of the range-averaged case.

C. DATA ANALYSIS AND DISCUSSION

For this modeled environment, we are interested in characterizing the overall spreading in the arrival structure envelope of the range-dependent realization relative to its range-averaged counterpart. In particular, we wish to determine if there is a statistically significant bias in the near-axial arrival structure. The data analysis will refer to the data in four sets based on the combinations of range (500 km, 1000 km) and perturbation strength (0.125 m/s, 0.25 m/s).

The first step in analyzing the data was to measure the arrival envelope lengths. Employing the technique of using arrival times as the time instants corresponding to the significant maxima (peaks) of the arrival pattern (Athanssoulis and Skarsoulis, 1995), the arrival envelope length was determined by measuring the time difference between peaks of the first and last arrivals. Only peaks with less than 100 dB re 1 m transmission loss were considered part of the arrival structure. In those cases where the first arrival “wrapped around” due to the finite transform window, the relative time was adjusted

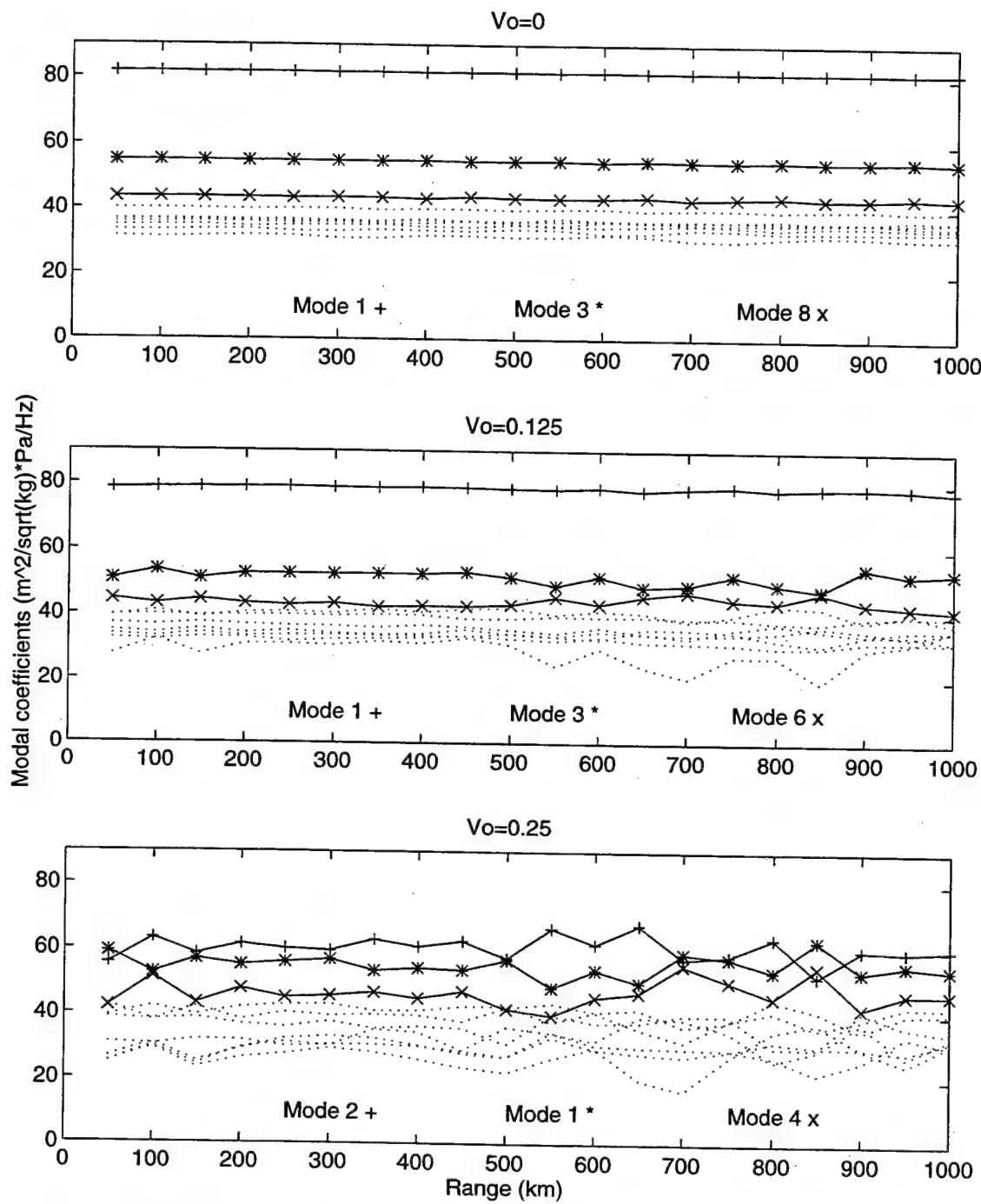


Figure 9. Representative modal decomposition of computed single frequency (100 Hz) pressure fields. Amplitudes for the ten modes having the largest amplitudes are plotted. Only the three modes with the largest amplitudes are identified.

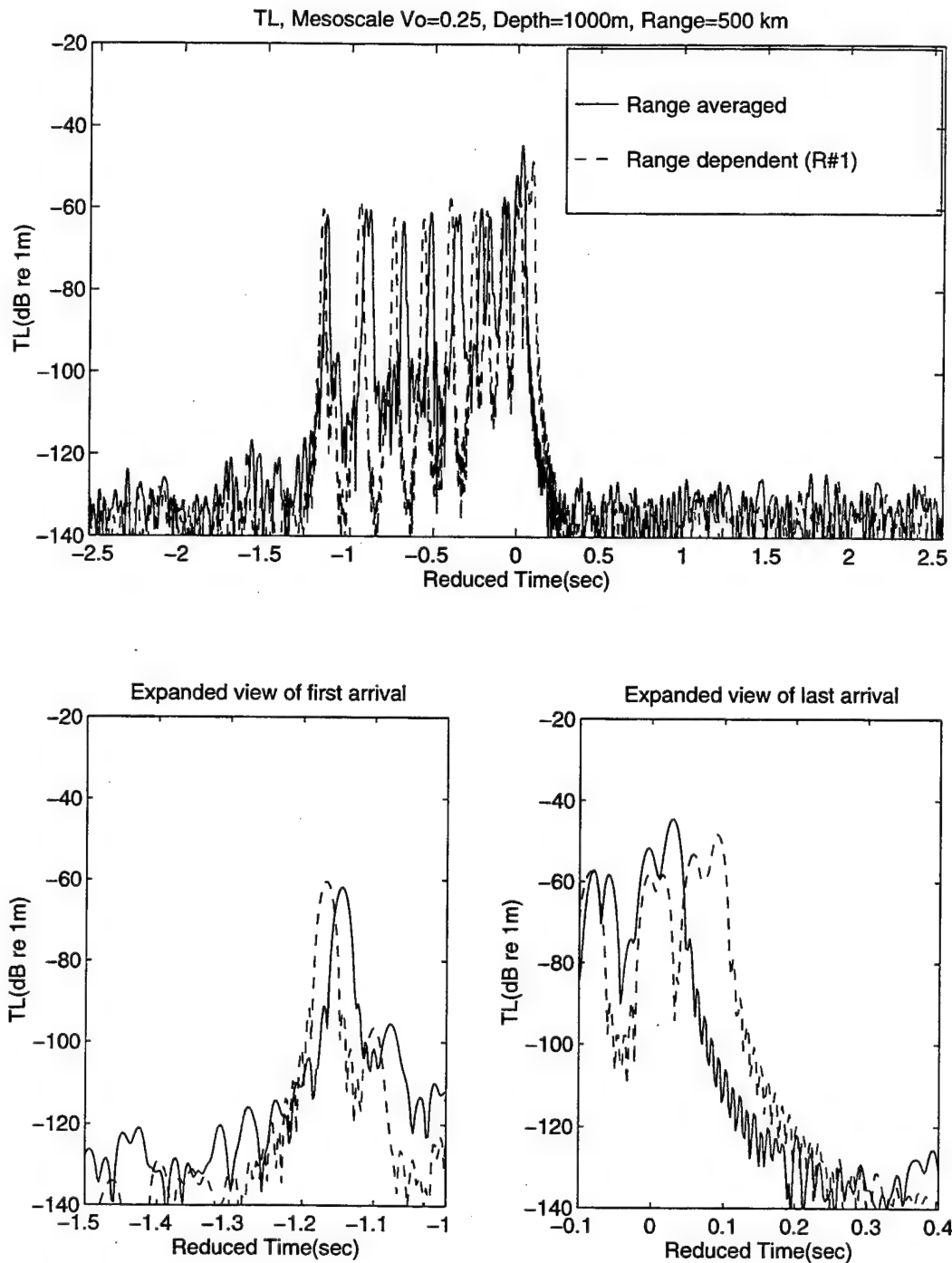


Figure 10. Transmission loss arrival time structures at range 500 km and depth 1000 m. Upper panel shows total structure for range-independent and range-dependent realization with $V_0=0.25$ m/s. Lower panels show expanded view of the first and last arrivals.

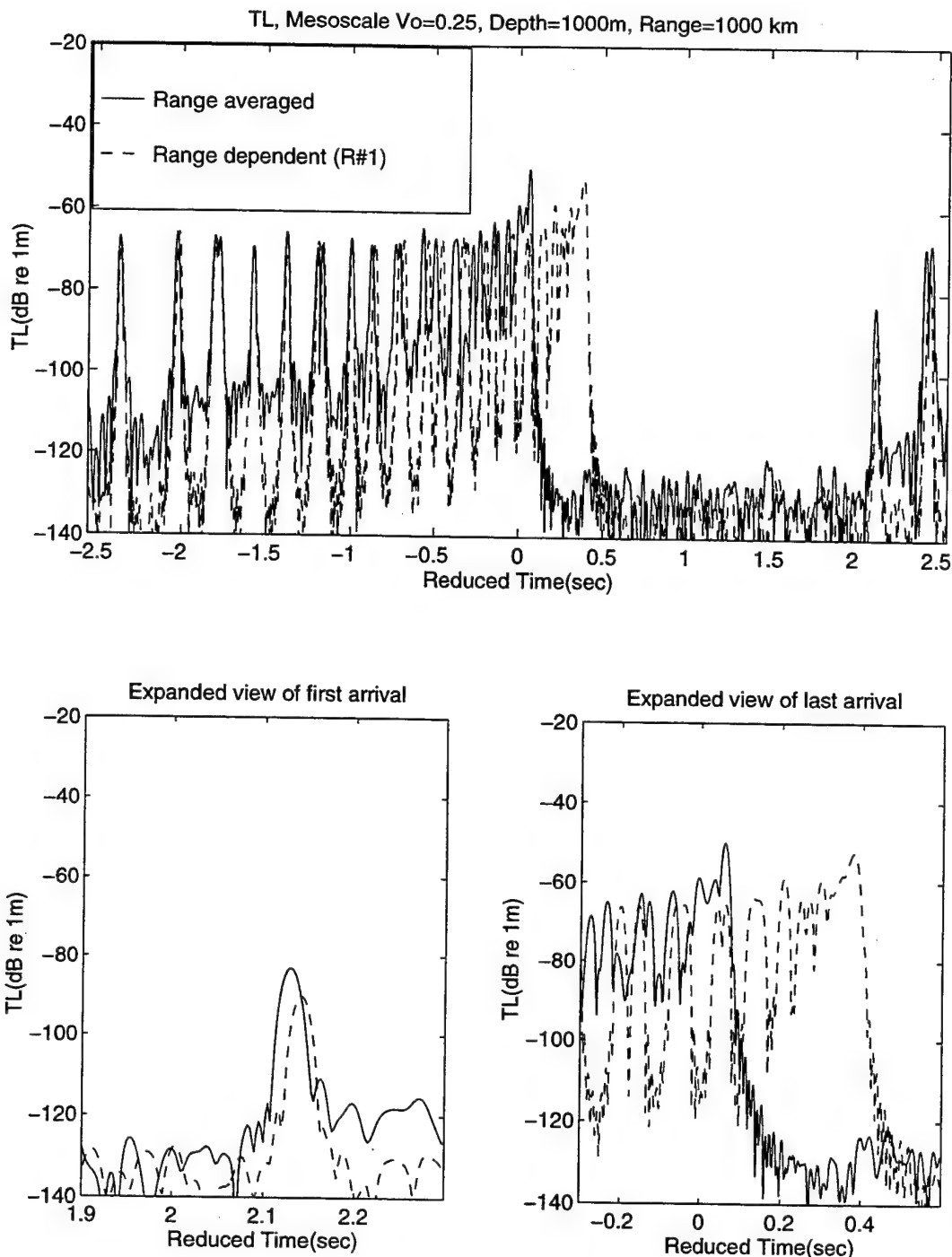


Figure 11. Transmission loss arrival time structures at range 1000 km and depth 1000 m. Upper panel shows total structure for range-independent and range-dependent realization with $V_0=0.25$ m/s. Lower panels show expanded view of the first and last arrivals.

accordingly. Histograms showing the respective number of realizations in each 10 msec time bin are provided by Figs. 12 and 13 for the 500 km and 1000 km ranges, respectively. Note that as the perturbation strength is increased, there is a significant spreading in the arrival envelope lengths. Additionally, the mean range-dependent arrival envelope length is longer than its corresponding mean range-averaged length for all four sets of data plotted.

The arrival envelope spread is computed by taking the difference between the range-dependent and associated range-averaged arrival envelope lengths. A positive spread indicates that the range-dependent envelope length is greater than its associated range-averaged counterpart. Again, histograms with 10 msec bins were constructed and are provided in Figs. 14 and 15 for the 500 km and 1000 km ranges, respectively. Note that while the mean for all four data is positive, there are several individual realizations with negative spreads. However, the arrival envelope spread becomes increasingly positive with increasing range and perturbation strength.

Next, the time difference between the range-dependent and associated range-averaged first peak arrivals was measured. This same time difference was also measured for the last peak arrivals. In this case, we refer to the time difference as the bias, where

$$\tau_{BIAS} = \tau_{RD} - \tau_{RA} . \quad (4.6)$$

In Eq. (4.6), the subscript *RD* denotes range-dependent and *RA* denotes range-averaged. Figures 16 and 17 provide histograms of the bias in the first and last peak arrivals at the 500 km and 1000 km ranges, respectively.

The mean bias for the near-axial (last) arrivals is generally positive, and increases with increasing perturbation strength and range. In particular, the mean bias for the last peak arrival increases by over 100 msec when the perturbation strength is increased from $V_0=0.125$ m/s to $V_0=0.25$ m/s. A possible physical explanation for this cold bias is that the acoustic path is continually adjusting toward the lowest sound speed, thus resulting in an actual sound speed along the path which is lower than the comparable range-average. The mean bias for the higher modes is significantly less indicating that these modes are more stable in terms of their arrival times. In some realizations, the earlier arrivals, those

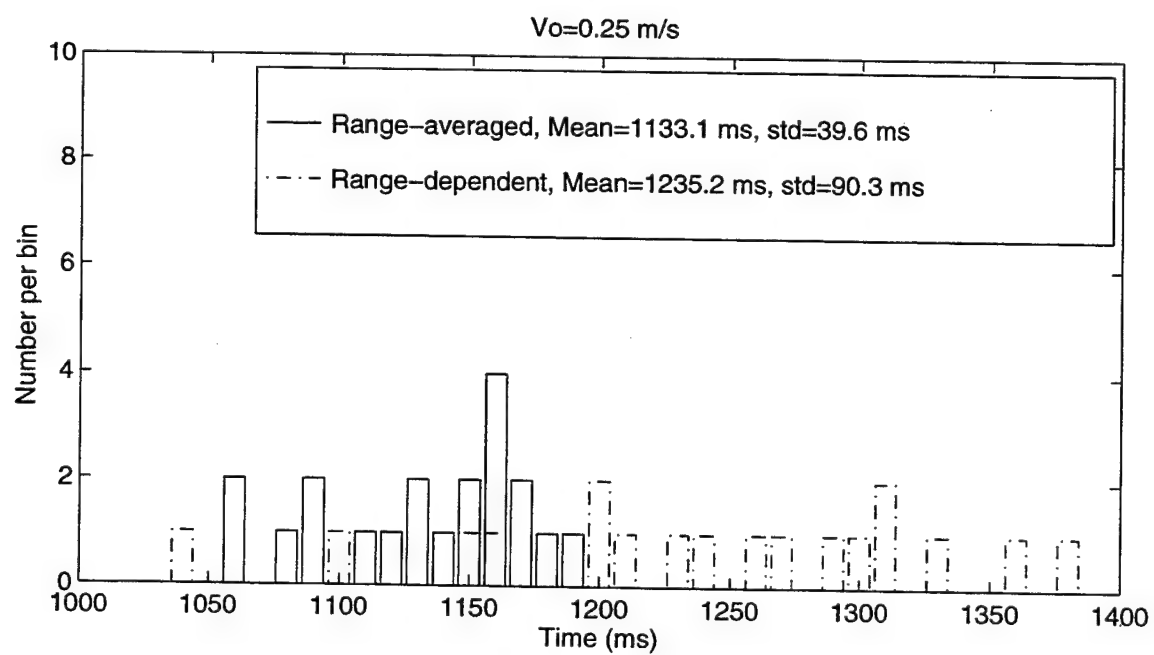
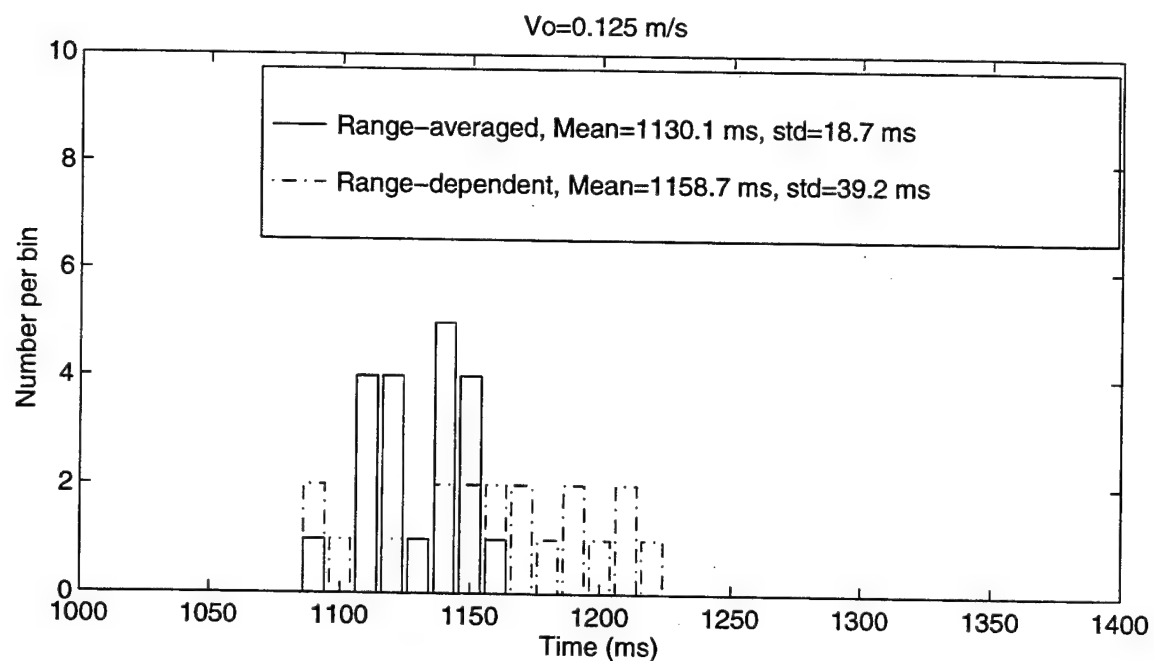


Figure 12. Arrival envelope lengths at 500 km range.

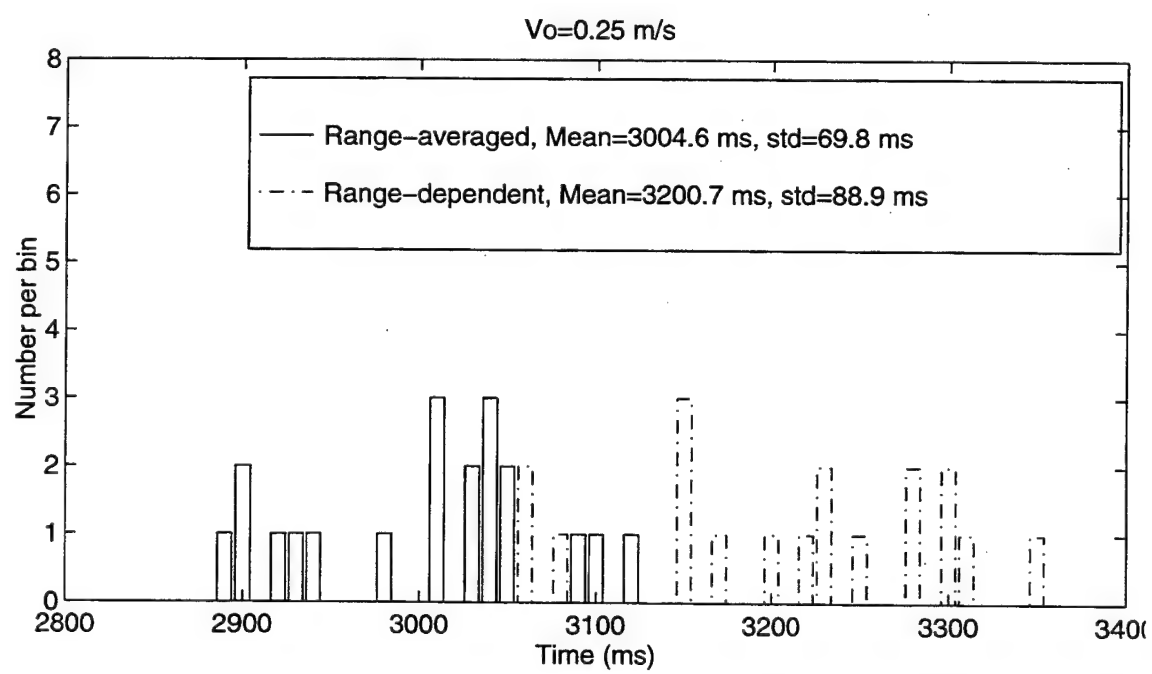
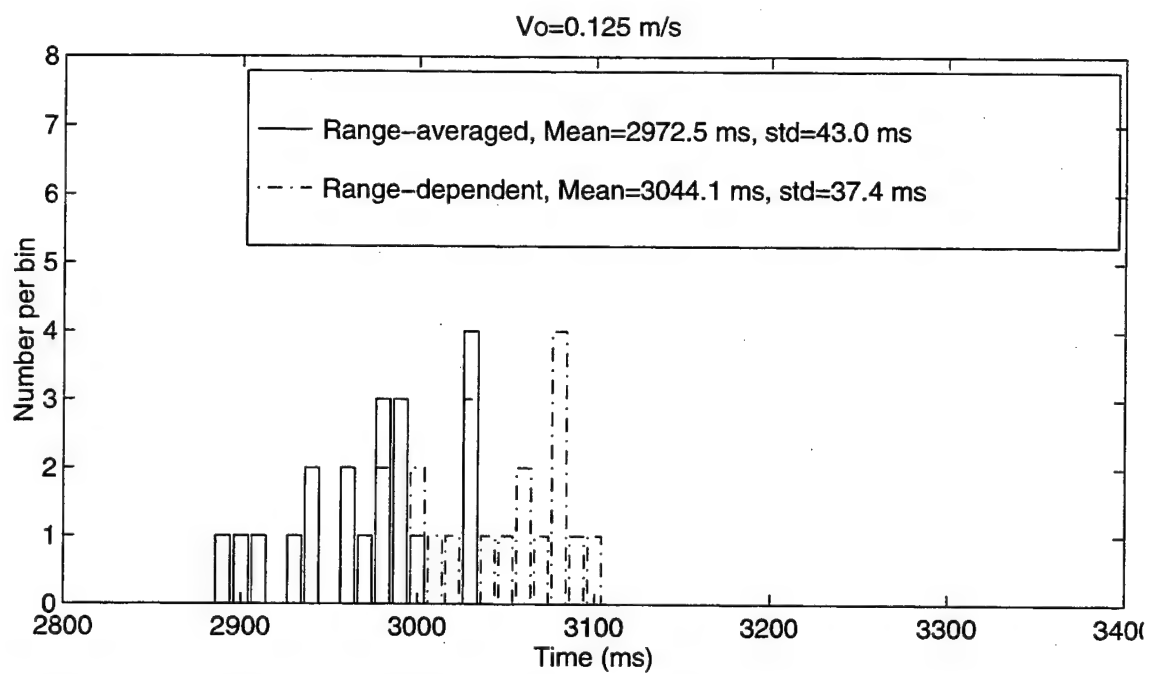


Figure 13. Arrival envelope lengths at 1000 km range.

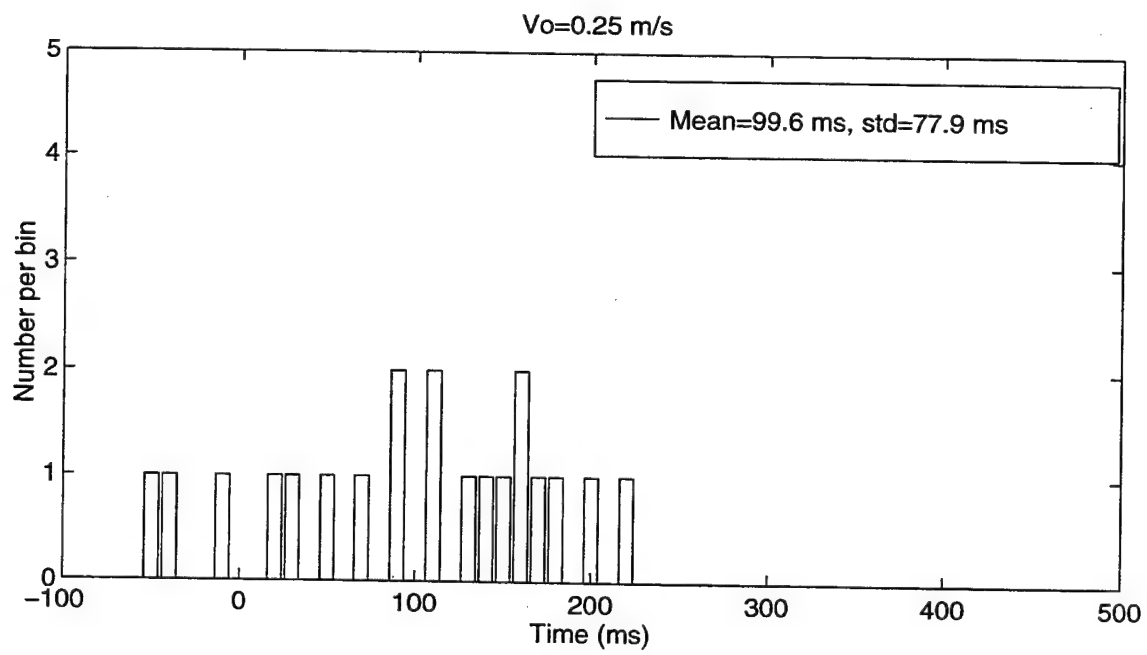
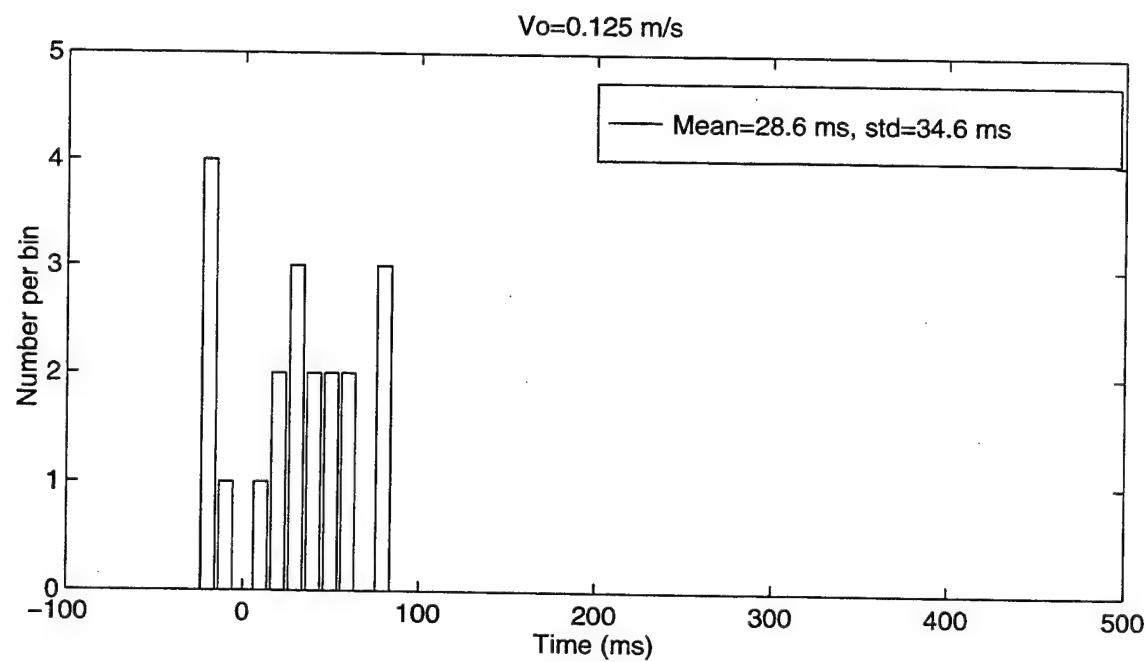


Figure 14. Arrival envelope spread at 500 km range.

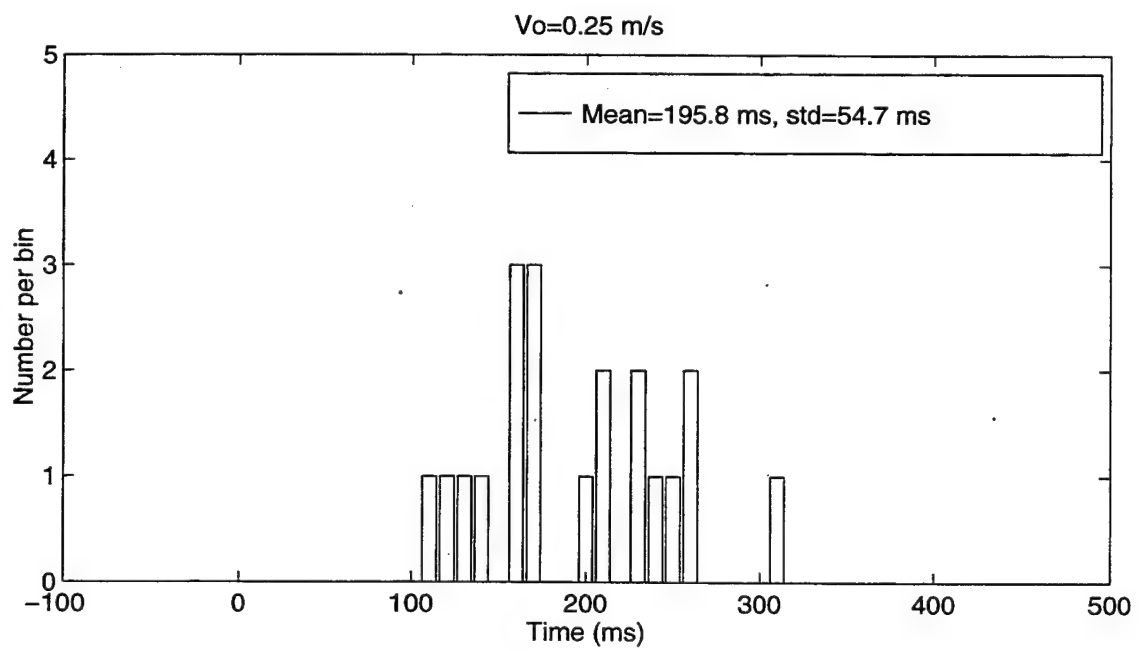
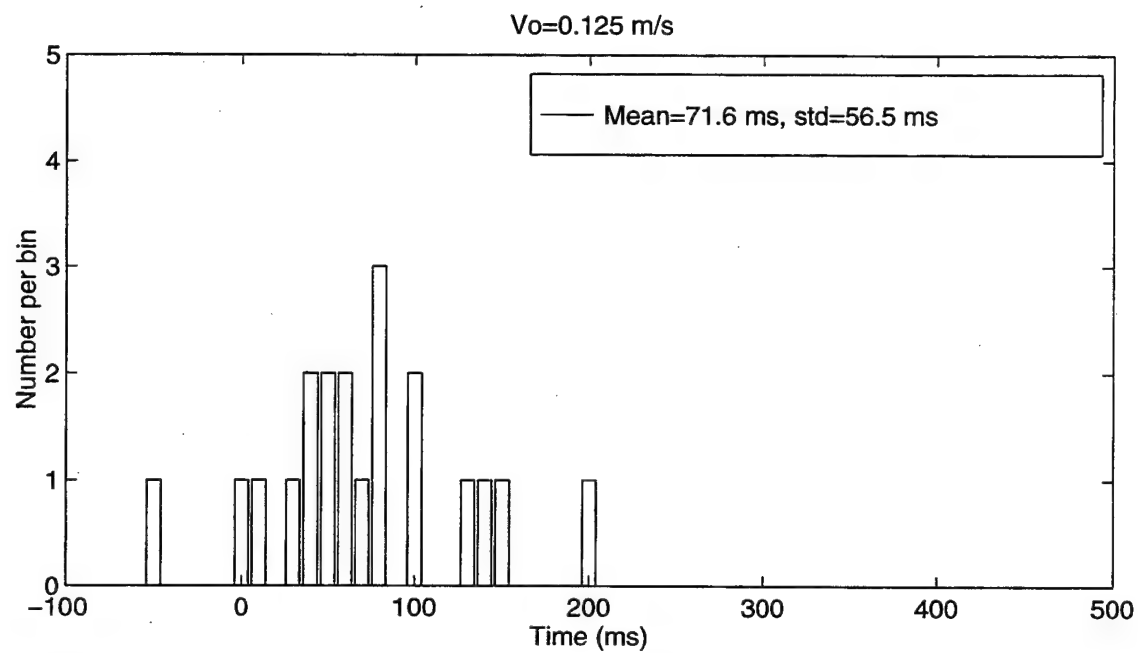


Figure 15. Arrival envelope spread at 1000 km range.

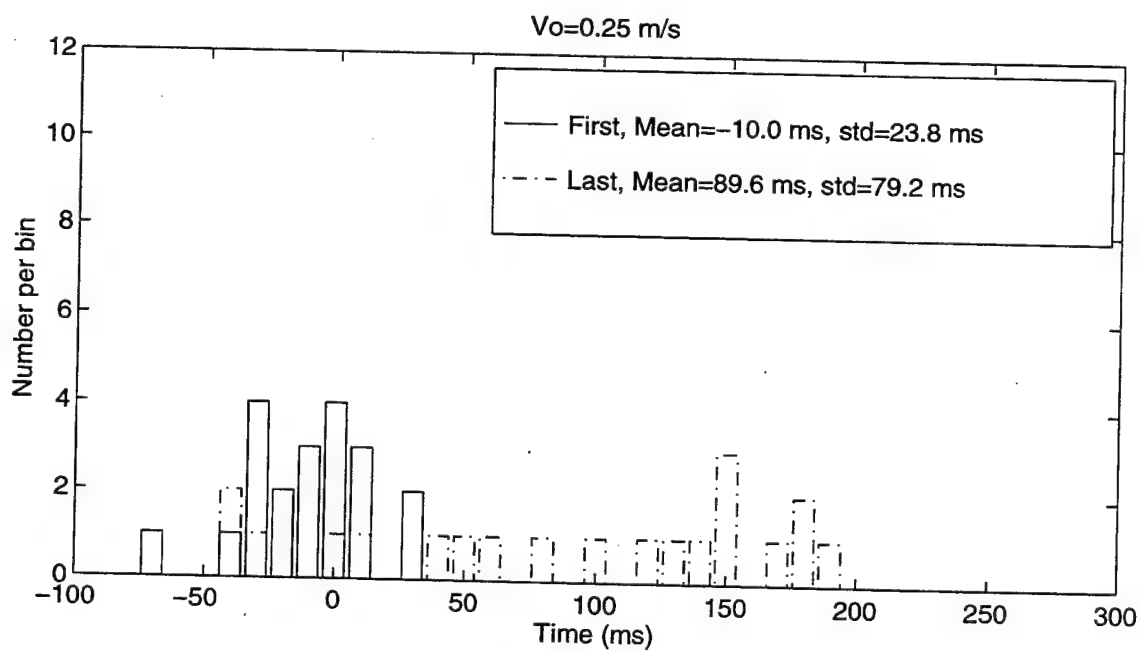
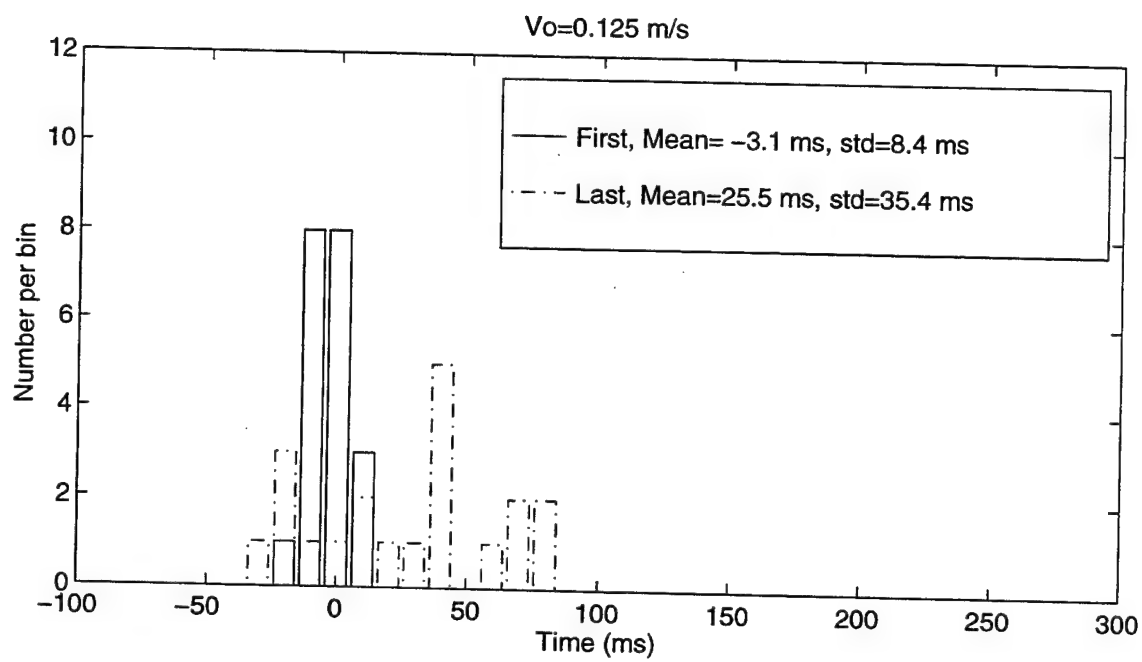


Figure 16. Travel time bias in first and last arrival peaks at 500 km range.

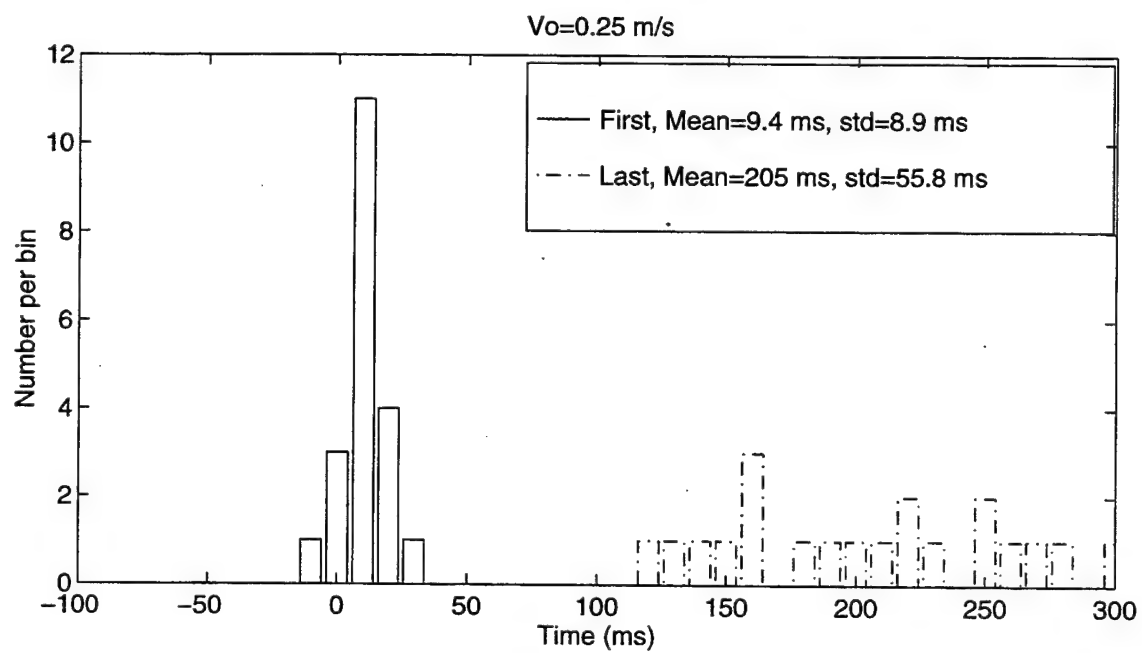
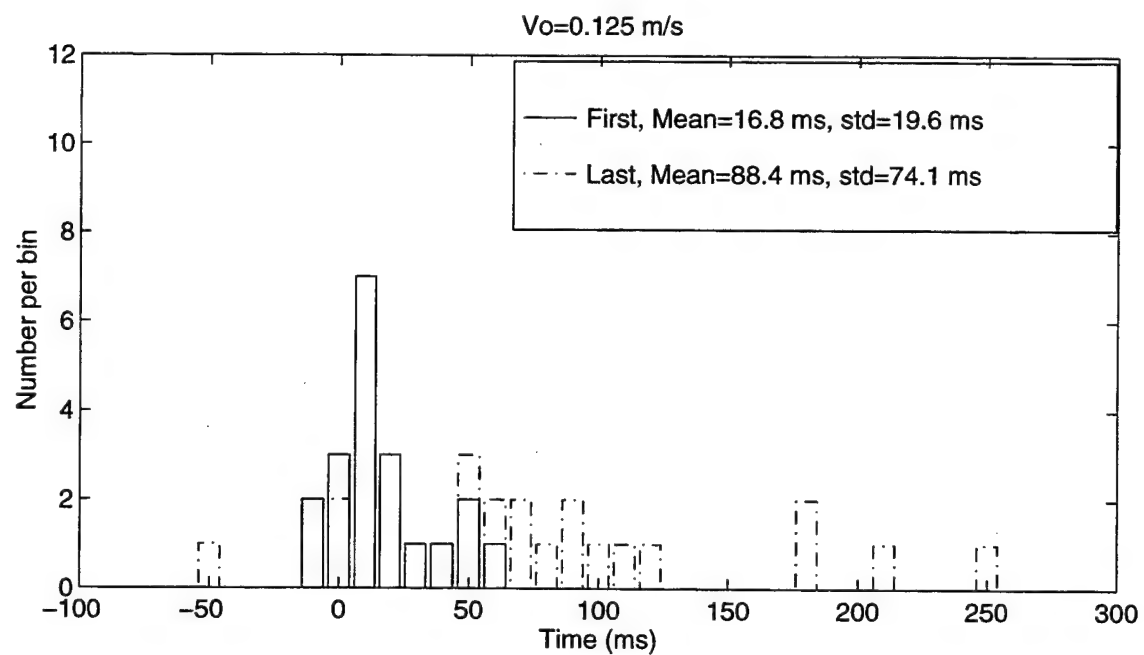


Figure 17. Travel time bias in first and last arrival peaks at 1000 km range.

corresponding to higher acoustic modes, actually arrive slightly earlier when the perturbations are present. The data may then suggest that the total time envelope of arrivals (i.e. time between earliest and last arrivals) always tends to increase. In all cases, however, the influence is most pronounced in the delayed arrival of the lowest modes.

In closing out this chapter, there are four main points which are suggested by the data.

- 1) Mesoscale features can significantly perturb the late arrivals (corresponding to the lowest order acoustic modes) and produce an overall spreading in the arrival structure even when propagation is adiabatic.
- 2) The bias in the arrival times of the lowest modes increases with increasing perturbation strength.
- 3) The size of bias variability is not directly related to range or perturbation strength.
- 4) Steeper, earlier arrivals are relatively stable in the presence of mesoscale structure.

The arrival data statistics are summarized by Table 4.

Strength	Range	Range=500 km		Range=1000 km	
		Mean	Std Dev	Mean	Std Dev
Vo= 0.125 m/s	First peak bias	-3.1 ms	8.4 ms	16.8 ms	19.6 ms
	Last peak bias	25.5 ms	35.4 ms	88.4 ms	74.1 ms
	Envelope Spread	28.6 ms	34.6 ms	71.6 ms	56.5 ms
Vo= 0.25 m/s	First peak bias	-10.0 ms	23.8 ms	9.4 ms	8.9 ms
	Last peak bias	89.6 ms	79.2 ms	205.0 ms	55.8 ms
	Envelope Spread	99.6 ms	77.9 ms	195.8 ms	54.7 ms

Table 4. Arrival statistics for deep ocean with random mesoscale structure.

V. TRAVEL TIME VARIABILITY DUE TO THE CALIFORNIA CURRENT FRONT

In this chapter, the effects of a fluctuating frontal region created by the California Current on modal acoustic travel time variability are investigated using a state-of-the-art global ocean circulation model to provide input environmental data. The California Current is the major eastern boundary current of the North Pacific. It is 500-1000 km wide and has been found to be highly variable in both space and time (Mooers and Robinson, 1984). The instantaneous current consists of intense meandering current filaments intermingled with synoptic-mesoscale eddies. In general, cool water upwelled near shore is entrained and then subsequently advected 100 km or more offshore by the variously oriented jetlike strong current filaments and eddies. Additionally, the jets and eddies can also advect warm offshore waters onshore to the coastal ocean. Through satellite imagery and oceanographic studies, it has been shown that this jet and eddy system can change substantially on a weekly time scale.

Recently there has been work along a similar theme (Dushaw, 1997) which was motivated by the ATOC project. Dushaw's concern was that, as described previously, variability in the acoustic pulse travel time acts as geophysical "noise" in problems such as accurately assessing the large-scale North Pacific heat budget. An accurate assessment may be extremely difficult for acoustic paths passing through this region if the effect of variability in the California Current is severe enough. Dushaw examined the effects of the California Current on synthetic acoustic transmissions made from the ATOC Pioneer Seamount acoustic source (shown on Fig. 18) to a fictional receiver 500 km away along a path which is nearly perpendicular to the California coast. He calculated the variation of ray travel times using environmental input data interpolated from the California Cooperative Fisheries Investigations (CalCOFI) time series data. However, there are shortfalls in using the CalCOFI data which are pointed out by Dushaw. In particular, the CalCOFI data sampling is irregular in time, depth, and horizontal sampling. At best, temporal sampling is provided at some of the CalCOFI grid stations on a monthly basis, but the

entire grid is rarely surveyed during any particular month or year. The sporadic monthly sampling does not capture the complete variability known to exist in this region from satellite imagery. Furthermore, vertical sampling is limited to the upper 500 to 1000 m of the water column, dependent on the observation year. Accordingly, Dushaw relied on a limited number of sound speed profiles and extensive interpolation to generate his range-dependent sound speed environment, and as discussed in his results, his study could not address any sound speed variability which may occur below 1000 m. Given these limitations, and after accounting for the assumed general North Pacific variability, his conclusion was that a conservative upper bound on ray travel time variability specifically due to California Current variability is ± 50 ms for the 1000-5000 km ATOC transmissions.

In an effort to capture more completely the variability of the California Current System and acoustic transmissions through a small region of it, this investigation uses the global Parallel Ocean Circulation Model (POCM) (Semtner and Chervin, 1992), also known as the Semtner and Chervin model, to obtain realistic environmental input data spanning a one-year time period over a 474 km acoustic path. In that this was a first-time use of POCM with the UMPE acoustic propagation model, it was necessary to develop computer code to interface the two models. Then, using the coupled ocean-acoustic model, the temporal, spatial and seasonal variability in the individual modal arrivals of the first thirty modes is assessed. The mesoscale bias variability is also examined by comparing the full-field peak arrival times for the range-averaged environment to that of the range-dependent environment at the 400 km and receiver ranges.

The research here is presented in a number of sections. First the ocean model used for environmental data input is described. Next the method of reformatting the input environmental data into a usable format for UMPE and description of a typical sound speed field are provided. This is followed by a discussion of the acoustic modeling method and modal variability analysis. Finally, a discussion of results with general conclusions is presented.

A. OCEAN MODEL

Input environmental data is obtained from the global Parallel Ocean Circulation Model (POCM), also known as the Semtner and Chervin model. Semtner and Chervin (1992) describe the basic POCM model formulation, and Stammer *et. al.* (1996) describe subsequent improvements to the POCM model. It was this improved model that was used for obtaining input environmental data for the coupled ocean-acoustic modeling described herein. Key features of the improved model are described below.

The POCM model is capable of resolving mesoscale ocean features and strong currents both spatially and temporally. Initially, a 1/2-degree model initialized with Levitus temperature and salinity data was spun up for 33 years. Instantaneous fields were then interpolated to a Mercator grid size of 0.4 degree in longitude, thus producing square grids between the equator and 75 degrees latitude. This provides a nominal lateral resolution of 1/4 degree (~25 km). The simulation was then resumed, starting with the recorded winds of January 1985 providing the forcing function. Up to 20 vertical layers are provided at each grid point. In that the greatest variability is observed near the ocean surface, the spacing between vertical layers is approximately 25 m near the surface and then the layer spacing gradually increases with ocean depth. Coastlines and bathymetry are prescribed at the local model resolution, and are not smoothed further.

Model data is available for numerous years, at a time interval of three days. With realistic external surface boundary forcing, including daily wind-stress fields and sea surface heat fluxes, the POCM simulated ocean environment successfully models the large scale variability as compared with oceanographic observations. However, the simulated amplitudes of variability are reported to be low by about a factor of 2 to 4 over a broad spectral range. This discrepancy in energy is greatest at high frequencies and wavenumbers, diminishing to a factor of two at the lowest frequencies and wavenumbers (Stammer *et al.*, 1996).

B. ACOUSTIC PATH DESCRIPTION AND INPUT DATA PREPARATION

For this particular investigation, the chosen acoustic path is between a moored SOFAR source designated SS3 and a SOSUS hydrophone array at Point Sur, California for an approximate path length of 474.6 km. The source and receiver locations are shown in Fig. 18. The Naval Postgraduate School (NPS) sound sources designated SS1, SS2, SS3 in this figure were specifically deployed to study the California Current System by tracking oceanographic floats (Garfield *et. al.*, 1997). The source provides a linear frequency modulated chirp with a center frequency of 260.1 Hz and a swept bandwidth of 1.523 Hz, has a source level of 183 dB re 1 μ Pa, and is moored at 642 m depth. Source signal monitoring is done with the Pt. Sur SOSUS hydrophone array (C.-S. Chiu, pers.

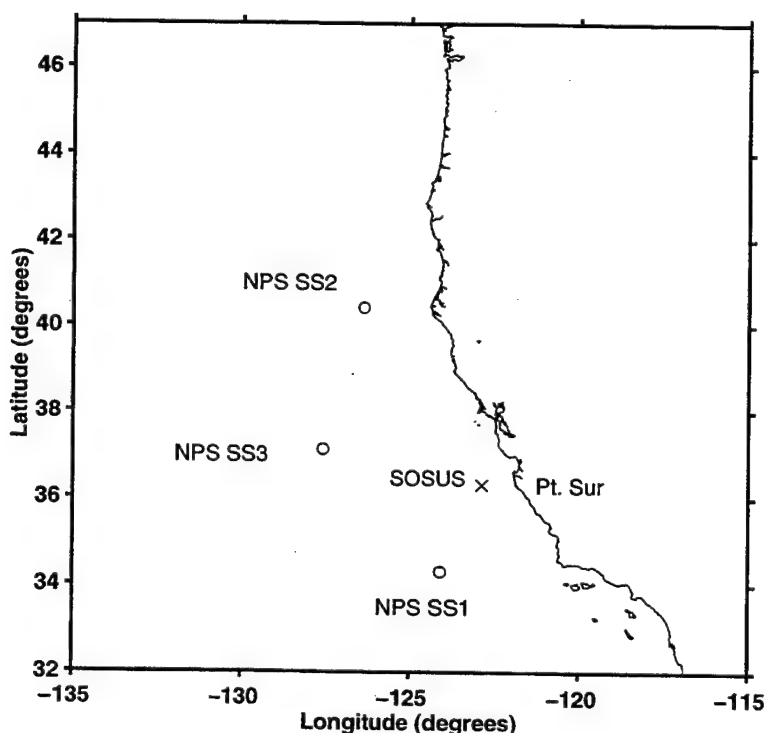


Figure 18. West coast sound sources. NPS sound sources designated SS1, SS2, SS3 were specifically deployed to study the California Current System by tracking oceanographic floats. SOSUS array is located near Pt. Sur.

comm., 1997). The Point Sur array is at the ocean bottom, a depth of 1359 meters. Actual data is available from this source/receiver combination for future comparison with numerical predictions obtained using POCM environmental input data. Available source and receiver characteristics are summarized in Tables 5 and 6, respectively.

To assess the acoustic stability of arrivals for this source/receiver combination, the first step was to obtain data sets of temperature and salinity spanning a one-year time period (122 data sets, model year 1995) from the POCM model. Bathymetry data was obtained from the National Oceanographic Data Center (NODC) database DBDB5 which

Parameter	Value
Mooring location	37° 06.55'N 127° 34.60'W
Source depth	642 m
Water depth	4752 m
Center frequency	260.1 Hz
Signal	LFM Chirp
Swept Bandwidth	1.523 Hz
Pulse length	0.6 sec
Source Level	183 dB re 1 μ Pa

Table 5. Naval Postgraduate School SS3 source characteristics

Parameter	Value
Location	36° 17.87'N 122° 22.58'W
Type	Single hydrophone
Receiver depth	1359 m
Bottom depth	1359 m
Distance from SS3 source	476.1 km

Table 6. Pt. Sur receiver characteristics

has a resolution of $0^\circ 05'$. The next step was to interpolate the temperature, salinity, and bathymetry data from the ocean model/database grid points onto grid points along a 2-D great circle path between the chosen source-receiver combination. Horizontal interpolations were done linearly, whereas interpolations between vertical depth layers were done using a cubic spline. The interpolated temperature and salinity data was then converted into sound speed using the empirical formula (Mackenzie, 1981)

$$c(z, S, t) = 1449.2 + 46t - 5.5t^2 + 0.29t^3 + (1.34 - 0.1t)(S - 35) + 0.016z \quad (5.1)$$

where c is sound speed in m/s, S is the salinity in parts per thousand (ppt), z the depth in meters, and $t = T/10$ where T is in degrees Celsius.

A typical sound speed profile interpolated from the POCM output consists of a surface duct with its local sound speed minimum around 200 m depth and a main water column channel with an axial depth around 1000 m. To illustrate the annual sound speed variability along the chosen acoustic path, the yearly mean range-averaged sound speed profile and its envelope are provided in Fig. 19. This figure also plots the full ensemble of range-averaged sound-speed profiles. Note that the POCM output suggests that the surface duct persists throughout the annual cycle. This is not considered realistic (C.-S. Chiu, pers. comm., 1997). Subsequently, this chapter will focus on modal travel time variability for modes which remain in the main water column channel.

The sound speed perturbation fields for POCM model dates 05 Jan 95 and 01 Jul 95 are depicted by Figs. 20 and 21, respectively, where the sound speed perturbation is defined as

$$\delta c(r, z) = c(r, z) - c_{RA}(z) \quad (5.2)$$

and $c_{RA}(z)$ is the reference range-averaged sound speed profile specific to that data set. For the January perturbation field, the sound speed perturbations range from about ± 3.5 m/s and are essentially limited to the upper 2000 meters in the water column. The July perturbation field shows much stronger gradients, with amplitudes ranging from about ± 6.0 m/s and extending deeper to near 2500 meters depth. Throughout the year, the

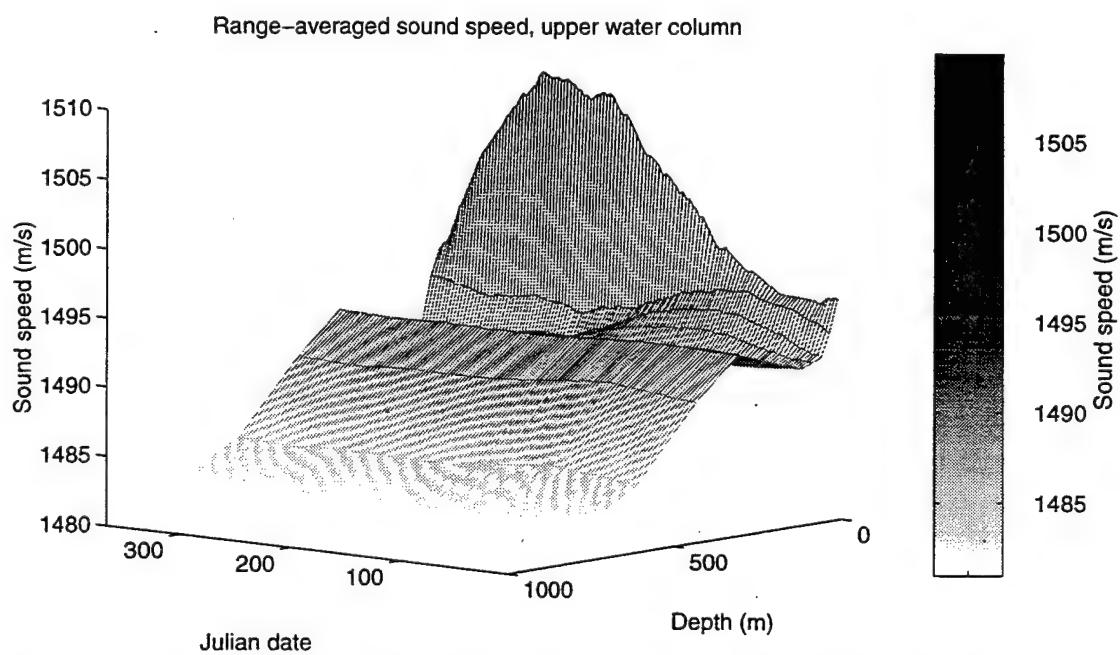
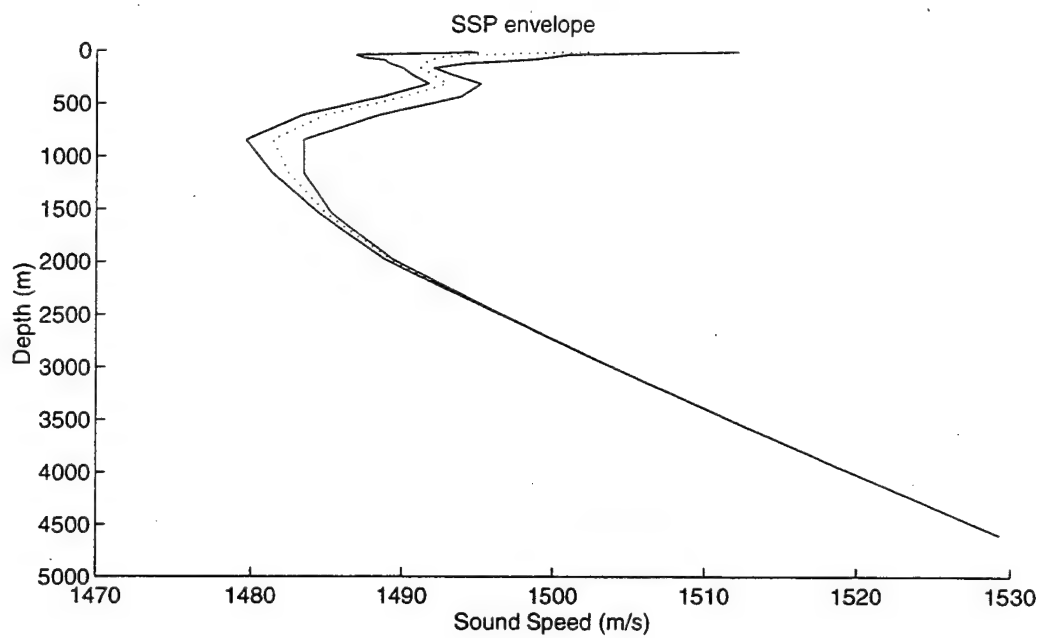


Figure 19. Annual range-averaged sound speed profiles as interpolated from POCM output for modeled environment. Upper panel shows the mean annual range-averaged sound speed profile and envelope of range-averaged sound speed profiles. Lower panel illustrates the variation in range-averaged sound speed profiles over the annual cycle.

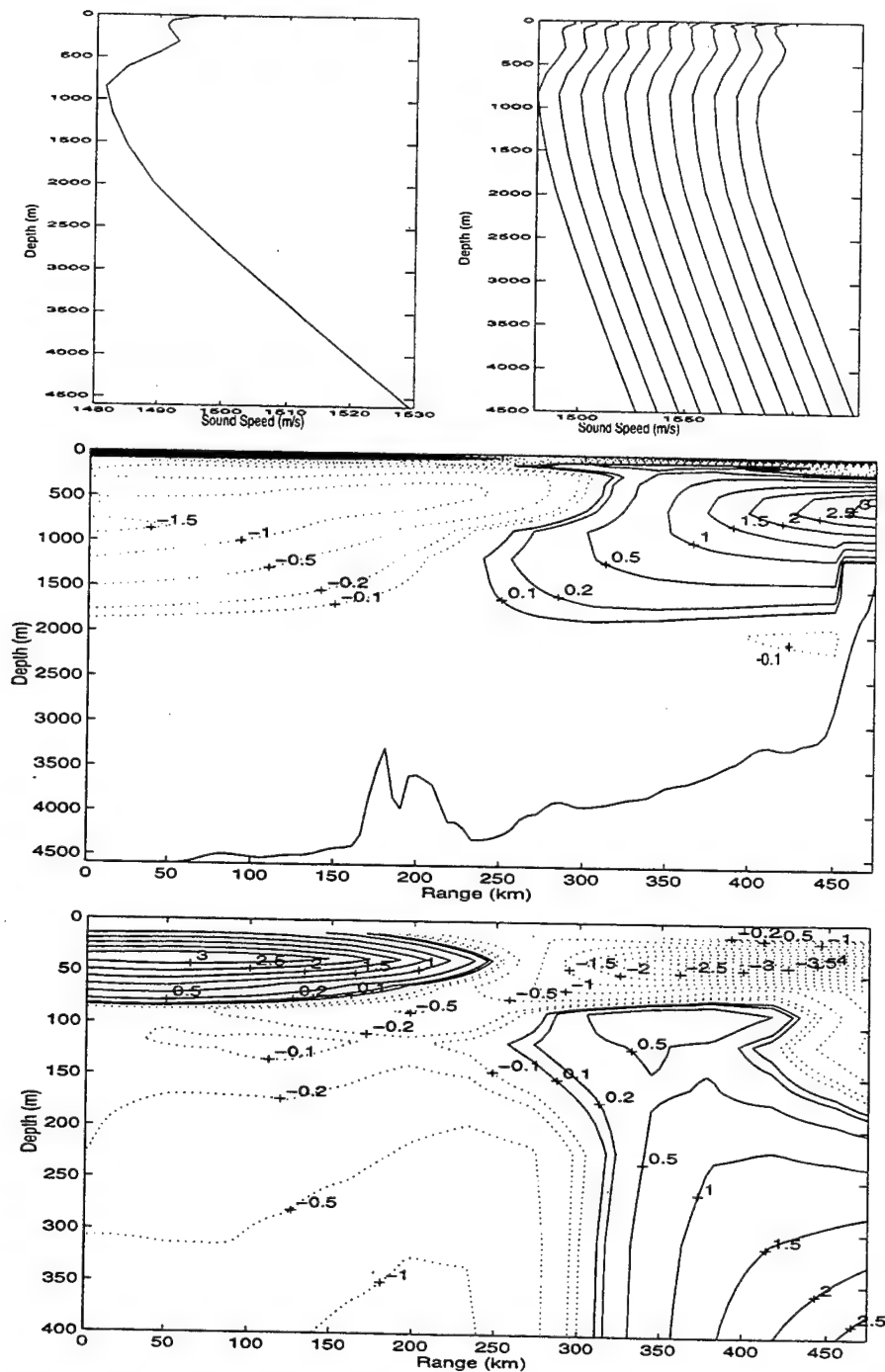


Figure 20. Sound speed perturbation field for POCM model date 05 Jan 95. Top left panel shows reference range-averaged sound speed profile. Top right panel shows 11 equally-spaced sound-speed profiles as a function of range. Abscissa scale applies only to first profile. Middle panel shows perturbation field for entire water column and bathymetry along track. Lower panel provides enlarged view of field in the upper 400 m.

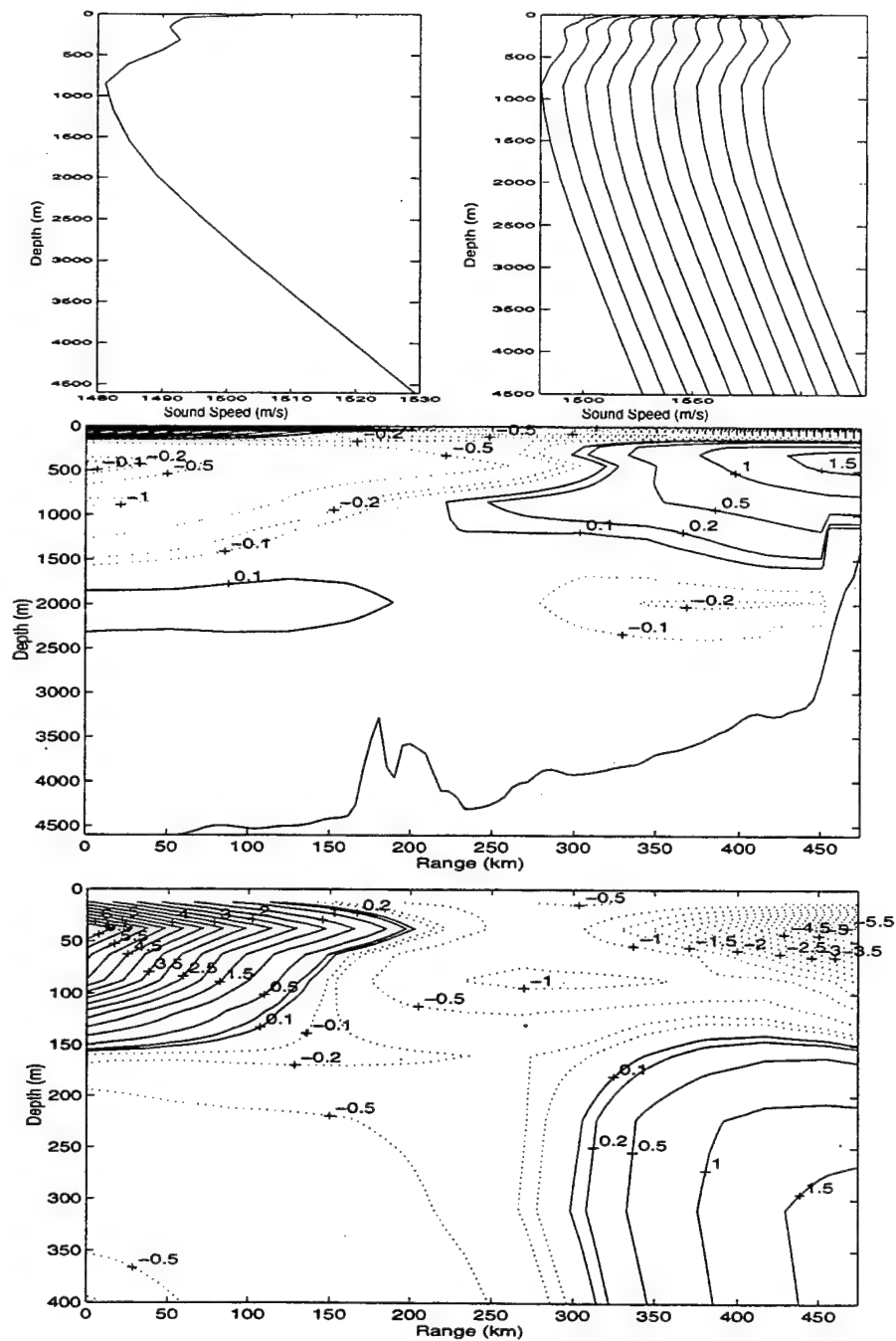


Figure 21. Sound speed perturbation field for POCM model date 01 Jul 95. Top left panel shows reference range-averaged sound speed profile. Top right panel shows 11 equally-spaced sound-speed profiles as a function of range. Abscissa scale applies only to first profile. Middle panel shows perturbation field for entire water column and bathymetry along track. Lower panel provides enlarged view of field in the upper 400 m.

surface duct is seen to be much more pronounced in the region near the receiver relative to that near the sound source.

C. ACOUSTIC MODELING

The range-dependent sound speed environments computed using the 122 POCM datasets are individually input into the UMPE acoustic propagation model to compute the full acoustic pressure field and the arrival structures at specific ranges of interest. In addition, UMPE runs using a range-averaged sound speed profile as environmental input were completed for 25 data sets (every 15 model days) to support analysis of the mesoscale bias variability. Range-averaged sound speed profiles were computed for each data set by averaging the range-dependent sound speed profiles (water column sound speeds only) at 1 km steps up to the range of interest. Input parameters for the UMPE acoustic propagation modeling are summarized in Table 7. Typical range-dependent arrival structures across the full water column at the receiver range and two intermediary ranges are presented in Fig. 22. Figure 23 displays a typical full-field arrival structure in terms of transmission loss specifically at the receiver depth and range. The variability in these full-field arrival structures at the receiver depth and range are demonstrated by Figs. 24 and 25.

To determine the degree of mode coupling as a function of environmental parameters and bathymetry, pressure field modal decompositions were completed for range-averaged and range-dependent environments, with and without bathymetry. The standard PE approximation was used to compute the pressure field used for these modal decompositions, so that KRAKEN standard normal modes might be employed as the proper basis set. Typical results are plotted in Fig. 26. For the modes analyzed, this figure clearly illustrates that bathymetry plays no role in mode coupling until approximately the last 20 km where the ocean bottom shows a relatively steep rise to depths of less than 3000 m as it nears the Pt. Sur coastline. Environmental parameters which influence sound speed appear to have the greatest impact on mode coupling in the 200-300 km range

Parameter	Value
Type of PE approximation	Wide-angle
Reference sound speed, c_0	1495.2 m/s
Number of points in depth	8192
Computational depth	6500.0 m
Depth mesh size	1.6 m
Range step size	5.0 m
Maximum range	474.61 km
Center frequency	260.1 Hz
Number of frequencies	64
Frequency bandwidth	1.6 Hz
Frequency bin spacing	0.025 Hz
Source depth	642.0 m
Source level	183 dB re 1 μ Pa
Source spectrum	Hanning amplitude window
Angle of the beam center	0.00 deg
RMS half-width angle	35.00 deg
Taper	10.00 deg

Table 7. Acoustic propagation model (UMPE) input run parameters for west coast environment.

segment, and again between 450 and 474 km range. In this latter range segment, surface ducting and bathymetry effects become important to the specific modes being analyzed. As will be shown in the next section, some of the local normal modes shift from a "deep water" mode at ranges of 200 and 400 km to surface duct modes at the receiver range. Due to concerns regarding the validity of surface layer sound speeds as interpolated from

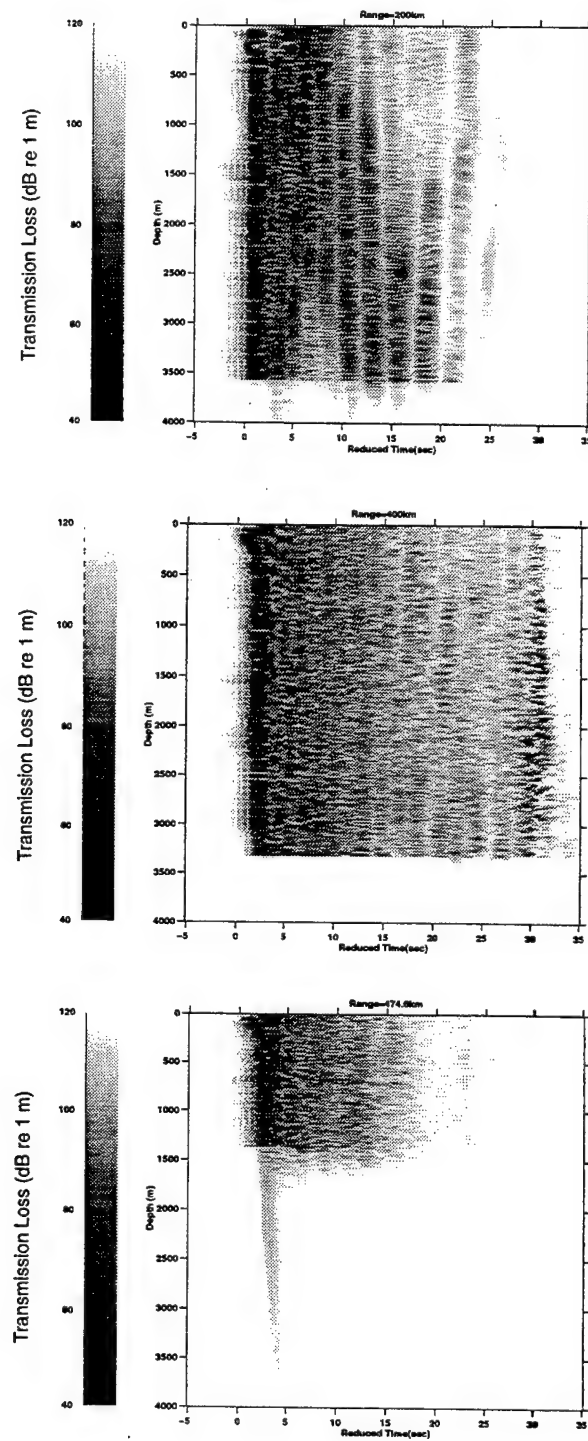


Figure 22. Typical range-dependent arrival structures at 200, 400, and 474 km ranges. Reduced time is referenced to 133.761, 267.523, and 317.081 seconds, respectively.

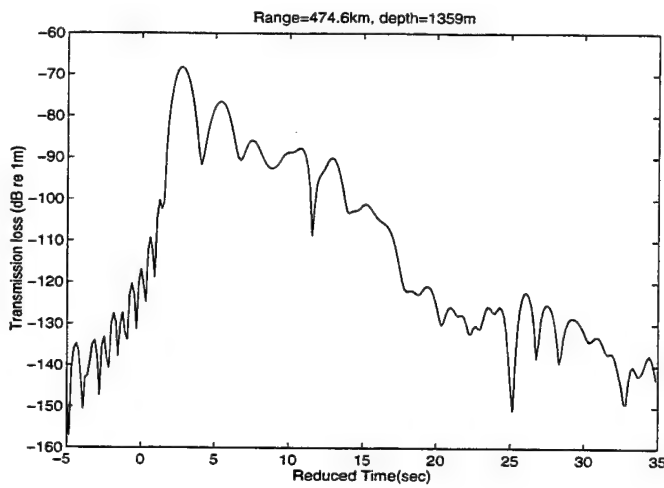


Figure 23. Plot of typical arrival structure at receiver depth (model date 31Jul95).

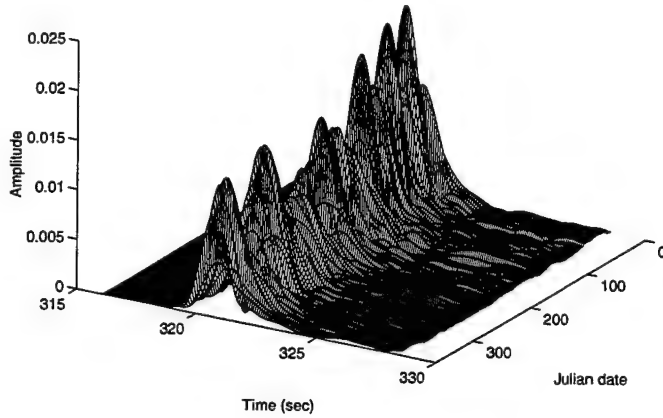


Figure 24. Full pressure field arrival structure at receiver over one model year period.

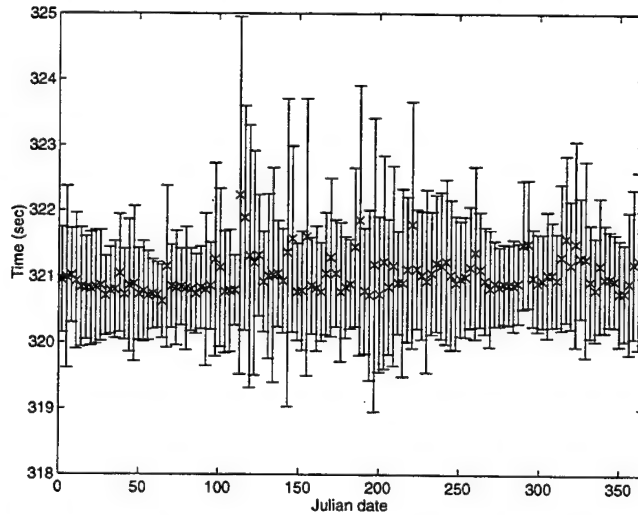


Figure 25. Centroid and energy distribution of arrival structure at receiver over one year.

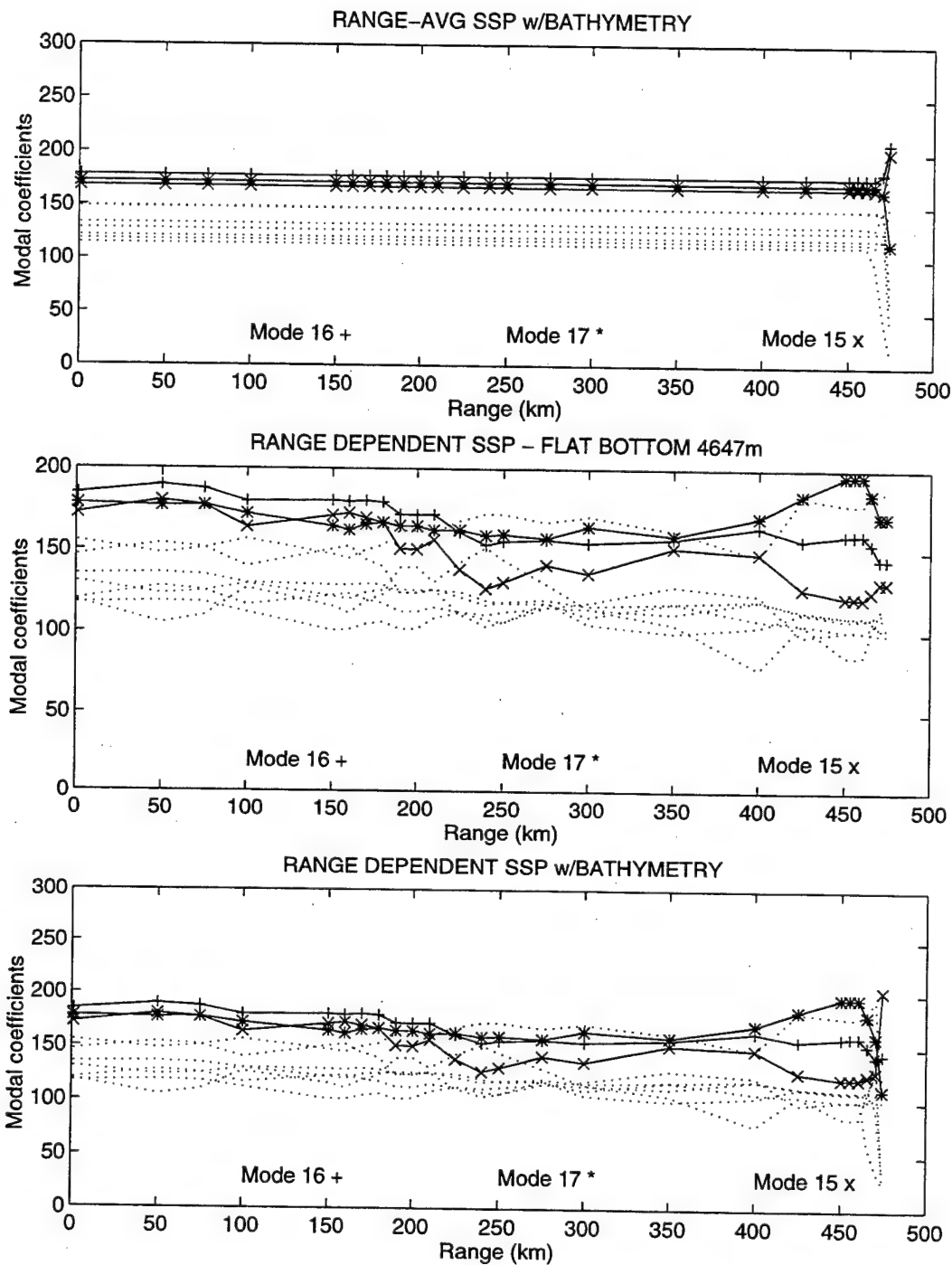


Figure 26. Modal coefficient amplitudes for a single frequency run. Upper panel is for the range-averaged sound speed profile with bathymetry. Middle panel assumes flat bottom with range-dependent sound speed profile. Lower panel incorporates both the range dependent sound speed profile and bottom bathymetry.

POCM output, modal travel time variability was assessed only at the 400 km range where the first thirty modes remained in the main water column channel.

D. MODAL ANALYSIS

In this section the spatial and temporal variability of the first thirty local modes is assessed. In addition, the mesoscale bias variability is examined by comparing the full-field peak arrival times for the range-dependent environment to that of the corresponding range-averaged environment. To examine the modal variability, the WAPE pressure field at selected ranges was decomposed into local normal modes using the numerical code KRAKEN (Porter, 1995). As discussed in Chapt. III, there is a slight, but acceptable, error introduced to the modal travel time by using standard normal modes for decomposing the WAPE field. Using inverse Fourier techniques described in Chapt. II, the individual modal arrival times were computed at the 400 km range. Note that due to mode coupling, there is a complex relationship between modal travel time variability and sound speed perturbation.

The spatial variability in selected local mode functions at the 200 km, 400 km, and receiver ranges are depicted by waterfall displays in Figs. 27, 28, and 29, respectively. At the 200 and 400 km ranges, modes 1-30 reside entirely in the main water column channel, with upper and lower turning points confined between 400 m and 1950 m depths. At the 200 km range, the mode shapes show very little variability over the annual cycle. At the 400 km range, there is a slight but detectable upward shift in the upper and lower turning points during the summer season. The greatest spatial variability in the mode functions occurs at the receiver range. At this range, modes 23-30 alternately appear as surface duct (modes 1 and 2) and water column channel modes dependent on the specific sound speed environment and frequency. For simplicity in further discussion, these modes will be referred to simply as "surface duct" modes. The axis of the surface duct clearly shifts over time, as is evident in the mode 30 plot. Again, the modal upper turning points generally tend to shift upwards during the summer season. In addition, it is noted

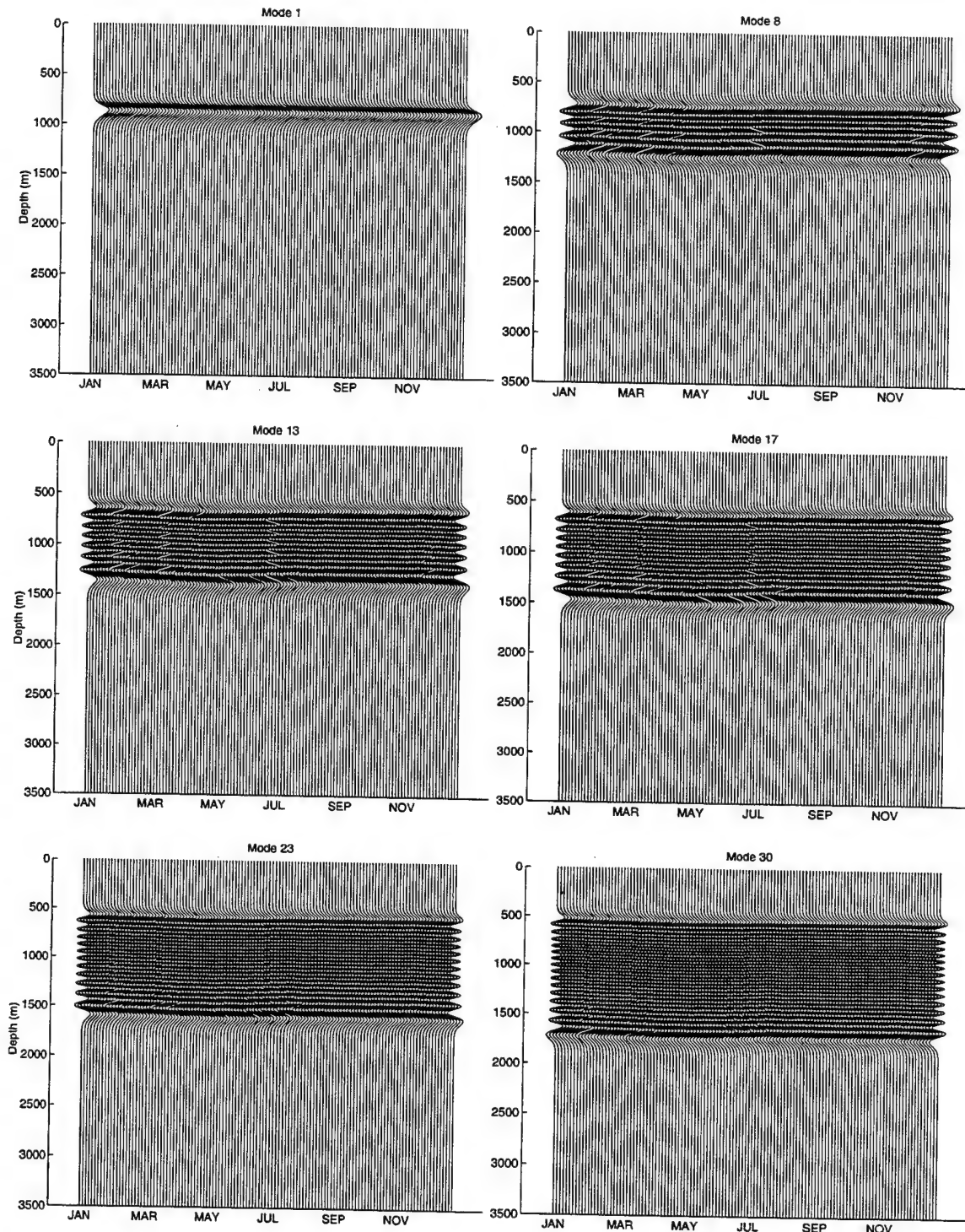


Figure 27. Annual spatial variability of selected mode functions at 200 km range.

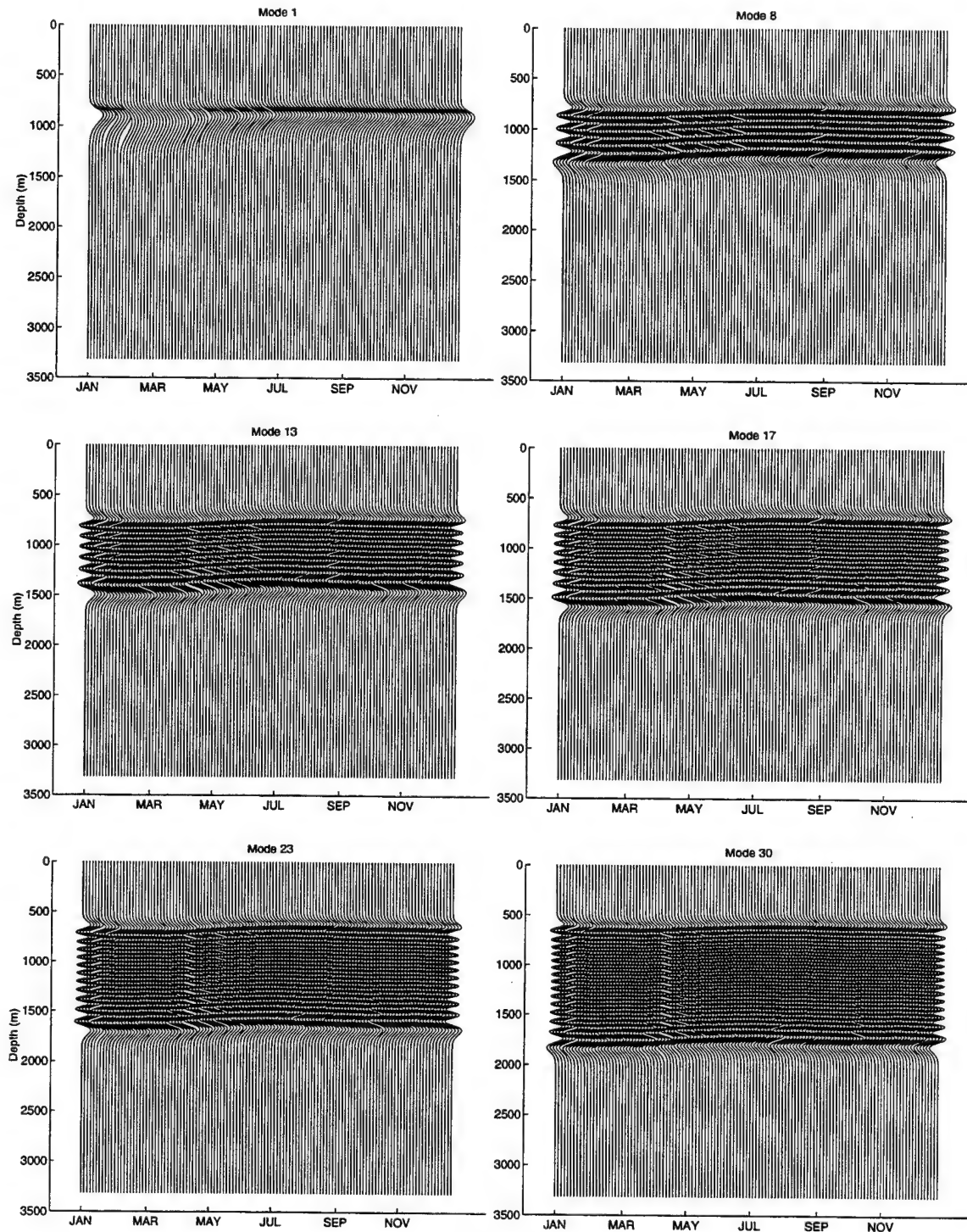


Figure 28. Annual spatial variability of selected mode functions at 400 km range.

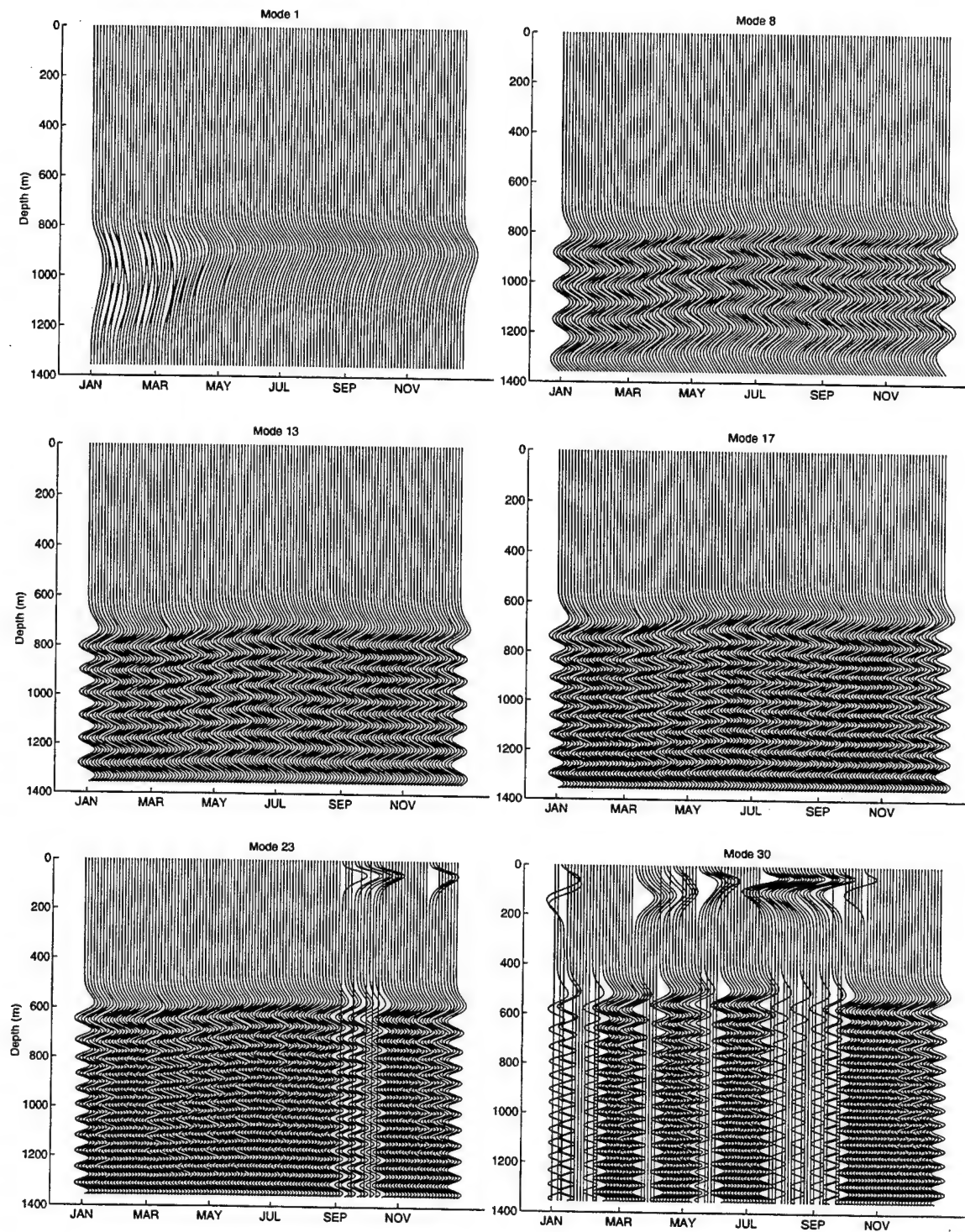


Figure 29. Annual spatial variability of selected mode functions at receiver range. For modes 23 and above, mode numbers refer to deep channel mode number (rather than surface duct mode number).

that modes 8 and higher are bottom interacting at the receiver range.

To assess the temporal variability for each of the first 30 modes, the following statistics were computed at the 400 km range:

- 1) ensemble (annual) mean for the energy centroid arrival time, and the corresponding ensemble mean energy distribution (arrival width),
- 2) variance in the ensemble mean centroid arrival time, and
- 3) variance in the ensemble mean energy distribution,

where the ensemble consisted of the 122 range-dependent data sets. Results are presented graphically for selected modes in Figs. 30 and 31, and numerically for the first thirty modes in Table 8. These statistics show that arrival time (centroid) variability is limited to ± 52 msec. Modes 12 through 18 are the most stable, with their variability limited to ± 17 msec. The mean energy distribution (spread in modal peak arrival) also shows little variability, in general less than ± 6 msec, over the annual cycle for these lower water column modes with the exception of modes 1, 2, 3, and 30 which vary up to ± 276 msec. However, it is also noted that for many of the computations, modal amplitudes for modes 1 and 2 were so low that sidelobes in the FFT process might be affecting the results.

To assess the seasonal variability, the frequency spectra of the modal arrival times was computed. Figure 32 plots the modal arrival time frequency spectra for selected modes. The dominant frequency of variability for all modes examined is seasonal (1 cycle/year). Higher harmonics also appear for modes 1, 2, 29, and 30.

The mesoscale bias variability is examined by comparing the full-field peak arrival time for the range-dependent environment to that of the corresponding range-averaged environment at the 400 km and receiver ranges. In determining the range-averaged environment, only sound speeds in the water column were averaged. With bias defined as the difference between the range-dependent and the range-averaged travel times,

$$\tau_{BIAS} = \tau_{RD} - \tau_{RA}, \text{ computations included determining}$$

- 1) the mean bias over 25 samples, and
- 2) the associated standard deviation for the mean bias.

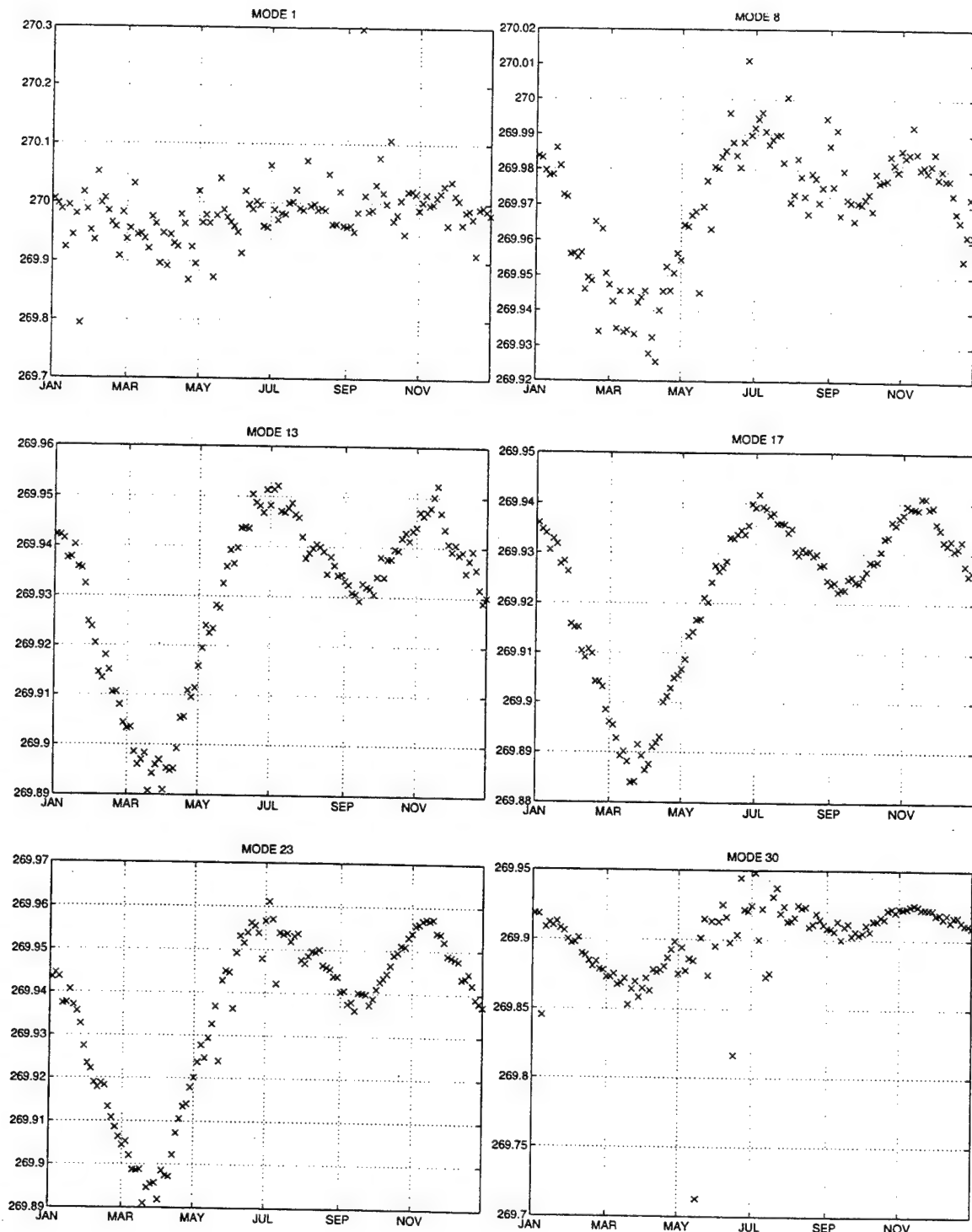


Figure 30. Annual variability in centroid of select modal arrivals at the 400 km range.

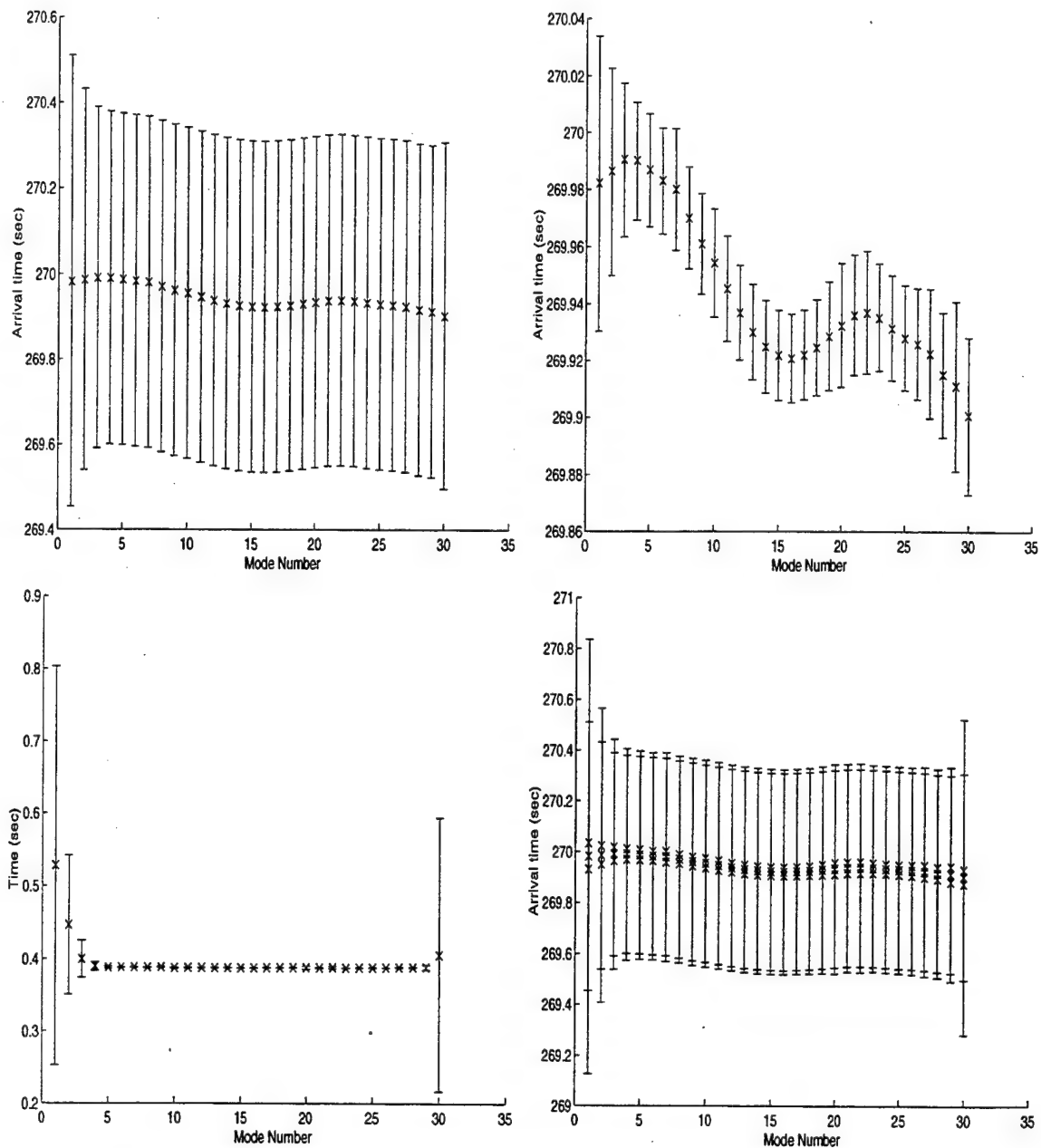


Figure 31. Temporal variability in first 30 modes at the 400 km range. Upper panel left plots the modal ensemble mean centroid arrival time with mean energy distribution. Upper right panel shows variance in the modal ensemble mean arrival time. Lower left panel shows the variance in the modal ensemble mean energy distribution. Lower right panel combines information presented in first three to show the ensemble variance in the modal arrivals and energy distribution.

Mode #	Ensemble mean centroid arrival (secs)	Std deviation of ensemble mean centroid arrival (ms)	Ensemble mean energy distribution (ms)	Std deviation of ensemble mean energy distribution (ms)
1	269.98	51.7	528.2	275.3
2	269.99	36.4	446.4	95.7
3	269.99	27.0	399.6	25.6
4	269.99	20.7	389.6	6.0
5	269.99	19.8	388.1	1.5
6	269.98	18.6	388.2	0.4
7	269.98	21.2	388.2	0.7
8	269.97	17.7	388.2	0.4
9	269.96	17.5	388.4	0.8
10	269.95	18.9	387.5	0.5
11	269.95	18.4	387.7	0.3
12	269.94	16.7	387.7	0.1
13	269.93	16.8	387.5	0.1
14	269.93	16.4	387.5	0.1
15	269.92	16.0	387.2	0.1
16	269.92	15.7	387.2	0.1
17	269.92	15.9	387.6	0.1
18	269.92	17.0	387.6	0.1
19	269.93	19.2	387.8	0.2
20	269.93	21.9	387.7	2.1
21	269.94	21.2	387.4	0.7
22	269.94	21.7	388.0	1.5
23	269.94	18.9	387.5	0.2
24	269.93	18.6	387.9	0.1
25	269.93	18.6	388.0	0.2
26	269.93	19.7	387.8	0.1
27	269.92	23.0	388.3	0.5
28	269.92	22.2	388.2	0.6
29	269.91	30.0	388.5	3.4
30	269.90	27.8	405.3	188.6

Table 8. Ensemble statistics for modal arrivals at the 400 km range.

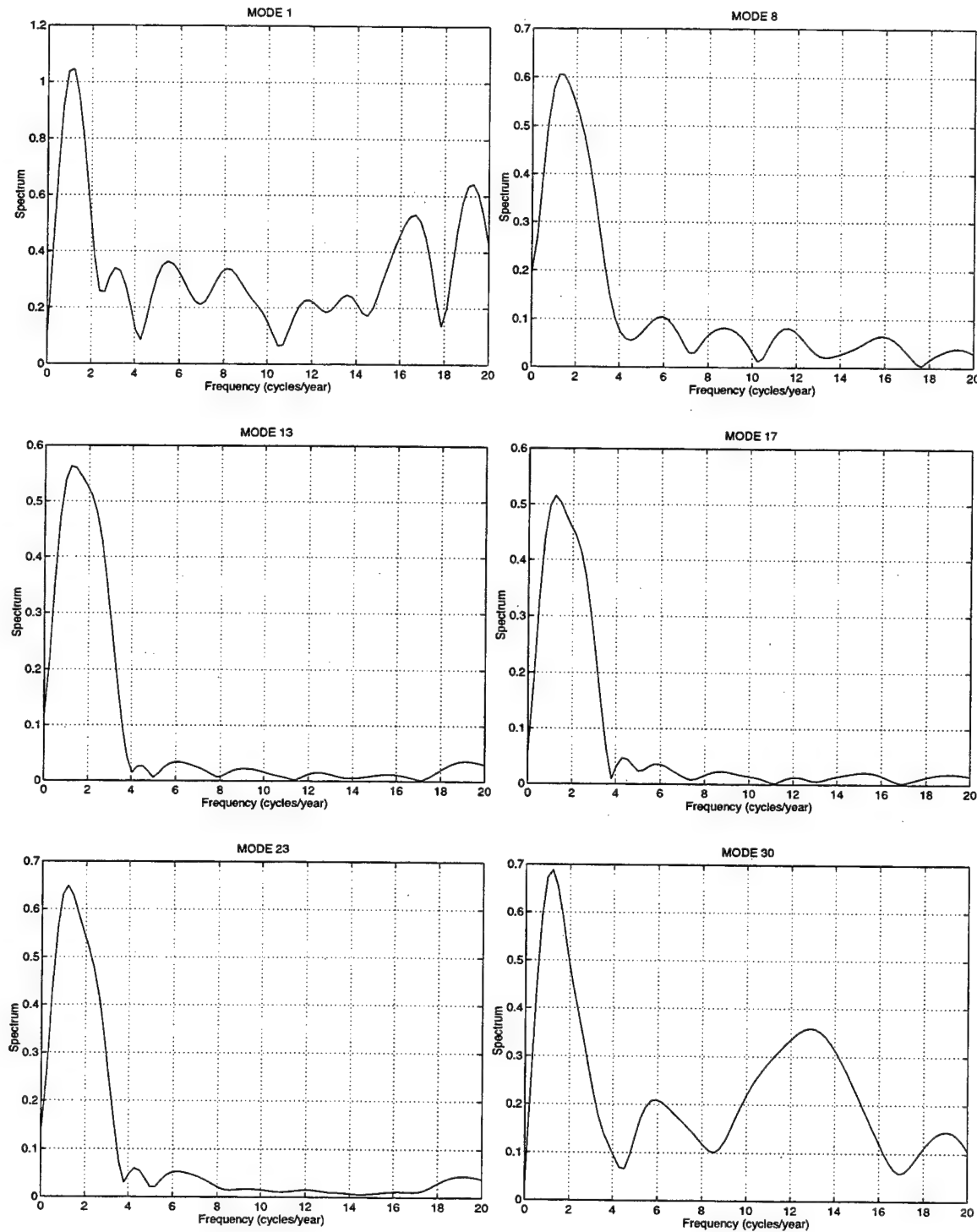


Figure 32. Frequency spectra of modal arrival times at the 400 km range.

For these calculations, the full-field arrival structure is dominated by a single peak arrival, as is evident in Fig. 23. This is partially due to the small bandwidth of the source spectrum. In addition, the source depth was generally several hundred meters above the deep sound channel axis. Thus, it is the higher modes (steeper propagation angles) which are predominantly excited. For the bias analysis, only this single peak was analyzed.

Histograms of the sampled bias at the two ranges are provided by Fig. 33. Bin spacing is 156 ms. In contrast to the generally cold bias results shown for the open ocean environment analyzed in Chapt. IV, the mean bias for the 400 km range appears to have a Gaussian-like distribution about zero bias. As previously mentioned, for this environment and source placement, only higher modes are predominantly excited. As suggested by the open ocean environment analysis, steeper arrivals tend to be more stable in the presence of mesoscale structure. Thus, this bias result does not contradict the general findings of Chapt. IV. At the 474 km range, the distribution indicates a tendency towards a negative (warm) bias. One possible factor contributing to this result for this acoustic path is the effect of bathymetry. With the steep rise in bathymetry near the receiver, energy is stripped out of the highest (and generally faster) modes and subsequently transferred into the ocean bottom or coupled into lower modes. Due to the range-averaging of the sound speed structure, the range-averaged ocean environment near the receiver is warmer than the range-dependent case. Any coupling would then shift energy into faster modes than predicted in the range-dependent ocean, thereby causing a general warm bias trend. Thus, this environment would suggest that mesoscale travel time bias through a region with significant bathymetry influences is not a simple function of range. Finally, the large bias variability, as indicated by a standard deviation in the mean annual bias in excess of 500 ms at each of the two ranges, suggests that the ability to accurately interpret travel time trends by assuming a range-averaged sound speed profile may be limited.

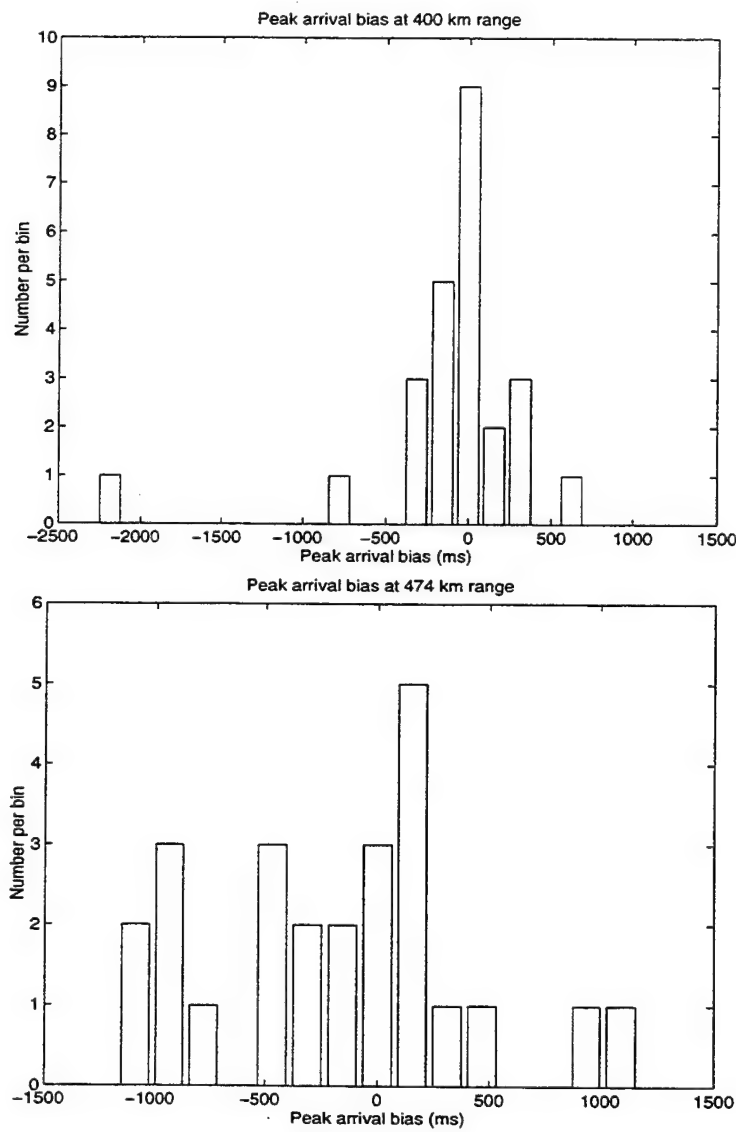


Figure 33. Bias in full-field peak arrival. Upper panel shows bias at the 400 km range, while lower panel shows bias at 474 km receiver range. Statistics based on a sample size of 25 with temporal sampling every 15 days.

E. SUMMARY

In this chapter, acoustic modal travel time variability through a region of the California Current was investigated using a coupled ocean-acoustic model. Basic results from this investigation are interpreted with the caveat that the simulated amplitudes of mesoscale variability in the oceanographic model are known to be low by about a factor of 2 to 4 over a broad spectral range. With that in mind, we have seen that the annual travel time variability along a 400 km path for the lowest 30 modes appears to be less than ± 60 ms. Additionally, for selected modes (12 through 18), the annual travel time variability predicted by this model was less than ± 17 ms along this path. For all modes examined, the arrival time spectra at the 400 km range generally show a dominant frequency of 1 cycle per year. While no attempt has been made in this investigation to separate out the variability due to general ocean circulation from that due to the California Current, these values are on the same order as that suggested by Dushaw for ray travel time variability. This might then suggest that the resolution achievable in this coupled ocean-acoustic model is not yet sufficient to accurately model the coastal region.

The bias analysis for this environment and source placement is in agreement with the findings of the open ocean environment. Specifically, steeper arrivals tend to be more stable in the presence of mesoscale structure, as indicated by the bias results at the 400 km range. From bias results at the 474 km range, this environment also suggests that bathymetry effects may have an impact on the relative sign of the bias. Here, a relatively steep rise in bathymetry appeared to produce a warm shift in the bias.

VI. CONCLUSIONS

The focus of this research was the bias and travel time variability of acoustic propagation in the presence of ocean mesoscale structure. Because such analysis is routinely addressed in the context of normal modes, a modal decomposition of the predicted acoustic fields was required. One of the major contributions of this work was the quantitative assessment of the errors associated with the modal decomposition of an approximate solution by using an improper normal mode basis set. Specifically, it was shown that the wide-angle PE solutions do not, in general, decompose into the standard normal modes of the true acoustic wave equation. Because the wide-angle PE is a common approximation employed in various current research efforts, and forms the basis of the Navy standard PE model, the development and characterization of the proper mode basis set is an important result for the underwater acoustics community. Although a completely general numerical algorithm to compute this basis set was not obtained, significant progress was made toward this goal.

The main results presented in the body of this dissertation examined the bias due to oceanic mesoscale phenomena, and investigated its variability in terms of parameters such as range, local mode number, and mesoscale perturbation strength. Although previous investigators have attempted to address the issue of mesoscale bias using approximate theoretical models, those results have sometimes been ambiguous and contradictory. Furthermore, no model has previously been developed which provides the critical information on the associated variability of the bias. The deep ocean environment research presented here is the first to employ advanced, full-wave modelling techniques to explicitly compute the travel time bias introduced by mesoscale structures and its variability. The results suggest that nonlinear bias effects due to mesoscale ocean structure have a complex relationship with the sound speed perturbation field and bathymetry. In concluding this dissertation, a comparison of general findings from this work to that of earlier investigators (as discussed in Chapt. I) is provided.

- Previous investigations have suggested that the non-linear bias contribution is approximately proportional to range. Results from the open ocean environment with Rossby waves support this finding with the axial delay being on order of 50-200 ms/1000 km.
- Flat, axial rays were found by previous investigators to be less linear than steep rays. In the open ocean environment analyzed here, perturbations were shown to produce a variable overall spreading in the arrival structure, primarily producing a delay in the later, axial arrivals. Earlier arrivals were shown to be relatively stable in the presence of mesoscale structure.
- Earlier investigators suggested that the non-linear bias is small compared to seasonal fluctuations. In contrast, the analysis of a region of the California current system suggests that while the mean bias may be small, the bias variability for some environments may exceed seasonal fluctuations in travel time perturbations. Additionally, the degree of bias variability was found to have no clearly discernible relationship to range or mesoscale strength parameter.
- Earlier investigations reached divergent conclusions with regard to the general sign of the bias. This dissertation work suggested a predominantly cold bias for the open ocean environment field composed of Rossby waves. The acoustic path through the California Current suggested that bathymetry effects may have an impact on the relative sign of the bias. This then suggests a complex relationship between mesoscale bias and its dependence on bathymetry and the sound speed perturbation field.

For the California Current model study, the primary quantities of interest were the modal travel times and their seasonal variability. The annual travel time variability along a 400 km path for the lowest 30 modes appeared to be less than ± 60 ms, with some modes showing a variability of less than ± 17 ms. For all modes examined, the arrival time spectra at the 400 km range generally displayed a dominant frequency of 1 cycle per year.

These values are on the same order as that suggested by a previous investigation using limited CalCOFI data for ray travel time variability. This might then suggest that the resolution achievable in this coupled ocean-acoustic model is not yet sufficient to accurately model the coastal region.

There are several areas for potential research which logically follow this investigation. The first area deals with further development of the wide angle PE mode functions. Additional numerical work is required to develop proper numerical treatment of interfaces, bottom boundaries, and density gradients. Assessments of the mode functions for more complicated environments or other WAPE implementations (other than split-step Fourier) might also be performed.

Finally, with respect to analysis of the region of the California Current system, the statistics of predicted travel time variability as determined from the coupled ocean-acoustic model output might be checked against measured travel time variability for consistency. In addition, insights from this variability study might be potentially applied in array configuration design for NPAL, refining tomographic techniques for this region, or for assessing travel time variability of ATOC transmissions through this region.

REFERENCES

Athanassoulis, G. A., and Skarsoulis, E. K., (1995). "Arrival-time perturbations of broadband tomographic signals due to sound-speed disturbances. A wave-theoretic approach," *J. Acoust. Soc. Am.* **97** (6), pp. 3575-3588.

Chelton, D. B., and Schlax, M. G., (1996). "Global Observations of Oceanic Rossby Waves," *Science* **272**, pp. 234-238.

Chin-Bing, S. A., King, D. B., Davis, J. A., and Evans, R. B., eds., (1993). "Lloyd's Mirror - Wide Angle Propagation," in *PE Workshop II: Proceedings of the Second Parabolic Equation Workshop*, Naval Research Laboratory NRL/BE/7181-93-0001 (US Government Printing Office), pp. 62-67.

Chiu, C.-S., and Desaubies, Y., (1987). "A Planetary Wave Analysis Using the Acoustic and Conventional Arrays in the 1981 Ocean Tomography Experiment," *J. Phys. Oceanogr.* **17**, pp. 1270-1287.

Chiu, C.-S., Semtner, A. J., Ort, C. M., Miller, J. H., and Ehret, L. L., (1994). "A ray variability analysis of sound transmission from Heard Island to California," *J. Acoust. Soc. Am.* **96** (4), pp. 2380-2388.

Collins, M. D., (1988). "FEPE User's Guide," NORDA TN-365, Naval Ocean Research and Development Activity, Stennis Space Center, MS.

Colosi, J. A., Flatte', S. M., and Bracher, C., (1994). "Internal-wave effects on 1000-km oceanic acoustic pulse propagation: Simulation and comparison with experiment," *J. Acoust. Soc. Am.* **96**, pp. 452-468.

DeSanto, J. A., (1977). "Relation between the solutions of the Helmholtz and parabolic equations for sound propagation," *J. Acoust. Soc. Am.* **62** (2), pp. 295-297.

Desaubies, Y., Chiu, C.-S., and Miller, J. H., (1986). "Acoustic mode propagation in a range-dependent ocean," *J. Acoust. Soc. Am.* **80** (4), pp. 1148-1160.

Dushaw, B., (1997). "The Effect of the California Current on Acoustic Transmissions from Pioneer Seamount," *ATOC Occasional Notes*, **36**, 7 January 1997.

Feit, M. D., and Fleck, J. A., (1978). "Light propagation in graded-index fibers," *Appl. Opt.* **17**, 3990-3998.

Garfield, N., Collins, C., Paquette, R., Rago, T., Carter, S., (1997). "Lagrangian Experiment of the California Undercurrent 1993-1995," *J. Phys. Oceanogr.*, submitted.

Godunov, S. K., and Ryabenkii, V. S., (1987). *Difference Schemes*, (Elsevier Science Publishers B. V., Amsterdam), pp. 94-109.

Gradshteyn, I. S., and Ryzhik, I. M., (1994). *Table of Integrals, Series, and Products* (Academic Press, Inc.), pp. 966, 972.

Hardin, R. H. and Tappert, F. D., (1973). "Applications of the split-step Fourier method to the numerical solution of nonlinear and variable coefficient wave equations," *SIAM Rev.* **15**, p. 423.

Heathershaw, A. D., Stretch, C. E., and Maskel, S. J., (1991). "Coupled ocean-acoustic model studies of sound propagation through a front," *J. Acoust. Soc. Am.* **89** (1), pp. 145-155.

Holmes, E. S., and Gainey, L. A., (1991). "Software product specification for the PE model v.3.2," OAML-SPS-22 (Naval Oceanography Office, Bay St. Louis, MS).

Howe, B. M., Mercer, J. M., Spindel, R. C., Worcester, P. F., Hildebrand, J. A., Hodgkiss, W. S., Duda, T. F., and Flatte', S. M., (1991). "SLICE89: A single tomography experiment," in *Ocean Variability and Acoustic Propagation*, edited by J. Potter and A. Warn-Varnas (Kluwer Academic, Dordrecht), pp. 81-86.

Jensen, F. B., Kuperman, W. A., Porter, M. B., and Schmidt, H., (1994). *Computational Ocean Acoustics* (AIP Press, New York), Chap. 5, pp. 271-341.

Lee, D. and Botseas, G., (1982). "An implicit finite-difference (IFD) computer model for solving the parabolic equation," *NUSC Tech. Rep.* 6659.

Mackenzie, K. V., (1981). "Nine-term Equation for Sound Speed in the Ocean," *J. Acoust. Soc. Am.* **70** (4), pp. 807-812.

Mercer, J. A., and Booker, J. R., (1983). "Long-Range Propagation of Sound Through Oceanic Mesoscale Structures," *J. Geophys. Research*, **88**, C1, pp. 689-699.

Milder, D. M., (1969). "Ray and wave invariants for SOFAR channel propagation," *J. Acoust. Soc. Am.* **46**, pp. 1259-1263.

Mooers, C. N. K., and Robinson, A. R., (1984). "Turbulent Jets and Eddies in the California Current and Inferred Cross-Shore Transports," *Science*, **223**, pp. 51-53.

MODE Group, (1978). "The Mid-Ocean Dynamics Experiment," *Deep-Sea Research* **25**, pp. 859-910.

Munk, W. H., (1974). "Sound channel in an exponentially stratified ocean, with application to SOFAR," *J. Acoust. Soc. Am.* **55**, pp. 220-226.

Munk, W. H., and Forbes, A. M. G., (1989). "Global Ocean Warming: An Acoustic Measure?" *Am. Meteorological Soc.* **19**, pp. 1765-1778.

Munk, W. H., Worcester, P., and Wunsch, C., (1995). *Ocean Acoustic Tomography* (Cambridge University Press, Cambridge), p. 88.

Munk, W. H., and Wunsch, C., (1979). "Ocean acoustic tomography: a scheme for large scale monitoring," *Deep-Sea Research* **26A**, pp. 123-161.

Munk, W. H., and Wunsch, C., (1983). "Ocean Acoustic Tomography: Rays and Modes," *Rev. of Geophys. and Space Physics*, **21** (4), pp. 777-793.

Munk, W. H., and Wunsch, C., (1985). "Biases and caustics in long-range acoustic tomography," *Deep-Sea Research* **32** (11), pp. 1317-1346.

Munk, W. H., and Wunsch, C., (1987). "Bias in Acoustic Travel Time Through an Ocean With Adiabatic Range-Dependence," *Geophys. Astrophys. Fluid Dynamics* **39**, pp. 1-24.

Munk, W. H., and Zachariasen, F., (1976). "Sound propagation through a fluctuating stratified ocean: Theory and observation," *J. Acoust. Soc. Am.* **59**, pp. 818-838.

Newhall, A. E., Lynch, J. F., Chiu, C.-S., and Daugherty, J. R., (1990). "Improvements in three dimensional ray tracing codes for underwater acoustics," in *Computational Acoustics: Ocean Acoustic Models and Supercomputing*, edited by D. Lee, A. Cakmak, and R. Vichnevetsky (North-Holland, Amsterdam).

Ocean Tomography Group, (1982). "A demonstration of ocean acoustic tomography," *Nature* **299**, pp. 121-125.

Pierce, A. D., (1965). "Extension of the method of normal modes to sound propagation in an almost stratified medium," *J. Acoust. Soc. Am.* **37**, pp. 19-27.

Porter, M. B., (1991). "The KRAKEN normal mode program," Rep. SM-245 (SACLANT Undersea Research Centre, La Spezia, Italy).

Robinson, A. R., Carman, J. C., and Glenn, S. M., (1994). "A Dynamical System for Acoustic Applications," in *Oceanography and Acoustics*, edited by A. R. Robinson and D. Lee (AIP Press, NY), pp. 80-117.

Semtner, A. J., (1995). "Modeling Ocean Circulation," *Science*, **269**, pp. 1379-1385.

Semtner, A.J., and Chervin, R.M. (1992). "Ocean General Circulation From A Global Eddy-Resolving Model," *J. Geophys. Res.* **97** (C4), pp. 5493-5550.

Shang, E. C., (1989). "Ocean acoustic tomography based on adiabatic mode theory," *J. Acoust. Soc. Am.* **85** (4), pp. 1531-1537.

Shang, E. C., (1997). "Ocean Acoustic Thermometry and Tomography," submitted for publication (University of Colorado, Boulder, CO).

Shang, E. C., and Wang, Y. Y. (1993). "The Nonlinearity of Modal Travel Time Perturbation," in *Computational Acoustics - Vol. 1*, edited by R. L. Lau, D. Lee and A. R. Robinson (Elsevier, North-Holland), pp. 385-397.

Shang, E. C., and Wang, Y. Y., (1993). "Acoustic Travel Time Computation Based on PE Solution," *J. Comp. Acoust.* **1** (1), pp. 91-100.

Shang, E. C., and Wang, Y. Y., (1996). "The Impact of Mesoscale Oceanic Structure on Global-Scale Acoustic Propagation," in *Theoretical and Computational Acoustics* edited by D. Lee, Y-H Pao, M.H. Schultz, and Y-C Teng, (World Scientific Publishing), pp. 409-432.

Smith, A. R., Smith, K. B., and Chiu, C.-S., (1996). "Effects of Ocean Mesoscale Features on Adiabatic Mode Travel Times," in *Proceedings of the Third European Conference on Underwater Acoustics*, edited by J. S. Papadakis, (Crete University Press, Heraklion), pp. 297-302.

Smith, K. B., (1992). "Broadband PE propagation through mesoscale perturbations," *J. Acoust. Soc. Am. Suppl.* **91**, p. 2327.

Smith, K. B., Brown, M. G., and Tappert, F. D., (1992a). "Ray chaos in underwater acoustics," *J. Acoust. Soc. Am.* **91**, pp. 1939-1949.

Smith, K. B., Brown, M. G., and Tappert, F. D., (1992b). "Acoustic ray chaos induced by mesoscale ocean structure," *J. Acoust. Soc. Am.* **91**, pp. 1950-1959.

Smith, K. B., and Tappert, F. D., (1993). "UMPE: The University of Miami Parabolic Equation Model, Version 1.0," Marine Physical Laboratory Technical Memo 432.

Spiesberger, J. L., (1985a). "Ocean acoustic tomography: Travel time biases," *J. Acoust. Soc. Am.* **77** (1), pp. 83-100.

Spiesberger, J. L., (1985b). "Gyre-Scale Acoustic Tomography: Biases, Iterated Inversions, and Numerical Methods," *J. Geophys. Research*, **90** (C6), pp. 11869-11876.

Spiesberger, J. L., and Worcester, P. F., (1983). "Perturbations in travel time and ray geometry due to mesoscale disturbances: A comparison of exact and approximate calculations," *J. Acoust. Soc. Am.* **74** (1), pp. 219-225.

Spindel, R. C. and Worcester, P. F., (1990). "Ocean Acoustic Tomography," *Scientific American*, **263** (4), pp. 94-99.

Spindel, R. C. and Worcester, P. F., (1991). "Ocean Acoustic Tomography: A Decade of Development," *Sea Technology*, July 1991, pp. 47-52.

Stammer, D., Tokmakian, R., Semtner, A., and Wunsch, C., (1996). "How well does a $1/4^\circ$ global circulation model simulate large-scale oceanic observations?" *J. Geophys. Research*, **101** (C10), pp. 25779-25811.

Staten, R. A., Chiu, C.-S., and Semtner, A., (1996). "A Simulation Study of the Variability of Acoustic Transmissions from Hawaii to Monterey," in *Theoretical and Computational Acoustics*, edited by D. Lee, Y.-H. Pao, M.H. Schultz (World Scientific Publishing), pp. 505-525.

Tappert, F. D., (1977). "The parabolic approximation method," in *Wave Propagation and Underwater Acoustics, Lecture Notes in Physics*, edited by J. B. Keller and J. S. Papadakis (Springer-Verlag, Berlin), Vol. **70**, pp. 224-287.

Tappert, F. D., and Tang, X., (1995). "Acoustic travel time effects of oceanic mesoscale structure at global ranges," unpublished paper, (U. of Miami, Miami, FL) dated 27 Oct 1995.

Thomson, D. J., (1993). "PE-Based Spectral Decomposition," in *PE Workshop II: Proceedings of the Second Parabolic Equation Workshop*, edited by S.A. Chin-Bing, D.B. King, J. A. Davis, and R.B. Evans, Naval Research Laboratory NRL/BE/7181-93-0001 (US Government Printing Office), pp. 296-320.

Thomson, D. J., and Chapman, N. R., (1983). "A wide-angle split-step algorithm for the parabolic equation," *J. Acoust. Soc. Am.* **74**, pp. 1848-1854.

Worcester, P. and Spindel, R., (1997). "North Pacific Acoustic Laboratory," presented at Office of Naval Research Long Range Acoustic Propagation Workshop, (Lake Arrowhead, CA), 3-4 March 1997.

INITIAL DISTRIBUTION LIST

1. Defense Technical Information Center 2
8725 John J. Kingman Rd., STE 0944
Ft. Belvoir, VA 22060-6218
2. Dudley Knox Library 2
Naval Postgraduate School
411 Dyer Rd.
Monterey, CA 93943-5101
3. Dr. Kevin Smith, Code PH/Sk 5
Physics Department
833 Dyer Rd., RM 142A
Naval Postgraduate School
Monterey, CA 93943-5117
4. Dr. Ching-Sang Chiu, Code OC/Ci 2
Oceanography Department
833 Dyer Rd., RM 318
Naval Postgraduate School
Monterey, CA 93943-5122
5. Chairman, Code PH 1
Physics Department
833 Dyer Rd., RM 201
Naval Postgraduate School
Monterey, CA 93943-5117
6. Chairman, Code EC 1
Electrical and Computer Engineering Department
833 Dyer Rd., RM 437
Naval Postgraduate School
Monterey, CA 93943-5121
7. Dr. Ellen Livingston, Code 3210A 1
Office of Naval Research
800 North Quincy Street
Arlington, VA 22117

8. Dr. John Roesel 1
NCCOSC RDTE D-103
53570 Silvergate Ave
San Diego, CA 92152-5031